



THE HONG KONG  
POLYTECHNIC UNIVERSITY

香港理工大學

Pao Yue-kong Library

包玉剛圖書館

---

## Copyright Undertaking

This thesis is protected by copyright, with all rights reserved.

**By reading and using the thesis, the reader understands and agrees to the following terms:**

1. The reader will abide by the rules and legal ordinances governing copyright regarding the use of the thesis.
2. The reader will use the thesis for the purpose of research or private study only and not for distribution or further reproduction or any other purpose.
3. The reader agrees to indemnify and hold the University harmless from and against any loss, damage, cost, liability or expenses arising from copyright infringement or unauthorized usage.

If you have reasons to believe that any materials in this thesis are deemed not suitable to be distributed in this form, or a copyright owner having difficulty with the material being included in our database, please contact [lbsys@polyu.edu.hk](mailto:lbsys@polyu.edu.hk) providing details. The Library will look into your claim and consider taking remedial action upon receipt of the written requests.

The Hong Kong Polytechnic University

Department of Electrical Engineering

**Novel Splice Techniques and Micro-hole Collapse  
Effect in Photonic Crystal Fibers**

Limin XIAO

A thesis submitted in partial fulfilment of the requirements for  
the Degree of Doctor of Philosophy

Nov 2007

## **CERTIFICATE OF ORIGINALITY**

I hereby declare that this thesis is my own work and that, to the best of my knowledge and belief, it reproduces no material previously published or written, nor material that has been accepted for the award of any other degree or diploma, except where due acknowledgement has been made in the text.

---

Limin XIAO

## ABSTRACT

Photonic crystal fibers (PCFs), which are also named microstructured optical fibers or holey fibers, represent one of the most active research areas today in the field of fiber optics.

Because of the freedom they offer in their design and novel wave-guiding properties, PCFs have resulted in a number of novel devices, communication and sensing applications that are difficult to achieve with conventional fibers. The micro-holes of PCFs can allow for the infusion of materials, thus the combination of PCFs with new materials provides a new platform for ultra-compact photonic devices. In practical applications, low-loss connection PCFs with conventional fibers is a key issue for integrating PCF devices into existing fiber optic systems. However, connecting PCFs to conventional fibers without incurring too much loss is a very challenging problem. The previous methods to solve this problem are time-consuming and expensive. So it is very important to find a simple and low-cost way to splice different PCFs with conventional single mode fibers (SMFs).

Two novel techniques were proposed to solve this problem in the thesis. One is fusion splicing technique; the other is micro-tip technique.

First, fusion splicing technique for PCFs is investigated in detail. The splice loss is generally due to two reasons: one is the mode field mismatch between PCFs and SMFs; the other is that the air holes in PCFs may completely collapse in the vicinity of the splice joint during the splicing process, which significantly increases the coupling loss by destroying the light guiding structure of PCF near the joint interface. Different kinds of PCFs have different micro-hole structures, and the properties of heat-induced collapse when splicing are quite different. One solution

which is suitable for one kind of PCF will fail when applying to other kinds of PCF. So a detailed study about the effect of micro-hole collapse on the splice loss for different kinds of PCFs is very important. For fusion splicing SMFs and PCFs having similar mode field diameters, a low-loss joint with good mechanical strength can be formed by choosing a suitably weak fusion current, short fusion time, offset and overlap to minimize the collapse of air holes and well melt two fibers together. For small-core PCFs, an optimum mode field match at the interface of PCF/SMF and an adiabatic mode field variation in the longitudinal direction of the small-core PCF can be achieved by repeated arc discharges applied over the splicing joint to gradually collapse the air holes of the small-core PCF. Low-loss fusion splicing of five different PCFs with SMFs are achieved, including large mode PCF, hollow-core PCF, nonlinear PCFs with low and high air-filling fraction and polarization maintaining PCF.

The other novel technique is using micro-tips. The method is based on growing photopolymer micro-tips directly on the end face of SMFs. The advantages of this micro-tip fabrication method are its simplicity, controllability, reproducibility and being inexpensive. The shape and the size of the tips can be controlled, by adjusting the laser power, the exposure time and the oxygen diffusion concentration for polymerization, to match its mode field to the small-core PCFs. A photopolymer micro-tip integrated on the end face of a SMF is used to reduce the mode field diameter and increase the numerical aperture of the light beam coming out from the SMF, so that there is a better match to the small mode field diameter and the large numerical aperture of small-core PCFs. A 5 dB improvement in coupling efficiency between a SMF and a commercial small-core, highly nonlinear PCF is demonstrated. This compact and efficient butt-coupling method is particularly suitable for PCF gas

sensor applications where holes in the PCF need to be kept open at the joint for easier access to the evanescent field.

Micro-hole collapse effect can be used to fabricate selective injection PCFs. The suitable arc discharge energy can cause the cladding holes to collapse while leaving the central hollow core to remain open. Thus a simple method for selective filling the central hole of PCFs based on a conventional fusion splicer is developed. The opening and closing of the central hole and the holes in the cladding can be controlled to a certain degree by controlling the fusion current, the fusion duration and the fusion offset position. Experiments show that this method can be used to make hybrid polymer/silica PCFs with the central hole filled by a polymer. The quality of the hybrid fiber is good and the fabrication process is highly reproducible. This novel structure not only introduces an effective way for micro-fluidics sensing applications, but also opens new perspectives for nonlinear applications by filling various functional materials into the central hole of a hollow-core PCF.

Hybrid PCF guides light by a novel guiding mechanism, which is a combination of index-guiding and bandgap-guiding. The properties of the hybrid PCF are systematically investigated, including modal effective index, mode field area, confinement loss, group velocity dispersion and birefringence. The hybrid PCF can be fabricated by selectively collapsing micro-holes and filling a row of air holes with high-index liquid. The potential applications are discussed.

## **ACKNOWLEDGEMENTS**

I would like to express my deepest gratitude to my chief supervisor, Chair Professor M. Suleyman Demokan, for careful guidance along the way. His wisdom and encouragement enlightened me to finish my research work. I am also very grateful to my co-supervisor, Professor Wei Jin, for his valuable suggestion and careful guidance. I have been truly lucky to be supervised by two friendly people with great insight.

I would also like to acknowledge Chair Professor H. Y. Tam for very useful discussions and his kind support. I am very grateful for the support and technical help of Dr. H. L. Ho. I also thank other colleagues for useful discussions: Professor C. L. Zhao, Professor Z. Wang, Dr. J. Ju, Dr. Y. L. Hoo, Dr. Y. P. Wang, Dr. W. S. Man, and Mr. M.N. Yeung.

Finally, I want to express my deepest gratitude to my grandparents, parents, my two sisters Yanhong and Yanxia, and my girl friend Ami S. Y. Wong for their endless love and support.

## Contents

Abstract	i
Acknowledgements	iv
Contents	v
Chapter 1 Introduction	1
1.1 History of photonic crystal fibers	1
1.2 Motivation for this work	4
1.3 Thesis outline	6
References	8
Chapter 2 Background	12
2.1 Guiding mechanisms of PCFs	12
2.1.1 Index-guiding PCFs	12
2.1.2 Bandgap PCFs	16
2.1.3 Hybrid PCFs	24
2.2 Properties and applications of index-guiding PCFs	25
2.2.1 Small index step	25
2.2.2 Large index step	28
2.2.3 Asymmetric index distribution	31
2.3 Properties and applications of bandgap PCFs	32
2.3.1 1D bandgap PCF	32
2.3.2 2D bandgap PCF	34
2.4 Modified and combined structure PCFs	36
2.4.1 Modified-structure PCFs	36

---

2.4.2 Combined-structure PCFs	38
2.5 Combination PCFs with new materials: fruitful applications	40
2.5.1 PCF with gases	41
2.5.2 PCF with fluids	42
2.6 Overview of PCF splice techniques	44
2.6.1 Splicing PCFs with doped core	45
2.6.2 Splicing PCFs using CO <sub>2</sub> laser	46
2.6.3 Splicing PCFs using GRIN fiber lens	46
2.6.4 Tapered PCFs	47
2.6.5 Splice-free PCFs	49
2.6.6 Splicing PCFs using fusion splicers	50
2.7 Summary	50
Reference	51
Chapter 3 Fusion splice PCFs	65
3.1 Introduction	65
3.2 Challenges in splicing PCFs	67
3.2.1 Collapse of air holes	69
3.2.2 Mode field mismatch	70
3.3 The principle of low-loss splicing	71
3.4 Fusion splicing PCF/PCF experiment	74
3.5 Low-loss fusion splicing SMF/PCF experiments	76
3.5.1 Splicing SMF to solid-core PCF with similar MFDs	77
3.5.2 Splicing SMF to hollow-core PCF with similar MFDs	78
3.5.3 Splicing SMF to small-core PCF with low air-filling fraction	81
3.5.4 Splicing SMF to small-core PCF with high air-filling fraction	92

---

3.5.5 Splicing SMF to polarization maintaining PCF	96
3.6 Summary	98
Reference	100
<b>Chapter 4 Microtips for optical coupling to PCFs</b>	<b>103</b>
4.1 Introduction	103
4.2 Method of fabricating photopolymer microtips	104
4.3 Controllable shape of microtips	108
4.4 Low-loss coupling between PCFs and SMFs using microtips	111
4.5 Summary	115
Reference	116
<b>Chapter 5 Fabrication of selective injection PCFs</b>	<b>118</b>
5.1 Introduction	118
5.2 Method of fabrication: micro-hole collapse effect	120
5.3 Experimental studies of fabrication	125
5.3.1 The effect of fusion current	125
5.3.2 The effect of fusion duration	127
5.3.3 The effect of fusion offset	128
5.4 Filling the central hole of PCF	129
5.5 Summary	130
Reference	131
<b>Chapter 6 Hybrid PCF</b>	<b>134</b>
6.1 Introduction	134
6.2 Theory of hybrid PCFs	135
6.2.1 Description of the approach	135
6.2.2 Analysis and Discussion	137

6.3 Method of fabrication: micro-hole collapse effect	147
6.4 Potential Applications	149
6.5 Summary	150
Reference	151
<b>Chapter 7 Conclusion and future work</b>	<b>153</b>
7.1 Conclusion	153
7.2 Future work	155
<b>Appendix: Publication</b>	<b>157</b>

# Chapter 1

## Introduction

### 1.1 History of Photonic Crystal Fibers

Photonic crystal fibers (PCFs), which are also named microstructured optical fibers (MOFs) or holey fibers (HFs), represent one of the most active research areas today in the field of fiber optics. PCFs have wavelength-scale microscopic structure that runs along the entire fiber length. This structure enables light to be confined to the fiber by novel mechanisms. PCFs generally guide light by two mechanisms: one is modified total internal reflection (index-guiding) and the other is photonic band gap effect (bandgap-guiding). In index-guiding PCFs, similar to conventional fibers, light is guided in a higher index core by modified total internal reflection from a low effective index cladding; in bandgap PCFs, light is confined in a low-index core or even hollow air core by reflection from a photonic crystal cladding, the cladding can be a one-dimensional (1-D) or two-dimensional (2-D) photonic crystal structure. Because of the freedom they offer in their design and novel wave-guiding properties, PCFs have resulted in a number of fiber optic devices, communication and sensing applications that are difficult to achieve with conventional fibers. The development of PCF technology has revolutionized traditional fiber optics and a broad range of

innovations based on PCFs is being explored.

Although PCFs attracted much attention after the mid-1990s, the history of PCFs can be comparable to conventional fibers. In 1970, following an earlier suggestion by Kao, Hockman [1], and Werts [2], the loss of conventional fibers was reduced drastically to about 20 dB/km [3]. Further progress resulted in bringing down the loss to about 0.2 dB/km near the 1.55  $\mu\text{m}$  wavelength region in 1979 [4]. The availability of low-loss conventional fibers led to a revolution in the field of lightwave technology and started the era of optical fiber communications [5]. Also in mid 1970s, the rudiment of PCFs appeared. Kaiser et al [6] demonstrated low loss, single mode or multimode holey fibers fabricated by pure fused silica in 1974, as shown in Fig. 1(a). This is the earliest report about PCFs. In 1978, Yeh et al. [7] first proposed the theory of Bragg fiber. The Bragg fiber can confine light in the low-index core, even hollow-core, provided that the core is surrounded by a suitably designed alternating ring cladding of high and low refractive indices. It is the first theoretical report of the bandgap PCF; this bandgap is formed by 1D photonic crystal structure in the fiber cladding. However, the microscopic high index contrast multilayers of the cladding usually have very different thermo-mechanical property, which makes 1-D bandgap PCFs difficult to fabricate using traditional thermal drawing method and limits its development.

A number of years later, a PCF with 2-D photonic crystal structure was proposed in 1995 [8]. Full 2-D photonic bandgaps can be formed by a periodic structure comprising just air and fused silica [8]. Air is mechanically and thermally compatible with most materials [9], it is transparent over a broad spectral range and it has a very low refractive index; fused silica is an excellent material for drawing and fabrication, so PCFs made of air-silica have been widely studied and developed

[9, 10]. In 1996, a solid-core PCF with hexagonal air-silica cladding was fabricated [11] by a stack-draw technique, as shown in Fig. 1(b). This index-guiding PCF supported a single-mode over a very broad spectral range. In 1998, the first 2-D bandgap PCF was demonstrated [12], as shown in Fig. 1(c), where light can be guided in the low-index core by “reflection” from a 2D honeycomb pattern photonic crystal cladding.

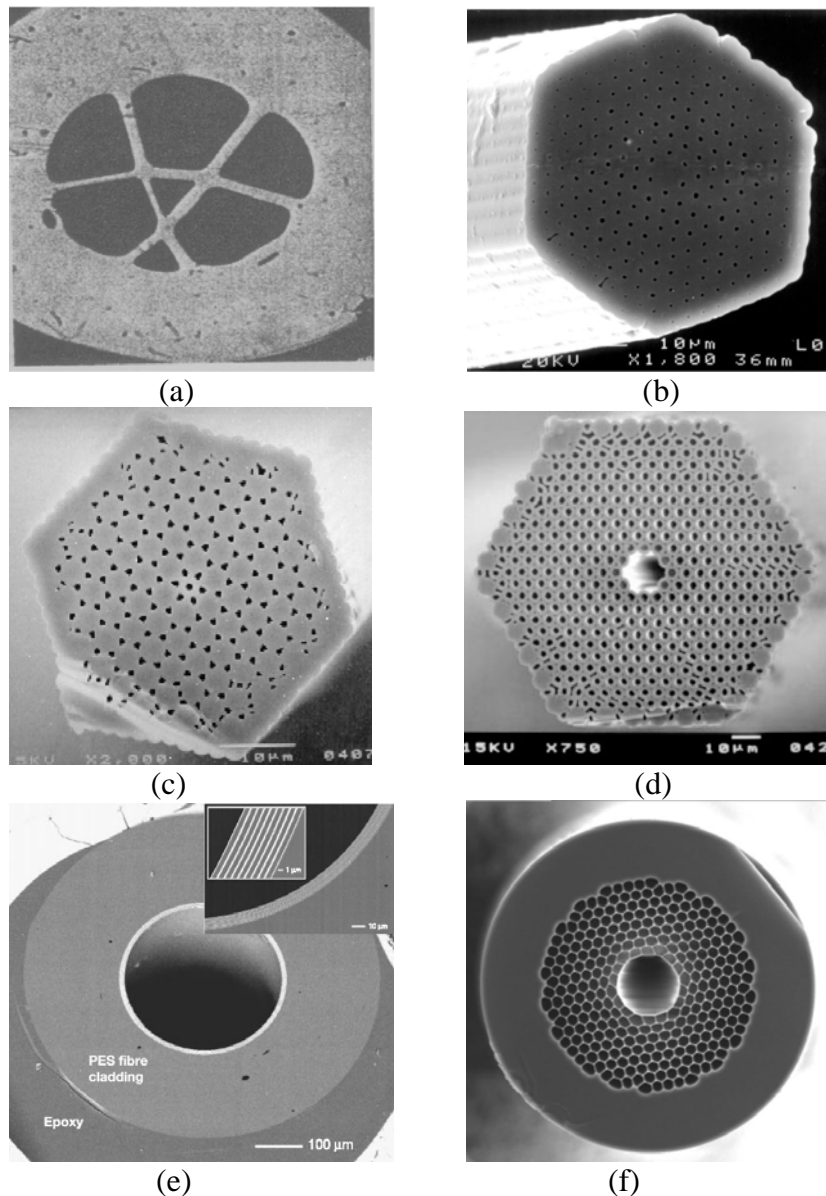


Figure 1.1 The cross-sections of different PCFs: (a) the first air-silica PCF (1974) [6]; (b) the first index-guiding PCF with 2-D photonic crystal cladding (1996) [11]; (c) the first bandgap PCF with 2-D photonic crystal cladding (1998) [12]; (d) the first hollow-core PCF with 2-D photonic crystal cladding (1999) [13]; (e) the hollow-core PCF with 1-D photonic crystal cladding for transmission of CO<sub>2</sub> laser

(2002) [14]; (f) the hollow-core PCF with 2-D photonic crystal cladding with record low loss (2005) [15].

A PCF which confined light in a hollow-core by 2-D bandgap-guiding was first demonstrated in 1999 [13], as shown in Fig. 1(d). In the same year, hollow-core 1-D bandgap PCF was fabricated by Fink et al. [14], and further progress for this structure was made using a roll-draw technique and thus a hollow-core PCF guiding light from a CO<sub>2</sub> laser with low loss was demonstrated in 2002 [15], as shown in Fig. 1(e).

With various types of PCFs invented, the performance of the PCFs was also improved rapidly. One of the most important factors for any optical fiber is loss. Early reported index-guiding PCF had large loss (240 dB/km) and the length was limited to tens of meters [16]. However, the loss was rapidly reduced in the following years and an attenuation of 0.28 dB/km at the wavelength of 1550 nm was achieved in 2003 [17], which approaches the intrinsic loss of conventional silica based fiber (0.14 dB/km). Specially designed index-guiding PCFs have “endless” single-mode property, thus a significant wider wavelength range can be used in transmission than conventional fibers. For hollow-core bandgap PCFs, the early loss was about 1000 dB/km in 2001 [18], however, it reduced dramatically to 1.2 dB/km at the wavelength of 1620 nm in 2005 [19], as shown in Fig. 1(f). This was because light in hollow-core PCFs can propagate in the air and avoid losses of fundamental scattering and absorption of silica in conventional fibers. A loss of 0.1 dB/km in a hollow-core PCF is possible [19], which is less than that of the best conventional fiber. Therefore PCFs may be better candidates for future optical communication transmission.

## **1.2 Motivation for this work**

Besides comparable transmission loss with conventional fibers, PCFs have a number of novel properties and applications that are difficult to achieve with conventional fibers. This results in PCFs having many important advantages over conventional fibers in various areas. For index-guiding PCFs, the properties include endlessly single mode operation [20], large mode area [21], high numerical aperture [22], high birefringence [23], high nonlinear coefficient [24] and dispersion management [25]. They can be widely used in ultrawide-band transmission, high power fiber amplifiers or lasers, high power pumping or beam delivery, as a polarization-maintaining component or a polarizer, supercontinuum spectrum generation or other nonlinear applications, nearly zero ultra-flattened or anomalous dispersion, evanescent field sensing and so on. For bandgap PCFs, the most important property is hollow-core guiding. It can be used in high power laser delivery of special wavelengths such as from CO<sub>2</sub> lasers [15], high power pulse transmission [26], gas-based nonlinear optics [27], atom or particle guidance [28], and gas and liquid sensors [29, 30]. The micro-hole of PCFs can allow the infusion of materials, thus the combination of PCFs with new materials provides a new platform for a number of ultra-compact photonic devices [31-33]. We will describe in detail the properties and applications of PCFs in Chapter 2.

In practical applications, low-loss connection of PCFs with conventional fibers is a key issue for integrating PCF devices into existing fiber optic systems. However, connecting PCFs to conventional fibers without incurring too much loss is a very challenging problem, which limits the wide development of PCF technology. The previous methods to solve this problem are time-consuming, expensive and ultimately unsatisfactory. So it is significant important to find a simple and low-cost way to splice different PCFs with conventional single mode fibers (SMFs). In this

thesis, two novel techniques have been proposed to solve this problem. One is a special fusion splicing technique and the other is micro-tip technique. The former technique uses a conventional fusion splicer to splice different PCFs with conventional fibers. Since fusion splicing is the most mature technology in splicing conventional fibers and that commercial fusion splicers are widely used, it will be a simple and practical solution to splice SMFs and PCFs. However, PCFs have micro-hole structures which are totally different from conventional fibers, and therefore fusion splicing different PCFs to conventional fibers is a significant challenge. The micro-hole collapse phenomenon and its effect on splice loss, and the optimized fusion condition of low-loss splice will be investigated in detail in Chapter 3. The latter technique is based on growing photopolymer micro-tips on the end face of SMFs to match the mode field of PCFs. The advantages of this microtip fabrication method are its simplicity, controllability, reproducibility, and inexpensiveness, which will be described in Chapter 4. Micro-hole collapse effect during fusion splicing can be used to fabricate selective injection PCFs, which not only introduces an effective way for micro-fluidic sensing applications, but also opens new perspectives for nonlinear applications by filling various functional materials into the central hole of a hollow-core PCF (Chapter 5). Micro-hole collapse effect can also be used to fabricate hybrid PCFs. A hybrid PCF guides light by a novel guiding mechanism, which is a combination of index-guiding and bandgap-guiding; its potential applications will be discussed in Chapter 6.

### **1.3 Thesis outline**

The thesis is organized as follows:

**Chapter 2** We review three guiding mechanisms of PCFs: index-guiding, bandgap-guiding and hybrid-guiding PCFs in section 2.1. The properties and

applications of index-guiding PCFs and bandgap PCFs are reviewed in section 2.2 and section 2.3, respectively. In section 2.4, we study modified and combined structure of PCFs. In particular, the applications of combination PCFs with new material are reviewed in section 2.5. Finally, the various PCF splice techniques are exhaustively reviewed in section 2.6.

**Chapter 3** After introducing the challenges in splicing PCFs (section 3.2), we give the principle of low-loss splicing PCFs in section 3.3. The experiments are then demonstrated and explained in the next sections. In section 3.4, we study fusion splicing between PCFs. In section 3.5, we study splicing SMF to solid-core PCF with similar mode field diameters (MFDs), hollow-core PCF with similar MFDs, small-core PCF with low-air filling fraction, small-core PCF with high-air filling fraction and polarization maintaining PCF, respectively.

**Chapter 4** In this chapter, we explore a method of fabricating photopolymer micro-tips in section 4.2, and then we demonstrate that the shape and the size of the micro-tips can be controlled by adjusting the laser power, the exposure time and the oxygen diffusion concentration for polymerization (section 4.3). We also demonstrate the low-loss coupling between PCFs and SMFs using micro-tips in section 4.4.

**Chapter 5** We present a method of fabrication selective injection PCFs by micro-hole collapse effect in section 5.2. In the next section, we demonstrate experimental studies of fabrication by controlling the fusion current, fusion duration and offset position. In section 5.4, the experimental filling of the central hole of PCF is demonstrated and the potential applications are discussed.

**Chapter 6** In this chapter, we present the theory of hybrid PCFs in section 6.2. The modal effective index, mode field area, confinement loss, group velocity

dispersion, and birefringence are numerically simulated and compared with those of the corresponding index-guiding and bandgap PCFs. In the next sections, we discuss the potential applications of the hybrid PCFs by filling selectively holes using micro-hole collapse effect.

**Chapter 7** In the last chapter, we summarize the research work accomplished in the thesis in section 7.1 and list the contributions of our work. Future work, which should be conducted, is recommended in section 7.2.

## References for Chapter 1

1. K. C. Kao and G. A. Hockham, "Dielectric-fiber surface waveguides for optical frequencies," *Proc. IEE*, vol. 113, pp. 1151-1158, (1966).
2. A. Werts, "Propagation de la lumiere coherente dans les fibres optiques," *L'Onde Electrique*, vol. 46, pp. 967-980, (1966).
3. F. P. Kapron, D. B. Keck, and R. D. Maurer, "Radiation losses in glass optical waveguides," *Appl. Phys. Lett.*, vol. 17, pp. 423-425, (1970).
4. T. Miya, Y. Terunuma, H. Hosaka, and T. Miyashita, "Ultimate low-loss single-mode fibre at 1.55  $\mu\text{m}$ ," *Electron. Lett.*, vol. 15, pp. 106-108, (1979).
5. G. P. Agrawal, *Fiber-optic communication systems*, Wiley, New York, 1992.
6. P. V. Kaiser and H. W. Astle, "Low-loss single-material fibers made from pure fused silica," *The Bell System Technical Journal*, vol. 53, pp. 1021-1039, (1974).
7. P. Yeh, A. Yariv, and E. Marom, "Theory of Bragg fiber," *J. Opt. Soc. Am.*, vol. 68, pp. 1196-1201, (1978).
8. T. A. Birks, P. J. Roberts, P. Russell, D. M. Atkin, and T. J. Shepherd, "Full 2-D

- photonic bandgaps in silica/air structures,” *Electron. Lett.*, vol. 31, pp. 1941-1942, (1995).
9. J. C. Knight, “Photonic crystal fibres,” *Nature*, vol. 424, pp. 847-851, (2003).
  10. P. Russell, “Photonic crystal fibers,” *Science*, vol. 299, pp. 358-362, (2003).
  11. J. C. Knight, T. A. Birks, P. Russell, and D. M. Atkin, “All-silica single-mode optical fiber with photonic crystal cladding,” *Opt. Lett.*, vol. 21, pp. 1547-1549, (1996).
  12. J. C. Knight, J. Broeng, T. A. Birks, and P. Russell, “Photonic band gap guidance in optical fibers,” *Science*, vol. 282, pp. 1476-1478, (1998).
  13. R. F. Cregan, B. J. Mangan, J. C. Knight, T. A. Birks, P. Russell, P. J. Roberts, and D. C. Allan, “Single-mode photonic band gap guidance of light in air,” *Science*, vol. 285, pp. 1537-1539, (1999).
  14. Y. Fink, D. J. Ripin, S. Fan, C. Chen, J. D. Joannopoulos, and E. L. Thomas, “Guiding Optical Light in Air Using an All-Dielectric Structure,” *J. Lightwave Technol.*, vol. 17, pp. 2039-2041, (1999).
  15. B. Temelkuran, S. D. Hart, G. Benoit, J. D. Joannopoulos, and Y. Fink, “Wavelength-scalable hollow optical fibres with large photonic bandgaps for CO<sub>2</sub> laser transmission,” *Nature*, vol. 420, pp. 650–653, (2002).
  16. P. J. Bennett, T. M. Monro, and D. J. Richardson, “Toward practical holey fiber technology: fabrication, splicing, modeling, and characterization,” *Opt. Lett.*, vol. 24, pp. 1203-1205, (1999).
  17. K. Tajima, K. Kurokawa, K. Nakajima, and I. Sankawa, “Photonic crystal fiber,” *NTT Technical Review*, vol. 3, pp. 57-61, (2005).
  18. J. A. West, N. Venkataramam, C. M. Smith, and M. T. Gallagher, “Photonic crystal fibers,” *Proc. ECOC*, Th.A.2.2, pp. 582-585, (2001).

19. P. Roberts, F. Couny, H. Sabert, B. Mangan, D. Williams, L. Farr, M. Mason, A. Tomlinson, T. Birks, J. Knight, and P. Russell, "Ultimate low loss of hollow-core photonic crystal fibres," *Opt. Express*, vol. 13, pp. 236-244, (2005).
20. T. A. Birks, J. C. Knight, and P. Russell, "Endlessly single-mode photonic crystal fiber," *Opt. Lett.*, vol. 22, pp. 961-963, (1997).
21. J. C. Knight, T. A. Birks, R. F. Cregan, P. Russell and P. D de Sandro, "Large mode area photonic crystal fibre," *Electron. Lett.*, vol. 34, pp. 1347-1348 (1998).
22. W. Wadsworth, R. Percival, G. Bouwmans, J. C. Knight, and P. Russell, "High power air-clad photonic crystal fibre laser," *Opt. Express*, vol. 11, pp. 48-53, (2003).
23. A. Ortigosa-Blanch, J. C. Knight, W. J. Wadsworth, J. Arriaga, B. J. Mangan, T. A. Birks, and P. Russell, "Highly birefringent photonic crystal fibers," *Opt. Lett.*, vol. 25, pp. 1325-1327, (2000).
24. P. Petropoulos, T. M. Monro, W. Belardi, K. Furusawa, J. H. Lee, and D. J. Richardson, "2R-regenerative all-optical switch based on a highly nonlinear holey fiber," *Opt. Lett.*, vol. 26, pp. 1233-1235, (2001).
25. T. A. Birks, D. Mogilevtsev, J. C. Knight, and P. Russell, "Dispersion compensation using single-material fibers," *Photon. Technol. Lett.*, vol. 11, pp. 674-676, (1999).
26. D. G. Ouzounov, F. R. Ahmad, A. L. Gaeta, D. Muller, N. Venkataraman, M. Gallagher, C. M. Smith, and K. W. Koch, "Generation of megawatt solitons in hollow-core photonic band-gap fibers," *Science*, vol.301, pp. 1702-1704, (2003).
27. F. Benabid, J. C. Knight, G. Antonopoulos, and P. Russell, "Stimulated Raman scattering in hydrogen-filled hollow-core photonic crystal fiber," *Science*, vol.

- 298, pp. 399–402, (2002).
28. F. Benabid, J. C. Knight, and P. Russell, “Particle levitation and guidance in hollow-core photonic crystal fiber,” *Opt. Express*, vol. 10, pp. 1195-1203 (2002).
29. T. M. Monro, W. Belardi, K. Furusawa, J. C. Baggett, N. G. R. Broderick, D. J. Richardson, “Sensing with microstructured optical fibres,” *Meas. Sci. Technol.*, vol. 12, pp. 854-858, (2001).
30. J. M. Fini, “Microstructure fibres for optical sensing in gases and liquids,” *Meas. Sci. Technol.*, vol. 15, pp. 1120-1128, (2004).
31. B. J. Eggleton, C. Kerbage, P. Westbrook, R. Windeler, and A. Hale, “Microstructured optical fiber devices,” *Opt. Express*, vol. 9, 698-713, (2001).
32. F. Benabid, F. Couny, J. C. Knight, T. A. Birks and P. Russell, “Compact, stable and efficient all-fiber gas cells using hollow-core photonic crystal fibers,” *Nature*, vol. 434, pp. 488-491, (2005).
33. C. Kerbage and B. J. Eggleton, “Manipulating light by microfluidic motion on microstructured optical fibers,” *Opt. Fiber Technol.*, vol. 10, pp. 133-149, (2003).

## Chapter 2

### Background

#### 2.1 Guiding mechanisms of PCFs

PCFs have a number of novel properties and applications because of their novel guiding mechanisms [1-8]. In Chapter 1, we introduced the two light guiding mechanisms in PCFs: one is modified total internal reflection (index-guiding) [9] and the other is photonic band gap effect (bandgap-guiding) [10-13]. Recently, a hybrid PCF was proposed in which a guided mode can be confined to the core simultaneously by index-guiding and bandgap-guiding [14]. In this section, we will review these light guiding mechanisms.

##### 2.1.1 Index-guiding PCFs

In index-guiding PCFs, because the refractive index of the pure silica core is larger than the average index of the cladding which is made of pure silica and air holes, light is guided in a higher index core by modified total internal reflection from a low effective index cladding, similar to conventional fibers. The schematic of the cross section of a common index-guiding PCF is illustrated in Fig. 2.1 (a). The PCF is made of pure fused silica, the cladding is a 2D photonic crystal air-silica structure; the air holes are arranged in a hexagonal pattern with air hole diameter  $d$  and

hole-to-hole pitch  $\Lambda$ . Fig. 2.1(b) shows the first index-guiding PCF made of pure fused silica, and its far field intensity at the wavelength of 632.8 nm is shown in Fig. 2.2 [9].

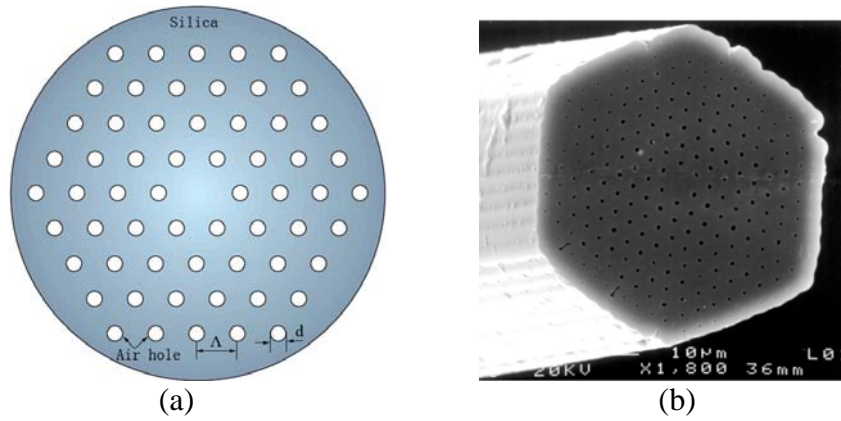


Figure 2.1 (a) The schematic of the cross-section of a common index-guiding PCF; (b) Scanning electron microscopy (SEM) photograph of the first index-guiding PCF with 2-D photonic crystal cladding [9].

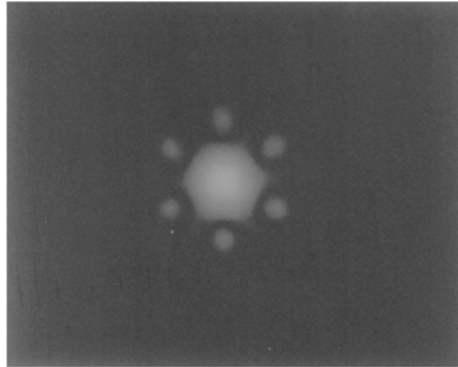


Figure 2.2 Photographed far field pattern of light intensity of the first index-guiding PCF at 632.8 nm [9].

In a conventional single mode fiber (SMF) with core radius  $\rho$  and core and cladding indices  $n_{co}$  and  $n_{cl}$  respectively, there are propagation constants  $\beta$  associated with specific modes in the core which do not propagate in the cladding. It satisfies [15]:

$$kn_{cl} < \beta < kn_{co} \quad (1)$$

where  $k = 2\pi / \lambda$ ,  $\lambda$  is the free-space wavelength. The number of guided modes can

be determined by the  $V$  value [15]:

$$V = \frac{2\pi}{\lambda} \rho \sqrt{n_{co}^2 - n_{cl}^2} \quad (2)$$

which should be less than 2.405 for the fiber to be a single mode. Thus the SMFs are in fact multimode for the light of sufficiently short wavelength. Similarly, for an index-guiding PCF, there are propagation constants  $\beta$  for the core modes which satisfies [15]:

$$\beta_{FSM} < \beta < kn_0 \quad (3)$$

where  $n_0$  is the index of silica (the core material), and  $\beta_{FSM}$  is the propagation constant of the fundamental space-filling mode (FSM). The FSM is the fundamental mode of the infinite photonic crystal cladding if the core is absent, and it corresponds to the maximum  $\beta$  allowed in the cladding. As the lower limit of  $\beta$  in a conventional fiber is  $kn_{cl}$ , the effective cladding index of the PCF can be defined as [15]:

$$n_{eff} = \beta_{FSM} / k. \quad (4)$$

The effective cladding index exhibits strong wavelength dependence, which is very different from that of the conventional fiber.  $n_{eff}$  decreases rapidly with the increase of wavelength, as shown in an example in Fig. 2.3 [16-18].

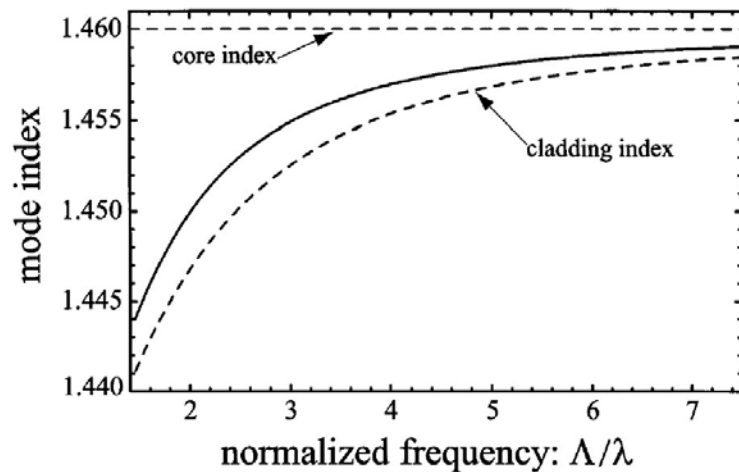


Figure 2.3 Modal dispersion curves extending from 300 nm to 1600 nm for a single mode photonic crystal fiber structure with air hole diameter of 0.6  $\mu\text{m}$  and a pitch of 2.3  $\mu\text{m}$  [16-18].

By analogy with conventional fibers, the effective V value of the PCF ( $V_{\text{eff}}$ ) can be defined as [18]:

$$V_{\text{eff}} = \frac{2\pi}{\lambda} \rho_{\text{eff}} \sqrt{n_o^2 - n_{\text{eff}}^2} \quad (5)$$

where  $\rho_{\text{eff}}$  is the effective core radius. The decrease of effective cladding index at longer wavelengths counteracts the increase in wavelength, thus keeping the V value nearly constant and making it possible for a single-mode to propagate over a remarkably wide wavelength range, sometimes referred to as “endlessly” single mode. When the relative hole diameter satisfies  $d/\Lambda \leq 0.43$ , PCFs are endlessly single mode [18]. There are many different definitions of  $\rho_{\text{eff}}$  [16-20], but if  $\rho_{\text{eff}}$  is defined as  $\rho_{\text{eff}} = \Lambda/\sqrt{3}$ ,  $V_{\text{eff}} \leq 2.405$  can also be used for determining whether a PCF supports a single mode, as shown in Fig. 2.4 [18].

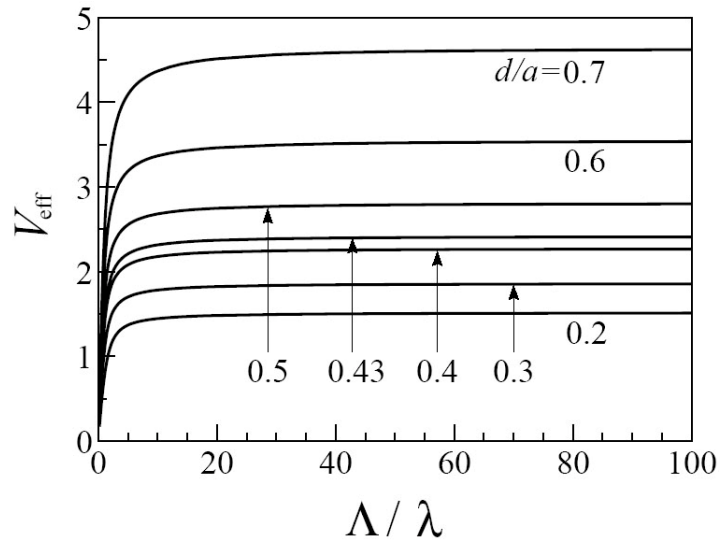


Figure 2.4 Effective V value as a function of normalized frequency for various relative air hole diameter ( $d/a$ ) [18].

An important property that was neglected by previous research is that

bandgap-guiding modes may exist in index-guiding PCFs [21]. When propagation constant  $\beta$  satisfies:

$$\beta < \beta_{FSM} < kn_0, \quad (6)$$

the corresponding modes cannot be guided by total internal reflection. However, when this condition holds and when  $\beta$  is within the region of bandgaps formed by 2D photonic crystal cladding, the modes can exist as bandgap-guiding modes. This will be discussed in the following section.

## **2.1.2 Bandgap PCFs**

### **2.1.2.1 Bandgap theory**

In bandgap PCFs, light is confined to a low-index core or even hollow core by “reflection” from a photonic crystal cladding, which can be a one-dimensional (1D) or two-dimensional (2D) photonic crystal structure, as shown in Fig. 2.5 [22, 23] and Fig. 2.6 [13], and their guided mode distributions are shown in Fig. 2.7(a) and Fig. 2.7(b) respectively. The guiding mechanism of bandgap PCFs is based on the photonic bandgap (PBG) effect [24]. A photonic crystal is a dielectric structure with a refractive index that varies periodically in space, with the period being of the order of optical wavelength. A light wave with special frequencies within the band gap (or stop band) of the photonic crystal cannot propagate through this photonic crystal. If there is a defect in the photonic crystal structure, the light can only propagate in the defect region [24]. For bandgap PCFs, the low-index core (or the hollow core) is the defect of the photonic crystal cladding, thus the light with special frequencies within the bandgap can propagate in the core with low loss by bandgap-guiding.

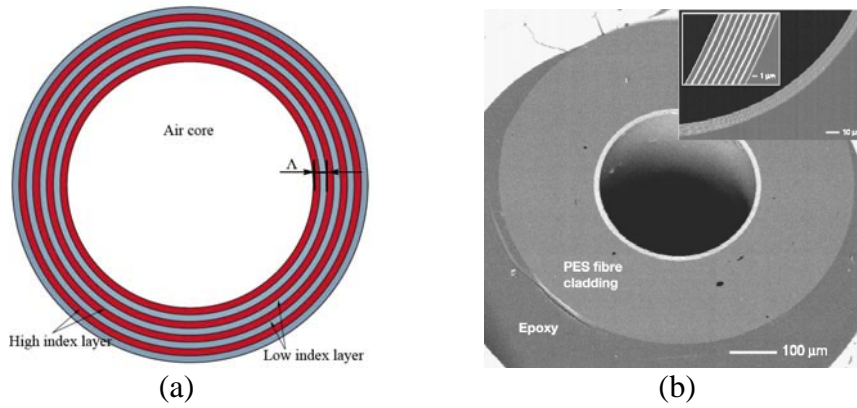


Figure 2.5 (a) The schematic of the cross-section of a hollow-core bandgap PCF with 1D photonic crystal cladding; (b) SEM photograph of the hollow-core PCF with 1D photonic crystal cladding [23].

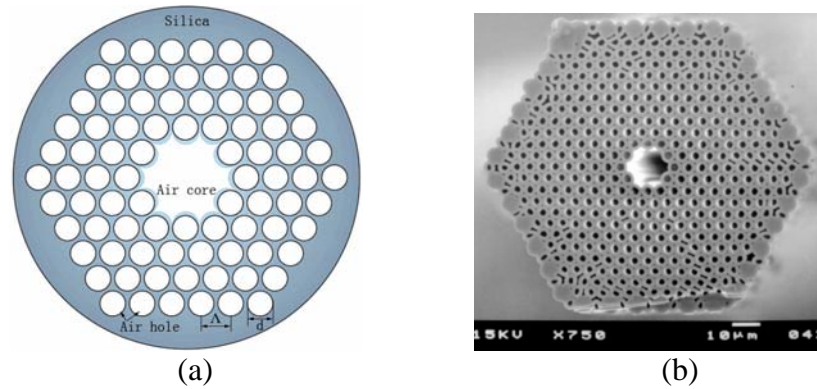


Figure 2.6 (a) The schematic of the cross-section of a hollow-core bandgap PCF with 2D PC cladding; (b) SEM photograph of the first hollow-core bandgap PCF with 2D PC cladding [13].

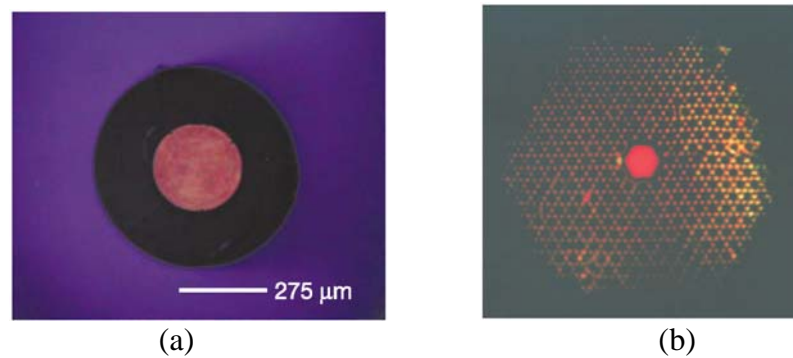


Figure 2.7 (a) Charge-coupled device (CCD) image of light intensity pattern of the hollow-core bandgap PCF with 1D PC cladding at 775 nm [23]; (b) Optical micrograph of the field intensity pattern of the hollow-core bandgap PCF with 2D PC cladding for white light excitation [13].

For 1D bandgap PCFs, which are also named Bragg fibers [10], a hollow core is surrounded by a multilayer cladding that consists of alternating layers having high and low refractive indices, as shown in Fig. 2.5. The index variation along the radius

only has an intrinsic advantage for forming hollow-core fibers: bandgap waveguide is much easier to create theoretically compared to 2D bandgap guiding because 1D bandgap needs much lower index contrast [6]. This makes it possible to form air-guided modes using two materials that would not provide an air-guiding bandgap when disposed in 2D array [6]. Especially, when the index contrast of a 1D bandgap PCF is reasonably high, the omnidirectional guiding can be formed [25-27], as shown in an example in Fig. 2.8. In the red region of bandgap maps, light with certain frequency can be guided in the fiber for all direction [25-27]. However, the use of two solid materials, as required for self-supporting in structure, limits the development of 1D bandgap PCF because two materials, which should have large index contrast and compatible thermal and thermal-mechanical properties for drawing fabrication are required [6, 23].

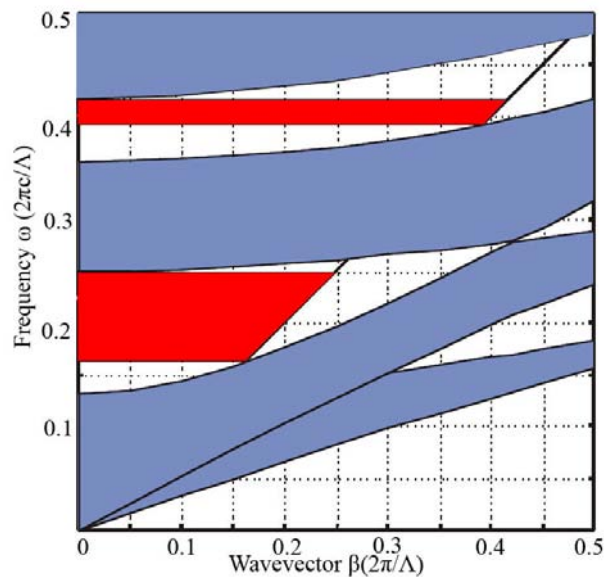


Figure 2.8 Band maps of the bandgap PCFs with 1D photonic crystal cladding. The high and low refractive indices are 4.6 and 1.6 respectively with relative thicknesses of 0.33 and 0.67. The white and red regions correspond to bandgaps where light can propagate in the hollow-core. The thick black line represents the light line. The red regions are two omnidirectional frequency ranges, where light reflects by the cladding from all direction [27].

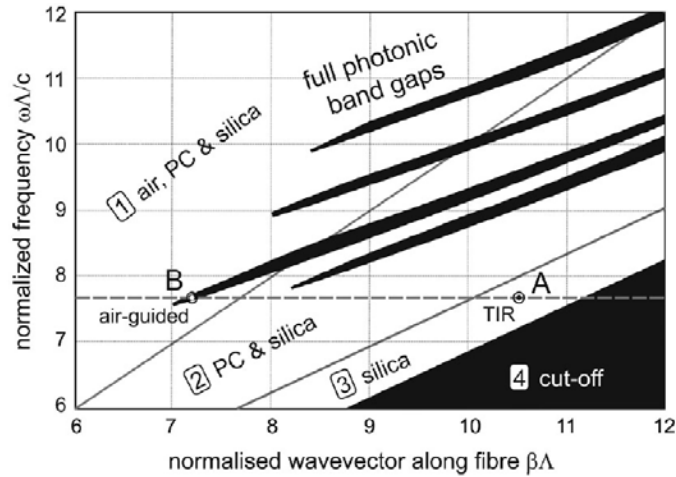


Figure 2.9 Propagation diagram for a 2D bandgap PCF with 45% air-filling fraction. In region (1), light is free to propagate in every region of the fiber (air, photonic crystal, and silica). In region (2), propagation is turned off in the air. In region (3), it is turned off in the air and the photonic crystal. In region (4), light cannot propagate anywhere (cut off) completely. The black fingers represent the regions where full 2D photonic band gaps exist. Guided modes of a solid core PCF form at points such as A, where light is free to travel in the core but unable to penetrate the photonic crystal. At point B, light is free to propagate in air but is blocked from penetrating the cladding by the PBG; these are the conditions required for a hollow-core mode [7, 8, 11].

For 2D bandgap PCFs, as shown in Fig. 2.6, a hollow-core is surrounded by a triangular pattern air-silica structure. When the light is restricted in the transverse plane, 2D bandgap can appear only for large enough index contrasts. For example, the triangular 2D array structure requires an index ratio no less than 2.66 [6, 28]. However, for propagation out of transverse plane, when the longitudinal component of wave vector ( $\beta$ ) is fixed but nonzero, 2D bandgaps can appear for much smaller index contrast such as air (1.0) and silica (1.45) [11]. This air-silica 2D structure can be well fabricated by stack-draw technique. Air is mechanically and thermally compatible with most materials [6], it is transparent over a broad spectral range and it has a very low refractive index. Fused silica is an excellent material for drawing fabrication, so PCFs made of air-silica have been widely studied and developed. What's more, PCFs with air hole structure can be fabricated by different glasses [29-31] or polymer [32-34] materials.

It is the norm to use a propagation diagram to understand 2D bandgap-guiding in PCFs. Propagation diagram for a 2D bandgap PCF with 45% air-filling fraction is shown in Fig. 2.9 [7, 8, 11], the finger-like regions are bandgap regions formed by 2D PC cladding. In principle, at a fixed optical frequency, the maximum value of  $\beta$  is given by  $kn$ , where  $n$  is refractive index of the medium in which light propagates. For  $\beta < kn$ , light is free to propagate; for  $\beta > kn$ , it is cutoff (or it is evanescent). Therefore, for the black region 4 as shown in Fig. 2.9 which satisfies

$$\beta > kn_{silica}, \quad (7)$$

light is cutoff. For the region 3 which satisfies

$$kn_{eff} < \beta < kn_{silica}, \quad (8)$$

light can propagate in the silica (the case of index-guiding PCF). For the region 2 which satisfies

$$k < \beta < kn_{eff} < kn_{silica}, \quad (9)$$

light can propagate in the air-silica PC and silica; for the region 1 which satisfies

$$\beta < k < kn_{eff} < kn_{silica}, \quad (10)$$

light can propagate in the air, air-silica PC and silica. Thus, for the hollow-core bandgap PCF, light with certain frequencies both within the bandgaps and in the region 1 can be guided in the air-core by bandgap-guiding mechanism. Now we study another case, for a solid-core PCF with 2D PC cladding, the light in the region 1 and 2 can not propagate by index-guiding mechanism, however, in these regions, when  $\beta$  with certain frequencies within the bandgaps, the light can be guided in the silica core by bandgap-guiding mechanism, which is neglected by most research on index-guiding PCFs. For certain frequencies, index-guiding and bandgap-guiding can co-exist in solid-core PCFs [21]. As an example, a bandgap-guiding mode in a

solid-core PCF is shown in Fig. 2. 10. Therefore, strictly speaking, it is not always appropriate to refer to solid-core fibers as index-guiding PCFs. However, because the bandgap modes in a solid-core PCF are generally high-order modes and have lobe size, these modes are difficult to be excited, and the loss of the bandgap modes are generally significantly larger compared with that of index-guiding modes, hence they may be neglected in most practical applications.

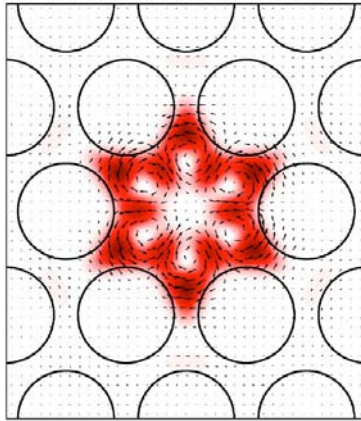


Figure 2.10 A high-order bandgap mode at the wavelength of 1550 nm in a solid-core PCF with 2D PC cladding, where relative hole size  $d/\Lambda=0.8$ , pitch  $\Lambda=3.1 \mu\text{m}$ , effective mode index  $n_{\text{eff}}=1.2289$ , confinement loss is 2.1 dB/m with five cladding air hole rings [21].

Bandgap guiding can also be formed in a solid core surrounded by periodical high index layers or high index rods, as shown in Fig. 2.11(b) and Fig. 2.11(c). One of the key properties of bandgap-guiding mechanism is that guidance can occur in several frequency windows which are defined by a set of bandgaps. Bandgap maps can be numerically calculated by solving the Maxwell equations using full-vector plane wave expansion method [35-36]. Although powerful, this method cannot provide a simple understanding of the physical mechanisms behind the light propagation. For solid-core bandgap PCFs with high-index layers or rods as cladding, the guiding mechanism can be explained intuitively by antiresonant reflecting waveguide (ARROW) model [37-44] besides the bandgap theory.

### 2.1.2.2 ARROW theory

Figure 2.11 shows (a) a planar waveguide with a low-index core ( $n_1$ ) and alternating layers of high ( $n_2$ ) and low ( $n_1$ ) indices; (b) a 1D bandgap PCF with a concentric ring composed of layers with similar indices; and (c) a 2D bandgap PCF with a low-index core ( $n_1$ ) surrounded by high-index ( $n_2$ ) cylindrical inclusions.

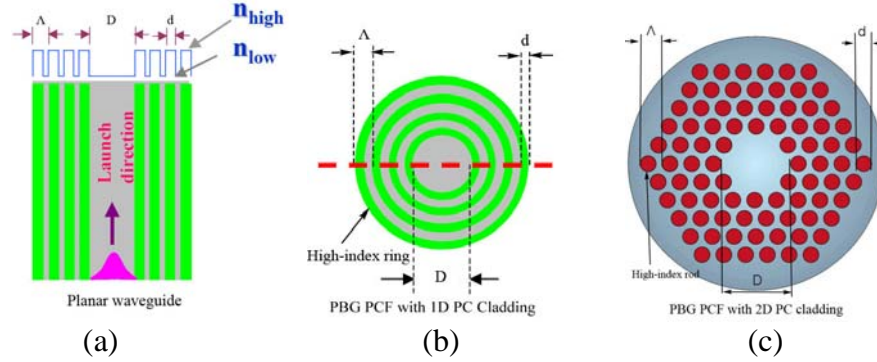


Figure 2.11 Schematic of (a) a 1D ARROW structure, (b) a 1D bandgap PCF with high-index layers, (c) 2D bandgap PCF with high-index rods [40].

For the planar 1D waveguide, as shown in Fig. 2.11(a), the high-index layer on either side of the low-index core behaves as a Fabry-Perot (FP) resonator in the ARROW model. A standing wave by constructive interference builds up in the high-index layer when [40, 41]

$$k_t d = m\pi \quad (11)$$

where  $m = 1, 2, \dots$  and  $k_t = \frac{2\pi}{\lambda} \sqrt{n_2^2 - n_1^2}$  is a transverse component of the propagation vector. This corresponds to a resonant condition in the high-index layer with resonant wavelengths (cutoff condition):

$$\lambda_m = \frac{2d}{m} \sqrt{n_2^2 - n_1^2}, \quad (12)$$

So that the light can leak out of the core, narrowband resonant wavelengths correspond to narrow transmission minima. For other wavelength, FP resonator

causes the light to confine in the core with low leakage as a result of destructive interference in the FP resonance by antiresonant reflection, as shown in Fig. 2.12. It should be noted that the cutoff condition (Eq.12) of this simple ARROW model is valid only in the regime where the high-index layers support modes, thus it is valid only for  $\lambda \leq 2d\sqrt{n_2^2 - n_1^2}$  (so-called “short wavelength regime”). For 1D bandgap PCF as shown in Fig. 2.11(b), the ring waveguide can be regarded as a slab waveguide that is rolled into a tube. So Eq. (12) can also be used to predict the spectral features in the 1D bandgap PCF.

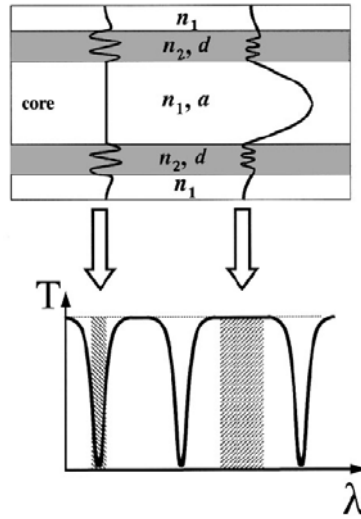


Figure 2.12 Schematic of the ARROW structure (top) and its transmission spectrum (bottom) [38].

For 2D bandgap solid-core PCF, the locations of the transmission minima are determined by the modal cutoff conditions for the modes in the individual high index rods. The modal cutoff condition for HE, TE, TM, and EH modes can be found from the eigenmode equation [40]:

$$J_l(k_t \frac{d}{2}) = 0 \quad (13)$$

where  $J_l$  is the Bessel function of order  $l$ . Using the cosine approximation for

Eq. (13), the resonant wavelength can be written as follows [40]:

$$\lambda_m = \frac{2d}{m+1/2} \sqrt{n_2^2 - n_1^2}, \quad m = 1, 2, \dots \quad (14)$$

Comparing Eq. (12) and Eq. (14), it can be found that the cutoff wavelengths of the 2D bandgap PCF with high-index rods structure are out-of-phase with those of the planar waveguide and 1D solid bandgap PCF with the same parameter  $d$ ,  $n_1$  and  $n_2$  [40]. Thus the ARROW model can give a simple explanation for this kind of bandgap PCFs and approximately predict the property of transmission windows.

### 2.1.3 Hybrid PCFs

For a guided mode, most PCFs confine it by only one of the two different guiding mechanisms, although hybrid-guiding (combination of index-guiding and bandgap-guiding) has been utilized in photonic crystal slabs [45] for many years. Recently, a hybrid PCF was proposed in which a guided mode can be confined in the core simultaneously by index-guiding and bandgap-guiding [14]. As shown in Fig. 2.13, this hybrid PCF was composed of air holes and Ge-doped silica rods disposed around an undoped silica core; the air holes were arranged in a hexagonal pattern as in an index-guiding PCF because it is relatively easy to fabricate by stacking capillary silica tubes and solid silica rods, while the high index rods replaced a single row of air holes along one of the PCF axes.

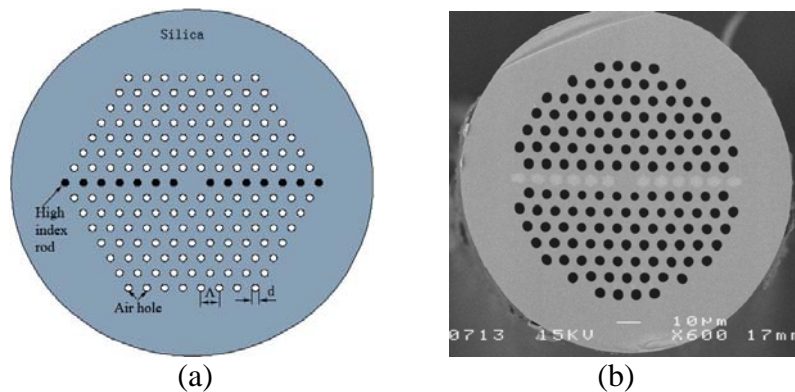


Figure 2.13 (a) The schematic of the cross-section of a hybrid PCF; (b) SEM

photograph of the first hybrid PCF [14].

Along the vertical axis, the core has a higher refractive index than the effective index of the cladding, so light can be guided in the core by index-guiding; on the other hand, along the horizontal axis, index-guiding is impossible because the cladding rods have a higher index than the core; however, light can be confined along the x direction by bandgap guiding (or antiresonant reflection). This hybrid PCF shared properties of both index-guiding and bandgap-guiding. However, the hybrid PCF is a quite new issue; although Cerqueira et al. proposed a kind of hybrid PCF and gave some basic analysis, it was not a systematic investigation that offers insight into the nature of the hybrid PCF, and many significant properties of hybrid PCFs have not been investigated. We will investigate systematically the properties of hybrid PCFs and potential applications in Chapter 6.

## **2.2 Properties and applications of index-guiding PCFs**

Index-guiding PCFs have a number of various micro-structures. The adjustment of the effective refractive index of the cladding via air filling fraction and air hole arrangement has been used for the implementation of small index step, large index step and asymmetric index distribution. Here we will divide index-guiding PCFs into three classes according to their index distribution, as shown in Fig. 2.14.

### **2.2.1 Small index step**

Index-guiding PCFs with small index step generally have small relative hole size ( $d/\Lambda$ ), so light confined in the core will partially distribute into the cladding. One significant property of this kind of PCFs is that the effective cladding index is strongly wavelength dependent.

#### **Endlessly single-mode PCF**

When  $d/\Lambda$  is very small, PCFs can support a single-mode over an ultra-wide

wavelength range. Especially when  $d/\Lambda \leq 0.43$ , the PCFs can be endlessly single mode. For example, an index-guiding PCF with a record level of low-loss (0.28 dB/km) at the wavelength of 1550 nm was achieved by NTT laboratories [46]. And it was used to perform the first successful 19 channel wavelength division multiplexing transmission experiment (190 Gbit/s) through a 5 km long PCF in the 850 nm to 1550 nm wavelength region [46, 47].

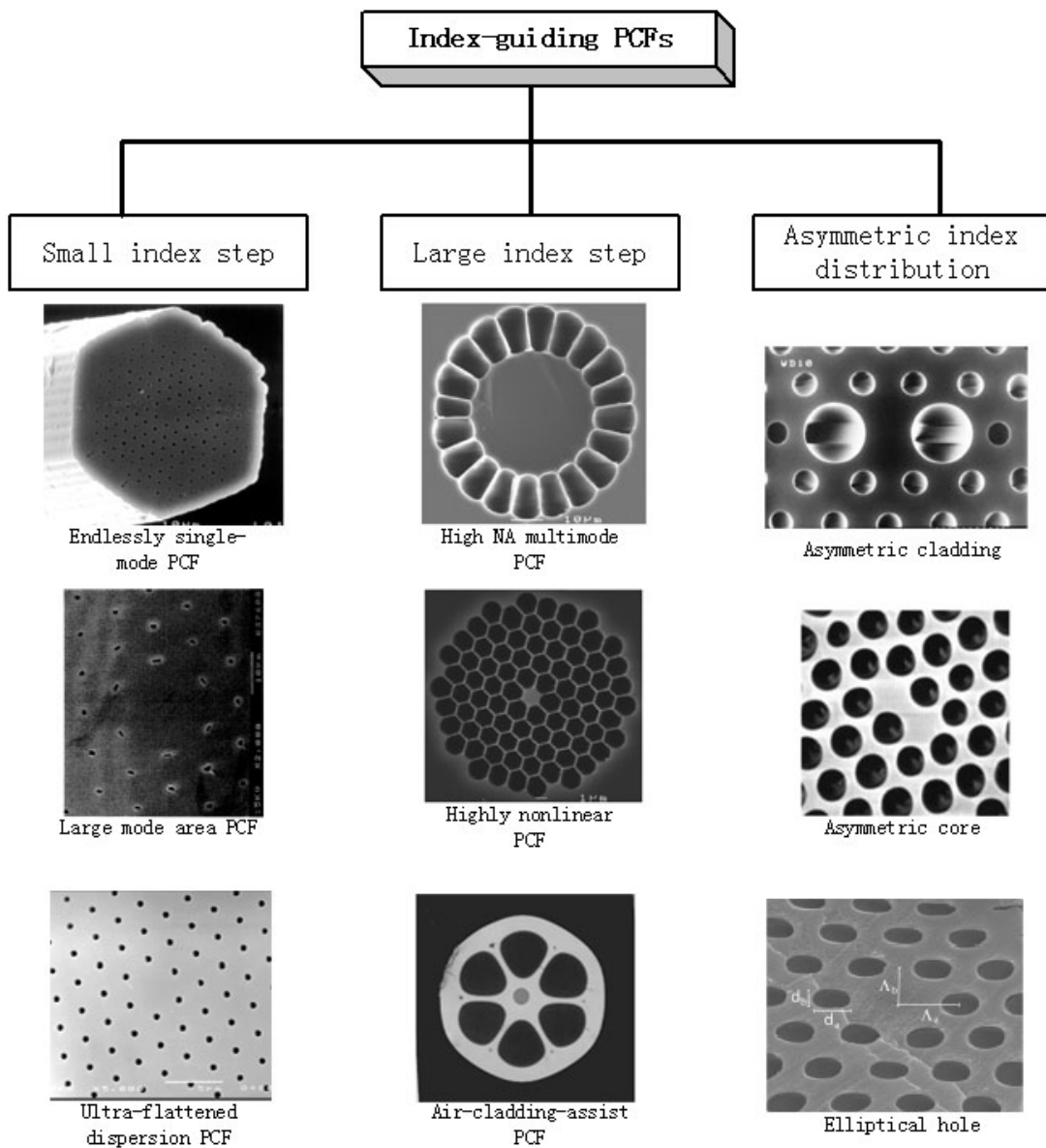


Figure 2.14 Diagram showing the typical structures of index-guiding PCFs.

The single-mode high-bit-rate transmission potential of the PCF was confirmed experimentally over a wide wavelength range from 850 nm to 1550 nm, which corresponds to a bandwidth of 160 THz. Thus an endlessly single-mode PCF can be expected to provide an ultra-wide band of several hundred THz for future optical communication systems with an ultra-large capacity [46, 47].

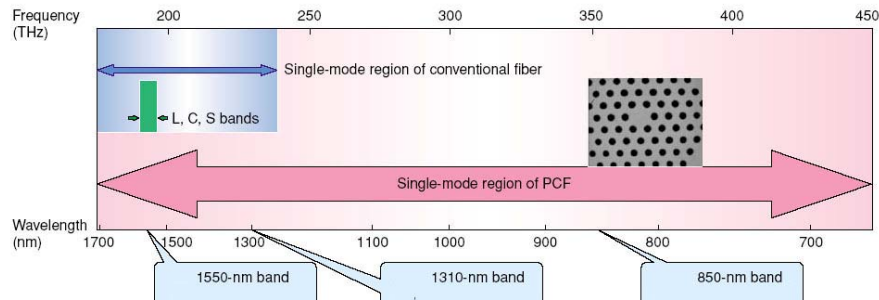


Figure 2.15 Ultrawide band transmission of an index-guiding PCF in NTT laboratories [46].

### Large mode area (LMA) PCF

Single-mode PCFs can be designed to have extremely LMA because, unlike conventional fibers, the number of guided modes in a PCF is independent of the ratio of core radius ( $\rho$ ) to the optical wavelength ( $\lambda$ ). Ultra-LMA single-mode PCF can be achieved by keeping the small relative hole size and large hole-to-hole pitch in a suitable range. Due to ultra-LMA, such PCF can have a rather low energy density in the core in high laser power operation. It has no limitation for the onset of intensity dependent nonlinear effects, and can avoid material damage in high-power fiber lasers. So it can be used for generating and propagating high power laser. Although PCFs and conventional fibers can exhibit similar mode areas at any single wavelength, LMA PCFs have a distinct advantage for broadband and high quality beam applications because of their ability to be single mode with large mode area over a wide wavelength range [48]. In addition, PCFs may simplify the fabrication

of large-mode-area single-mode fibers for use at short wavelengths [48, 49].

### Ultra-flattened dispersion PCF

In conventional fibers, group velocity dispersion (GVD) is usually dominated by the dispersion of the bulk silica. However, PCFs have much flexibility in dispersion management because the waveguide dispersion can be properly adjusted by controlling the air holes size and hole-to-hole pitch. As shown in Fig. 2.16 [50], a suitably designed PCF demonstrated nearly zero ultra-flattened dispersion over a significant wider wavelength range from 1  $\mu\text{m}$  to 1.6  $\mu\text{m}$ . Low ultra-flattened dispersion in a wide wavelength range has a great impact on many engineering applications such as dispersion compensation, wide-band supercontinuum generation, ultra-short soliton pulse transmission and wavelength-division multiplexing transmission [50].

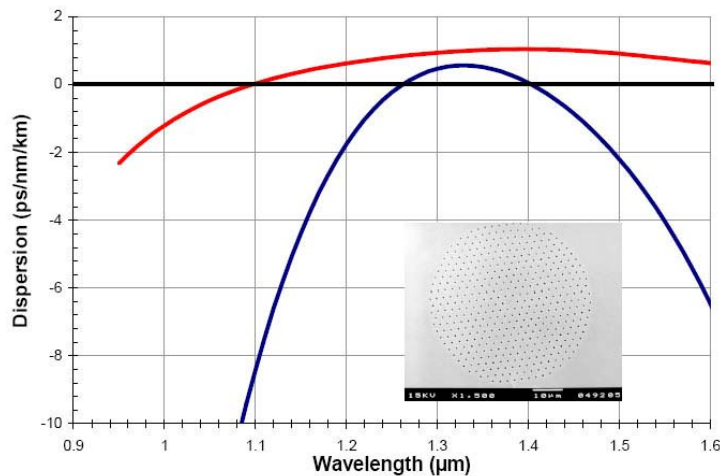


Figure 2.16 Dispersion plots for ultra flattened dispersion PCF. Red curve:  $d=0.58 \mu\text{m}$ ,  $\Lambda=2.59 \mu\text{m}$ ; Dark blue curve:  $d=0.57 \mu\text{m}$ ,  $\Lambda=2.47 \mu\text{m}$  [50].

### 2.2.2 Large index step

Index-guiding PCFs with large index step generally have large relative hole size ( $d/\Lambda$ ) or even air cladding. When the air-filling fraction of the cladding is extremely high, the air-silica structure supports the central rod like a thin silica bridge, the PCF

can behave similarly to a single silica rod surrounded by air.

### **High NA multimode PCF**

The materials of the conventional fiber are generally made of pure silica and silica doped with special materials to change refractive index, so the index contrasts are very limited. For example, the numerical aperture (NA) of Corning SMF-28 is about 0.14 at 1550 nm. The largest NA of conventional fiber is generally not beyond 0.4. However, the PCF can have a much larger NA due to the flexibility in air-silica structure. When the cladding has an air-ring structure, as shown in Fig. 2.14 [51], the average index of the cladding is close to one and thus having a high NA. PCFs with NAs as high as 0.9 have been demonstrated [51]. High NA fibers collect light very efficiently from a very broad space angle and distribute light in a broad angle at the output end; it can be widely used in endoscopy, high power cladding pumping lasers and amplifiers [52-54].

### **Highly nonlinear PCF**

Highly nonlinear PCFs, as shown in Fig. 2.14, have a high air-filling fraction cladding and a small core. The overall shape of the dispersion curve of this kind of PCF can be well approximate by assuming that the fiber behaves as an isolated micro-silica rod in air. The zero-dispersion wavelength point shifts strongly towards the visible wavelength when the core diameter decreases [55]. The small mode area resulting in high power density in the core and visible wavelength zero-dispersion make this kind of PCF very useful for nonlinear applications. It can be used as super-continuum generation for frequency metrology, spectroscopy or optical coherence tomography; four-wave mixing and self-phase modulation for switching; soliton generation and propagation, ultra-short pulse compression; wavelength conversion applications; raman amplification and so on [56-59]. An example is

given in Fig. 2.17, whereby an ultra-broadband continuum extending from 390 to 1600 nm was generated by injecting pulses of 100 fs duration, 800 pJ energy, and a center wavelength of 790 nm into a 75 cm length of a highly nonlinear PCF [56].

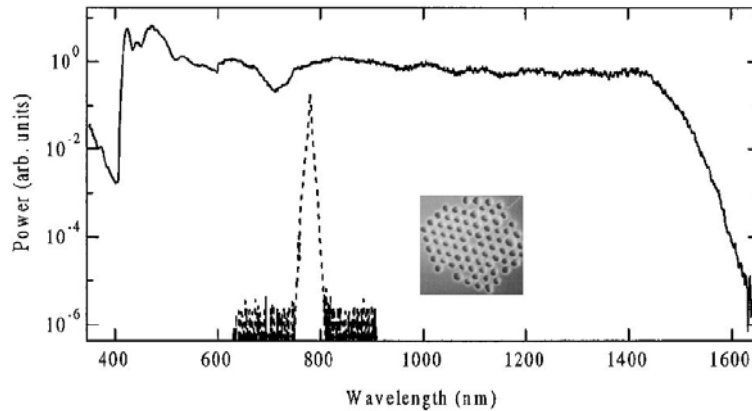


Figure 2.17 Optical spectrum of the continuum generated in a 75 cm length small-core nonlinear PCF. The dashed curve shows the spectrum of the initial pulse. The PCF has a core with diameter about 1.7  $\mu\text{m}$  and air holes with diameter 1.3  $\mu\text{m}$ . The calculated zero-dispersion wavelength of the PCF is 767 nm [56].

### Air-cladding-assist PCF

Air-cladding-assist PCFs can be explained as adding air holes in the cladding of conventional doped-core fibers. One of the air-cladding-assist PCF, called grapefruit PCF, as shown in Fig. 2.14 [60], is comprised of six approximately cylindrical air-holes introduced in the cladding. The diameter of air holes is about 40  $\mu\text{m}$ . The inner cladding region formed by air holes is about 34  $\mu\text{m}$  in diameter. The core is germanium (Ge) doped, has a diameter of about 8  $\mu\text{m}$  and with  $\Delta = (n_1 - n_2)/n_1 \sim 0.35\%$ , where  $n_1$  and  $n_2$  are the refractive indices of the Ge core and the silica respectively. This PCF can guide light in the Ge-doped core like a conventional SMF, however, the inner cladding surrounded by air holes can guide core modes when the PCF is tapered, or can guide excited cladding modes when the core is written with grating. The big air holes can be filled with polymer or micro-fluids, which results in many all-fiber optical devices, such as tunable filter, tunable

attenuator and polarization controller [61-64]. We will pay further attention to it in the following sections. Furthermore, air-cladding-assist PCFs have a very small bending loss. For example, the fiber has a low bending loss of 0.05 dB/turn with a bending diameter of 10 mm, which is less than 1/500 of that of conventional SMFs. It can be used as optical indoor cord [65].

### 2.2.3 Asymmetric index distribution

In the case of asymmetric index distribution, polarization maintaining (PM) PCF or single-polarization PCF can easily be achieved by controlling air hole size in two orthogonal directions. The large index contrast of the PCFs in combination with asymmetric core or cladding may be used to create modal birefringence of at least one order of magnitude larger than conventional PM fibers [66, 67]. As an example in Fig. 2.18 [68], a PM PCF was designed by introducing asymmetric air holes in two orthogonal directions. The modal birefringence of the PCF can be as high as  $1.4 \times 10^{-3}$  at the wavelength of 1550 nm with a low confinement loss of 1.3 dB/km.

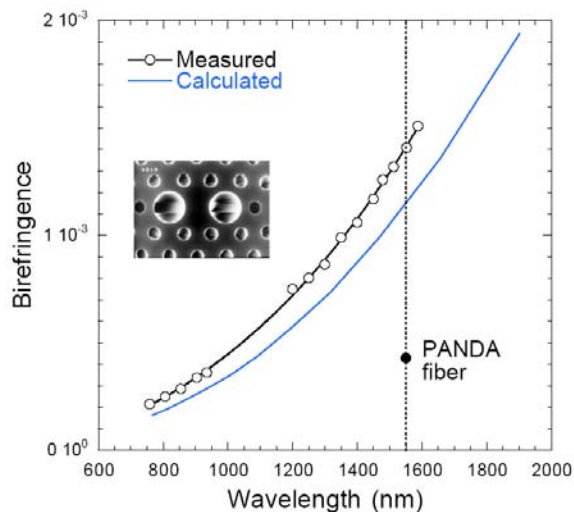


Figure 2.18 Wavelength dependence of PM-PCF birefringence.

The highly birefringence can also be achieved by designing asymmetry core [67] or elliptical holes [69, 70], as shown in Fig. 2.14. Single-polarization PCF can be

realized by designing PM PCF with large polarization dependent loss [71, 72]. Unlike traditional PM fibers which contain at least two different glasses each with a different thermal expansion coefficient, the birefringence of PCFs is highly insensitive to temperature, which is important in many applications. For example, temperature effects in the highly stressed conventional high birefringence fiber limit the accuracy of fiber optic gyroscopes, as well as current sensors based on spun elliptically polarizing optical fiber, which can be significantly improved using PM PCFs [73].

### **2.3 Properties and applications of bandgap PCFs**

As mentioned in the section 2.1, Bandgap PCFs can guide light by 1D or 2D bandgap effects; and light can be confined in a solid-core or a hollow-core. Here we will divide bandgap PCFs into two classes: 1D bandgap PCF and 2D bandgap PCF, as shown in Fig. 2.19.

#### **2.3.1 1D bandgap PCF**

1D bandgap PCFs (Bragg fibers) were first proposed theoretically in 1978 [10], and they began to attract much interest and fabrication commenced after a number of years.

##### **Solid-core 1D bandgap PCF**

The solid-core 1D bandgap PCF was first fabricated using modified chemical vapour deposition (MCVD) technique in 2000 [74]. The central core was made of F-doped silica ( $n_1=1.449$  at  $\lambda_0=1.06$  nm), the high index layers of the cladding were made of Ge-doped silica ( $n_2=1.457$  at  $\lambda_0$ ), the low index layers were pure silica ( $n_3=1.45$  at  $\lambda_0$ ). The fiber was drawn to obtain a core radius of 5  $\mu\text{m}$ . This PCF can confine light at the wavelength of 1.06 nm in the low index core by the bandgap effect and has a zero-dispersion at 1.06  $\mu\text{m}$ . It can be used in nonlinear optics such

as parametric amplifier or oscillator applications. Later, a single-mode 1D bandgap PCF was fabricated with large mode area ( $517 \mu\text{m}^2$ ) and low loss ( $0.4 \text{ dB/m}$ ) at the wavelength  $1.55 \mu\text{m}$ , which can be used in high power laser delivery [75]. The transmission loss was further improved to a few dB/km [76]. The solid core 1D bandgap PCF can also be fabricated using sputtering technique [77], the PCF was fabricated by forming dielectric multilayers Si/SiO<sub>2</sub> on the outside of a taped conventional SMF, as shown in Fig. 2.19. Such PCFs can be used as compact nonlinear devices and dispersion control components.

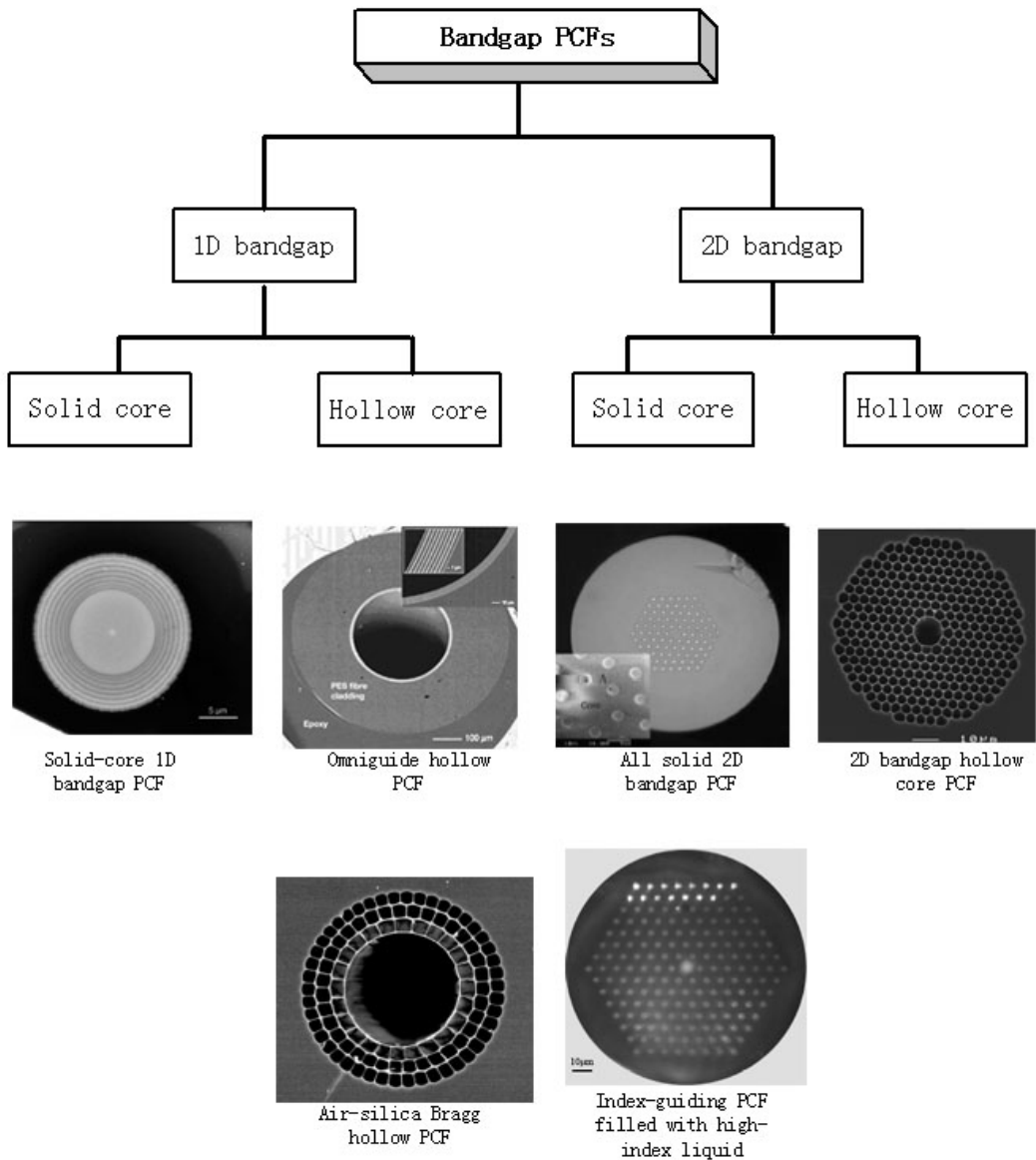


Figure 2.19 Diagram showing the typical structures of bandgap PCFs.

### **Hollow-core 1D bandgap PCF**

The hollow-core 1D bandgap PCF was first fabricated using thermally evaporated coating technique in 1999 [22]. The light can be guided in the hollow-core by omnidirectional bandgap guiding. Later, it was improved using a roll-draw technique and thus a hollow-core omni-guiding PCF was demonstrated, as shown in Fig. 2.19 [23]. The multilayers of this PCF are made of two materials: a chalcogenide glass with index of about 2.8, arsenic triselenide ( $\text{As}_2\text{Se}_3$ ), and a high glass-transition thermoplastic polymer with index of about 1.55, poly ether sulphone (PES). The bulk material  $\text{As}_2\text{Se}_3$  has a transmission loss of about 7 dB/m at 10.6  $\mu\text{m}$ , and the polymer PES has a transmission loss larger than 100,000 dB/m at 10.6  $\mu\text{m}$ . However, the hollow-core PCF made of them has a low loss of 0.95 dB/m at 10.6  $\mu\text{m}$ , which is an order of magnitude lower than the intrinsic fiber material losses. Therefore, it demonstrated that low attenuation can be achieved through structural design rather than high-transparency material selection. Another kind of 1D hollow-core Bragg fiber is air-silica ring structure, as shown in Fig. 2.19 [78]. The three silica cladding layers can be represented by concentric silica rings with the thickness about 0.20  $\mu\text{m}$ , which are separated by 2.3  $\mu\text{m}$  thick air rings comprising supporting nanoscale silica bridges of about 45 nm thick. The loss of this PCF is about 1.5 dB/m at 1.4  $\mu\text{m}$ . The potential advantage of air-silica 1D Bragg fibers is ultra-wide bandgaps [78]. Because light propagates mostly in the air in hollow-core PCFs and it is not limited by the material, they have great potential in low loss transmission for special wavelengths and high power delivery applications.

### **2.3.2 2D bandgap PCFs**

The theory of 2D bandgap PCFs was first proposed in 1995 [11], and then the first

solid-core and hollow-core 2D bandgap PCFs were fabricated in 1998 and 1999 respectively [12, 13].

### **Solid-core 2D bandgap PCF**

The first solid-core 2D bandgap PCF was made by introducing an extra small air hole in the central silica core surrounded by an air-silica cladding with honeycomb pattern, so the central core has a lower average index compared with the cladding. The light with special frequencies in the bandgap can be guided in silica part of the core by bandgap effect, as shown in Fig. 2.20 [12].

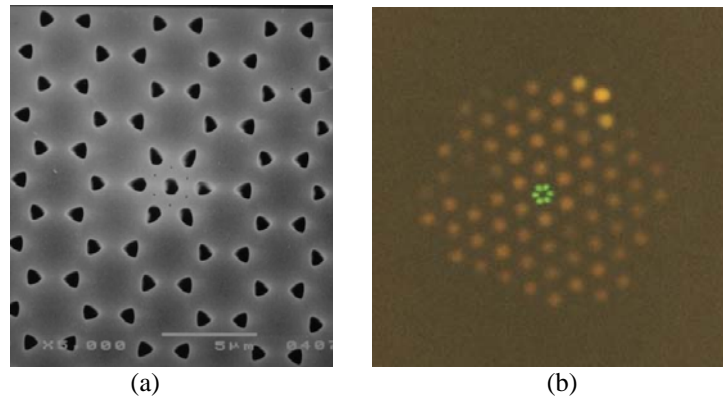


Figure 2.20 (a) SEM photograph of the first solid-core bandgap PCF with 2D PC cladding. (b) Optical micrograph of the field intensity pattern of the solid-core bandgap PCF with 2D PC cladding for white light excitation [12].

Several solid-core 2D bandgaps were invented in the following years [79-82]. For example, all-solid 2D bandgap PCFs were fabricated, as shown in Fig. 2.19. The PCF has high-index glass rods (or Ge-doped silica rods) arrayed in a hexagonal pattern in the background of pure silica. Later, the minimal loss of about 2 dB/km was achieved [80]. This kind of PCF may match the group indices at widely different wavelengths because of the presence of multiple bandgaps [79]. And bandgaps can exist even when the index contrast of high-index rod and background silica is fabricated to be as low as one percent [81]. Another kind of solid core 2D bandgap PCF can be realized by filling all air-holes of an index-guiding PCF with high-index fluids such as liquid, liquid crystal or polymer, as shown in Fig. 2.19

[82]. For this kind of PCFs, bandgap-guiding can be tuned by changing the index of fluids, which can be used as fiber tunable filters or switches [82].

### **Hollow-core 2D bandgap PCF**

Since the first hollow-core 2D bandgap PCF was demonstrated (Fig. 2.6(b)), it has been improved dramatically and became the most successful hollow-core bandgap PCF. The typical structure of this PCF is shown in Fig. 19. The transmission loss has been brought down to as low as 1.2 dB/km, the lowest loss of all hollow-core fibers [83]. Hollow-core PCFs confine light mostly to the air core and avoid losses of fundamental scattering and absorption of silica in conventional fibers. The loss may be further reduced and it may be used in future telecommunication transmission. This kind of hollow core PCF can be used to reduce the thermal sensitivity of a fiber optic gyroscope compared with conventional fibers [84, 85]. It can also be used in high power laser delivery and high power pulse transmission because of extremely low nonlinearity in the PCF. The anomalous dispersion of this bandgap PCF can benefit the generation of high power optical solitons [86]. The PCF with high beam intensity, long interaction lengths and good-quality transverse beam profile offers a perfect performance for gas-based nonlinear optics [87, 88], and atom or particle guidance [89, 90]. For the same reasons, it can also be used in highly sensitive gas and liquid sensors [91, 92].

## **2.4 Modified and combined structure PCFs**

### **2.4.1 Modified-structure PCFs**

The performance of PCFs can be optimized by locally adjusting the sizes, shapes and positions of the micro-holes to achieve special functions. Here three examples are given.

#### **Improved evanescent-field PCF**

Index-guiding PCFs have evanescent fields distributed into the air holes which can be used for gas sensors when the gas is filled into the air holes. Overlap is the fraction of optical power that is exposed to the gas samples. Because light is mostly confined in the central silica core, the overlap is very limited, thus the sensitivity of this PCF sensors is not very high. When a small-hole is introduced in the central silica core, as shown in Fig. 2.21 (a), the overlap can be improved dramatically, thus increasing the sensitivity [92].

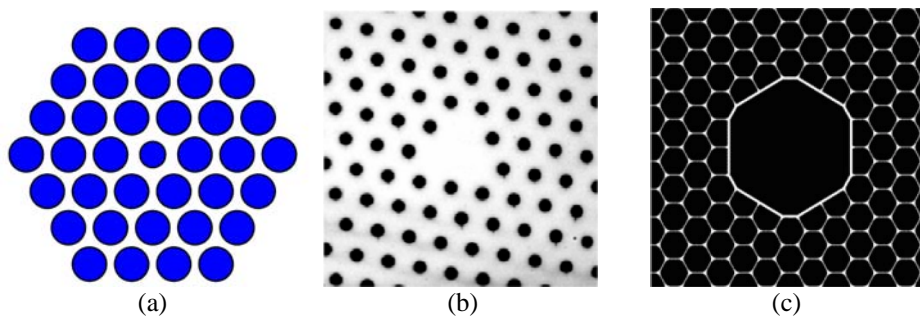


Figure 2.21 (a) Schematic of an improved evanescent-field PCF [92], (b) SEM photograph of an improved LMA PCF [93], (c) Schematic of an improved low-loss hollow-core PCF [94].

### Improved LMA PCF

When a common index-guiding PCF is scaled up by increasing hole-to-hole pitch to achieve large mode area, it is at the cost of increased susceptibility to longitudinal modulations such as microbending and macrobending. A triangular core formed by three missing neighboring air holes, as shown in Fig. 2.21(b), considerably improves the mode area without a corresponding change in the loss level for the same hole-to-hole pitch. An enhancement of the mode area by about 30% by this modification has been achieved [93]. It has important applications in high power fiber lasers [54].

### Improved low-loss hollow-core PCF

The loss limitations in hollow-core bandgap PCFs are set by hole interface

roughness, the roughness is primarily due to thermally excited surface capillary waves which become frozen-in when the glass solidifies. Since the level of hole interface roughness appears to be an intrinsic property of the fiber drawing process and cannot be reduced substantially, decreasing the modal field strength at the interface of the air core is an effective way to improve loss property. As shown in Fig. 2. 21(c), the silica interface surrounding the air core has a specially designed thickness which satisfies the antiresonant reflection condition. At antiresonance, the field intensity has a minimum at the interface of the air core, thus decreasing the loss caused by interface roughness [94]. The field intensity at the silica/air core interfaces is shown to be reduced by a factor of approximately three compared to a PCF without changing the thickness of the interface. The effect, acting to reduce the fraction of light power in the silica, also reduces nonlinearity, which is important in the delivery of high power short pulse applications.

#### **2.4.2 Combined-structure PCFs**

The combination of various PCF structures can improve the performance of the fibers and produce multifunctional fibers. Three examples are given below.

##### **Double-cladding index-guiding PCF**

The combination of LMA PCF structure and high NA multimode PCF structure can be used in high power fiber amplifiers and lasers. As shown in Fig. 2.22 (a) [52], the PCF has two claddings: the outer cladding is a high-NA air cladding surrounded by silica jacket, which is advantageous for the efficient use of high power and low brightness pumping light; the inner cladding comprises air holes with small relative hole size, which can realize high power and single-mode signal laser in the doped-core without limitation of nonlinearity and material destruction because of LMA. A 2.3 meter long air-clad Yb-doped LMA PCF laser generating up to 80W

output power with a slope efficiency of 78% has been achieved [54].

### Double-cladding bandgap PCF

The low-index contrast all-solid bandgap PCF has a large bending loss, which can be improved by adding a ring of air holes around the all-solid bandgap structure, as shown in Fig. 2.22(b). The confinement loss and bending loss can be significantly reduced [95]. The method can also be utilized in other kind of PCFs to improve the confinement performance, such as birefringent PCFs [96].

### Self-monitoring PCFs

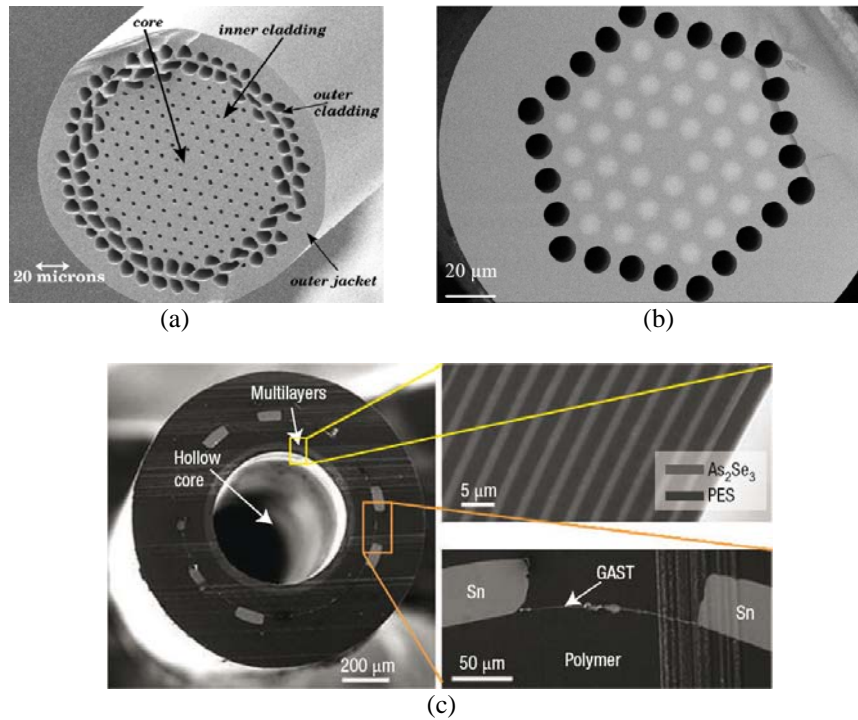


Figure 2.22 (a) SEM photograph of an air-clad Yb-doped PCF [52], (b) SEM photograph of a double-cladding bandgap PCF [95], (c) SEM photograph of a self-monitoring-PCF cross section highlighting the different structures integrated into the fiber. The inset on the lower right shows the thermally sensitive MSM junction. The upper right inset shows the 1D bandgap hollow core structure designed to guide CO<sub>2</sub> laser [97, 98].

The 1D hollow-core bandgap fibers can be used for transmitting high optical power with applications in industrial and medical fields. As the power carried in such fibers increases, the potentially adverse effects of inadvertent release of this

energy increase, thus predicting imminent failure is needed for safety. As shown in Fig. 2.22(c), a hollow core bandgap PCF, designed to transmit a high power CO<sub>2</sub> laser beam, is combined with a thin-film heat-sensing metal-semiconductor-metal (MSM) device whose conductivity depends on the peak temperature. The energy released at the localized defect significantly raises the temperature of the fiber in the vicinity of the defect, which decreases the resistance of the semiconductor layer and produces a large current in the MSM and the current can be monitored when there is a localized defect case.

## **2.5 Combination PCFs with new materials: fruitful applications**

The micro-hole of PCFs can allow for the infusion of materials, thus the combination of PCFs with new materials provides a new platform for a number of ultra-compact photonic devices and applications. The fiber optic systems generally use a variety of in-line components such as modulators, attenuators, filters, etc. These in-line components are typically produced by coupling the light out of the optical fiber and into some bulk or integrated optical waveguide device and then back into the optical fiber, as shown in the upper figure in Fig. 2.23(a). However, the coupling lenses and bulk optical devices make the optical system complicated. A PCF filled with functional material can be integrated with conventional fibers to be an in-fiber component, thus causing ultra-compact photonic devices to be possible. As an example, Fig. 2.23(b) shows a photograph of a 5-m-long hydrogen-filled hollow-core PCF gas cell, illustrating its size compared to that of a match, which can be used as an ultra-compact device for the generation of Raman scattering with low threshold and high efficiency [99]. We can divide the applications into two classes according to the filling materials: PCF with gases and PCF with fluids.

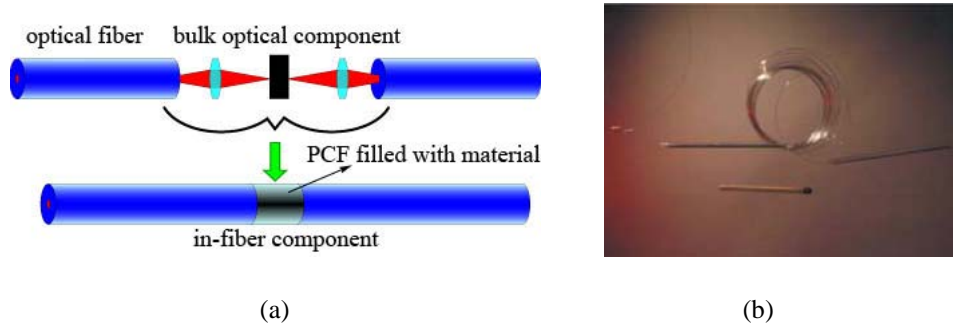


Figure 2.23 (a) Schematic of in-fiber component is made of a PCF filled with material. (b) Photograph of a 5-m-long hydrogen-filled hollow-core PCF gas cell [99].

### 2.5.1 PCF with gases

#### Gas sensors

The advantages of evanescent field fiber sensing include potentially easy alignment with transmission fibers, long interaction length and distributed sensing capability. The improvement of evanescent fields exposed to air holes compared with conventional fiber benefits PCFs in gas sensor applications [100]. For example, an index-guiding PCF with the relative sensitivity of about 6% has been achieved, which is 50 times better than that of D-shaped fiber and 65 times better than that of conventional SMF. For hollow-core bandgap PCFs, the relative sensitivity can be as high as 95% because the bandgap PCF has a much higher percentage of light power in the hollow core that interacts with the gas sample and hence a better sensitivity is achieved [91].

#### Gas-based nonlinear optics

The hollow-core bandgap PCF with high beam intensity, long interaction lengths and single-mode transverse beam profile can provide strong nonlinear interactions between light and gases for gas-based nonlinear optics. It can be widely used in stimulated Raman scattering, high harmonic generation, and electromagnetically induced transparency, etc [87, 88]. For example, the threshold power for rotational

Raman scattering in hydrogen was reduced by more than a million times using a hollow-core bandgap PCF, and near-perfect quantum efficiency was achieved [8].

## **2.5.2 PCF with fluids**

### **Liquid sensors**

When air holes of PCFs are filled with liquid samples, it can be used as liquid sensors [92]. For example, an evanescent field method to detect fluorophore-labeled bio-molecules in aqueous solution using hollow-core bandgap PCFs was demonstrated [101]. In this method, the liquid sample was filled into all the holes of PCFs with a length of 10 cm using capillary force. When the sample contained the labeled bio-molecules, light was guided in the silica segments located in the air-silica cladding and had strong penetration into the sample at frequencies in visible range. And then the transmission spectrum of the fiber was measured. The transmission spectrum showed dips at wavelengths corresponding to the labeled bio-molecules. The fraction of the optical field of the cladding mode that propagated in the aqueous sample was 5.2% for the light with 650 nm wavelength. The minimum concentration which could be detected is  $0.1\mu\text{M}$  for a PCF with 30 cm length. The advantage of the PCF-based liquid sensor is the possibility of achieving long effective interaction lengths while using submicroliter sample volumes. An improved method is the use of a hollow core bandgap PCF with its central core filled with samples for absorption measurements. For liquid samples, near-unity light/sample overlap over a wide range of wavelengths can be obtained, which will significantly improve the absorption measurement sensitivity [92].

### **Liquid-based nonlinear optics**

When the central hollow-core of a bandgap PCF is filled with functional liquids, it can be interacted with pumping laser strongly in the core for a long length, thus

increasing nonlinear effect. For example, it can be used in two photon fluorescence [102], stimulated Raman scattering [103] and supercontinuum generation [104] by filling various liquids.

### **Tunable photonic devices**

The air-holes of PCFs allow for the infusion of active materials yielding novel hybrid tunable all-fiber optical devices that exhibit desirable properties, such as enhanced tunability, compactness, and intrinsic low insertion loss. For example, air-clad-assist PCFs filled with fluid can be utilized as tunable attenuator [63], tunable filter [62] and tunable birefringent fiber [64]. As shown in Fig. 2.24 (a), one part of the PCF is tapered and high-index liquid is filled near the tapered region. When the capillary tube heats the air channels in the PCF which is sealed on both sides using the fusion splicer, it induces pressure and pushes the fluid into the waist of the PCF, thus the light is lost. When the heater is turned off, the fluid goes back and does not affect the transmission of light in the fiber. The PCF behaves as a broadband attenuator with a switching speed of about 0.5 s and an attenuation of 45 dB. As shown in Fig. 2.24 (b), the long period grating (LPG) is written in the PCF and the low-index fluid is filled in the LPG region, and the set-up can be used as a tunable filter when the resonance wavelength changes with the index of the fluid. In Fig. 2.24 (c), when the PCF is filled with high-index polymer only in the two opposite holes in the tapered region, the birefringence can be tuned by changing the index of the polymer via temperature. Furthermore, thermally, electrically and optically tunable PCF devices based on liquid crystals have been demonstrated [82, 105-107].

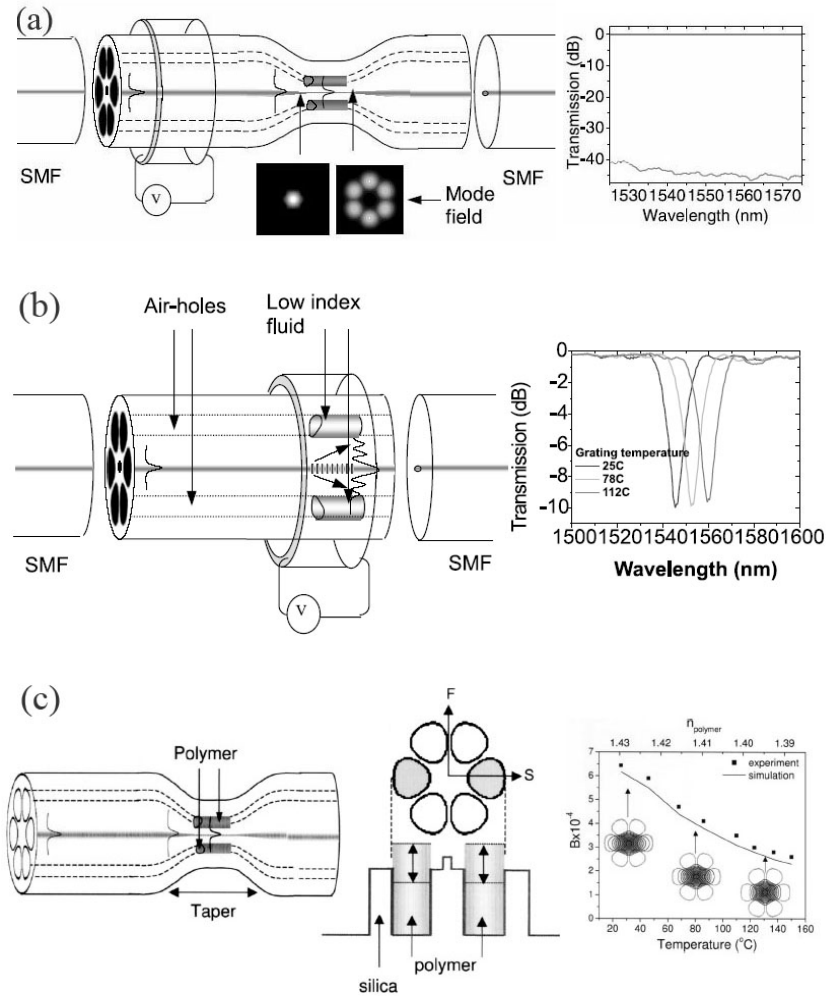


Figure 2.24 (a) Schematic of tunable attenuator. Fluid is moved to the waist of the tapered PCF when the voltage is on; light is lost due to refraction into the high index material [63]. (b) Schematic of tunable filter. The PCF has low-index fluid infused on the grating region; when the voltage is on, the refractive index of the fluid decreases and results in shifting the wavelength resonance [62]. (c) Schematic of tunable birefringence. Birefringence of the PCF increases as a function of the index of the polymer that is filled into two opposite holes of the PCF [64].

## 2.6 Overview of PCF splice techniques

PCFs have huge potential advantages over conventional fibers in various areas as described above. However, in practical applications, PCFs or PCF-based photonic devices generally need to be spliced to conventional fibers for integrating them into existing fiber optic systems. Connecting PCFs to conventional fibers without incurring too much loss is a challenging problem, which limits the applicability of PCFs. Below we provide a detailed review on previous PCF splice techniques.

### 2.6.1 Splicing PCFs with doped core

PCFs with doped core will guide light even when the air holes have completely collapsed during splicing, thus a suitable designed cladding hole-assist PCF, as shown in Fig. 2.14, can be spliced to a conventional SMF with a low splice loss. The following procedure was performed when splicing such PCFs [61]: The air holes were collapsed using heat without applying tension, and the heat source was scanned along the PCF until the air holes collapsed along a length of 6 mm. The full collapsed region was spliced to a conventional Corning SMF-28, as shown in Fig. 2.25 [61]. The splice loss was about 0.075 dB. Another doped-core PCF with similar structure is used in telecommunication transmission with low bending loss. It has a mode field matching with SMF-28. The optimized butt-coupling loss between this PCF and conventional SMF is about 0.126 dB, and the splice loss can be as low as 0.022 dB using a fusion splicer, which is the same as the fusion loss between conventional SMFs [65]. However, PCFs with doped-core will limit the flexibility in their design. Most PCFs are designed as air-silica structures with pure silica material, and this method cannot be used for these PCFs.

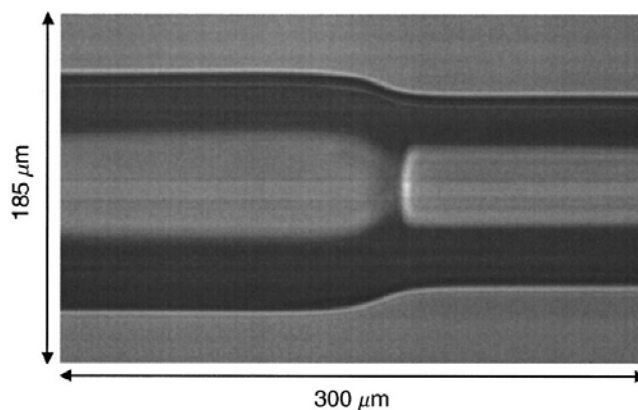


Figure 2.25 Fusion splicing between an air-cladding assist PCF with collapsed air holes (right-hand side) and a standard SMF (left-hand side). The splice loss is about 0.075 dB [61].

### 2.6.2 Splicing PCFs using CO<sub>2</sub> lasers

It was reported that a solid-core PCF and a SMF having similar mode field diameters (MFDs) were spliced using a CO<sub>2</sub> laser. The splice loss was achieved in the range from 1.3 dB to 2.8 dB, as shown in Fig. 2.26. The authors mentioned that the advantages of using a CO<sub>2</sub> laser were that it could clear the solution trapped in the air-holes, clean the fiber surface during the preheat process and not cause any damage to the end of the PCF when splicing [108, 109]. However, these advantages can be easily achieved by using a fusion splicer. There have not been any reports that demonstrate that a CO<sub>2</sub> laser can be used to low-loss splice other types of PCFs.

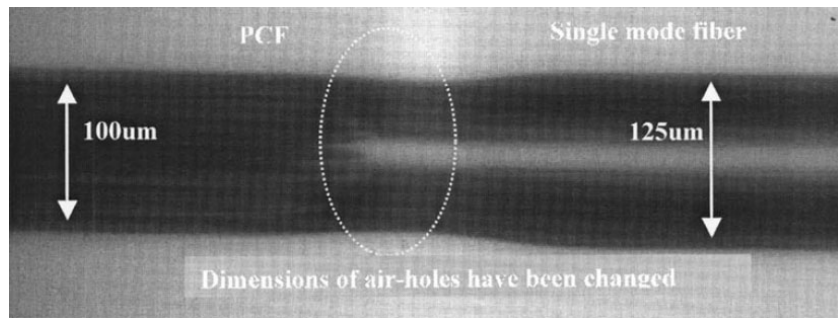


Figure 2.26 Splice between a PCF and a conventional SMF using a CO<sub>2</sub> laser [109].

### 2.6.3 Splicing PCFs using GRIN fiber lens

Low-loss high-strength splice between a solid-core PCF and a SMF having similar MFDs was achieved by using a gradient-index (GRIN) fiber lens, as shown in Fig. 2.27 [110]. A GRIN fiber lens was used to replace a bulk optic lens to couple light between a SMF and a PCF. A low splice loss of 0.44 dB between PCF/SMF was achieved and the mechanical strength can withstand a stress of up to 100-kpsi. However, three splices and controlled lengths of fiber lens and coreless pure fiber are required per connection, which makes this method quite complicated in practical operation. And this approach is suitable only for PCFs that have MFDs larger than 3.5 μm, which can not be used for small-core PCFs.

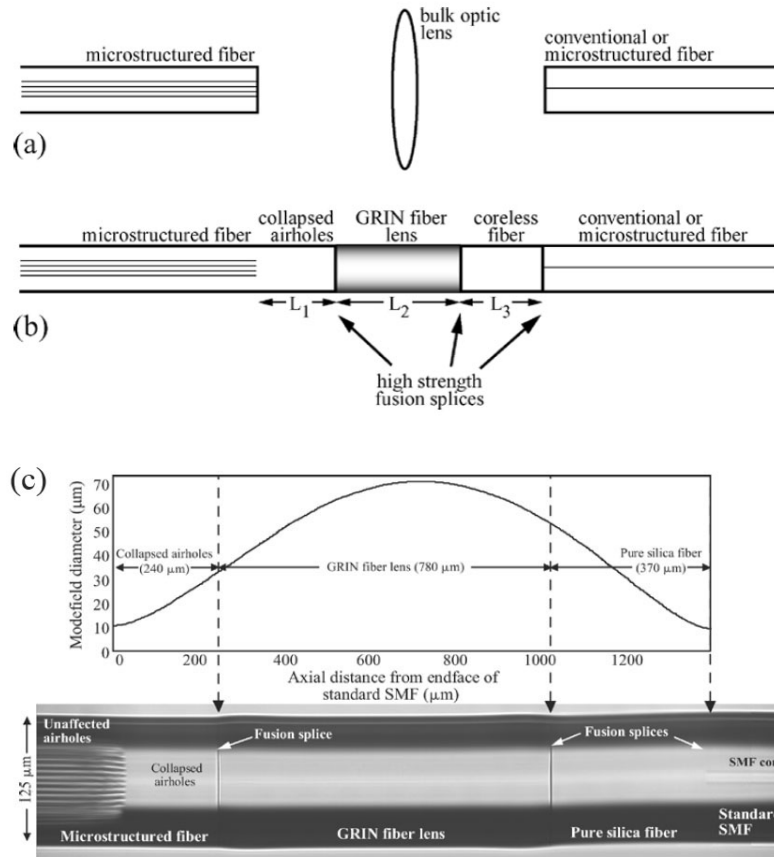


Figure 2.27 Illustration of how (a) conventional bulk optical coupling arrangement can be replaced by (b) GRIN fiber lens in conjunction with collapsed air holes in a PCF. (c) Evolution of MFD (top) and image of completed fusion splice assembly (bottom) between standard SMF and PCF [110].

#### 2.6.4 Tapered PCFs

Small-core PCFs have a number of nonlinear applications; however, low-loss splicing small-core PCFs with conventional SMFs is a challenging problem. To avoid direct splicing, tapering PCFs in the middle part provides a power tool to achieve a small-core and low transition loss. As shown in Fig. 2.28 [111], the un-tapered end of the air-clad-assist doped core PCF can be easily spliced to a conventional SMF with low loss, as mentioned in section 2.6.1. Tapering of the PCF is adiabatic so that the fundamental mode evolves into the fundamental mode of the central silica region, where it is confined by the ring of air holes. The loss represented by the tapering for the fundamental mode is about 0.1 dB.

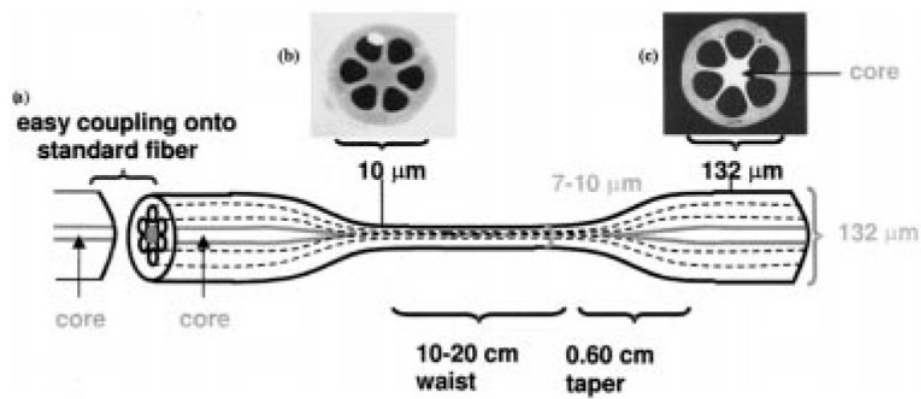


Figure 2.28 (a) Schematic of the tapered air-clad-assist doped-core PCF. (b) Cross section of tapered PCF with an outer diameter of  $10\ \mu\text{m}$ . (c) Cross section of the un-tapered PCF with an outer diameter of  $132\ \mu\text{m}$  [111].

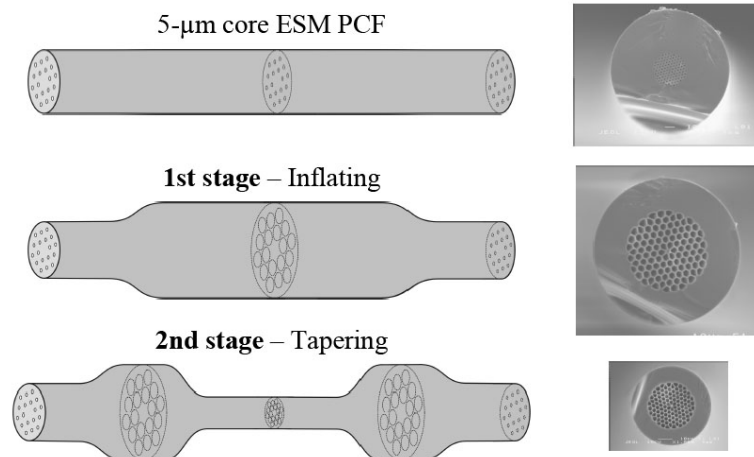


Figure 2.29 Endlessly single-mode PCF inflation and tapering process to produce a  $2\text{-}\mu\text{m}$ -core PCF with large air holes, which is connected at both ends to  $5\text{-}\mu\text{m}$ -core un-tapered PCF pigtailed with small air holes [112].

For endlessly single-mode (ESM) PCF, it can also be tapered to a small-core nonlinear PCF. As shown in Fig. 2.29 [112], first, the PCF is tapered “slow and hot”, using a hot flame for rapid hole inflation by high-pressure gas and stretching slowly to increase the processing time; secondly, the PCF is tapered “fast and cold”, using a cold flame to minimize the rate of hole collapse, and stretching as quickly as possible to minimize the processing time. The total losses of such a process are less than 0.4 dB. The end of the ESM PCF is easily spliced to a conventional SMF with

low loss. However, tapering is a time-consuming process, and the tapering part of the PCF needs to be specially protected because it is quite thin and fragile, which will limit its practical applications

### 2.6.5 Splice-free PCFs

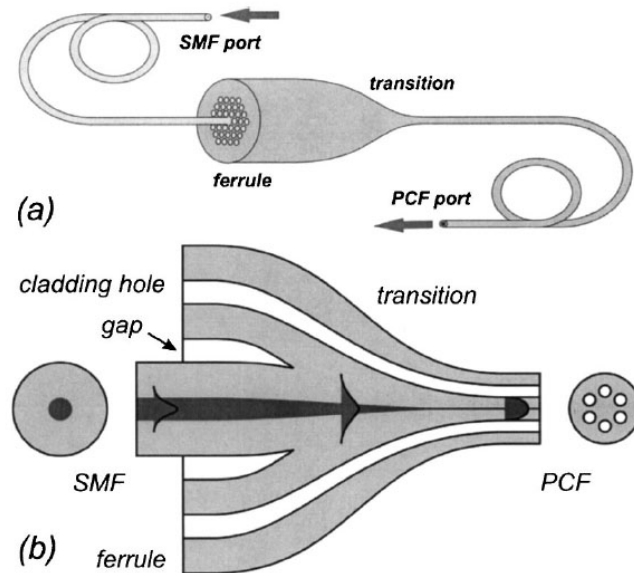


Figure 2.30 Schematic of a spliceless ferrule interface between a SMF and a PCF. (a) Construction of the interface by inserting a SMF into a void in the ferrule and then drawing it to a PCF. (b) Longitudinal section, showing how the mode spreads out from the tapered SMF core to become guided by the surrounding PCF core. The gap around the SMF in the void is collapsed by evacuation while drawing, forming a PCF core from the entire SMF and some ferrule material [113].

A splice-free method was reported to avoid splice loss [113]. The process is adapted from the fabrication of PCFs from stacked tubes and rods and is described schematically in Fig. 2.30. A PCF preform is constructed in the usual way but, instead of placing a solid rod in the stack of silica tubes, the central part is left empty. An intermediate preform (which is named a ferrule) is drawn from the stack so that the central void is more than 125  $\mu\text{m}$ , which is big enough to fit a fiber inside. A length of SMF is threaded into this void, replacing the rod omitted from the original stack; and one end of the filled ferrule is then drawn in the usual way into a PCF. As a result, the PCF is connected via a continuous transition to the SMF without

splicing. For example, the PCF drawn from the ferrule had a cobweb cladding structure supporting a core of 2.8  $\mu\text{m}$  diameter; the loss of the transition was less than 0.8 dB at 633 nm. However, this method is quite expensive because it is dependent on manufacturing PCF technology and the produced PCFs are limited within doped-core PCFs, which will hinder its wide development.

### 2.6.6 Splicing PCFs using fusion splicers

Fusion splicers are mostly reported for use in splicing SMFs and PCFs having similar MFDs [114-118, 99]. The splicing mechanism uses low fusion current and short fusion duration to minimize the collapse of the holes. For example, the splice loss between a solid-core PCF and a SMF was achieved to be about 0.45 dB, as shown in Fig. 2.31 (a). For hollow-core PCFs and SMFs having similar MFDs, low-loss splices were reported by using a filament fusion splicer [99] and an arc fusion splicer [118]. As shown in Fig. 2.31 (b), a splice loss of about 1.6 dB from a SMF (SMF-28) to a bandgap hollow-core PCF (HC-1550-02) was achieved. However, the potential of fusion splicers for all kinds of PCFs were not explored and the mechanism of low-loss fusion splicing needs to be studied further. We will investigate this type of splicing in detail in Chapter 3.

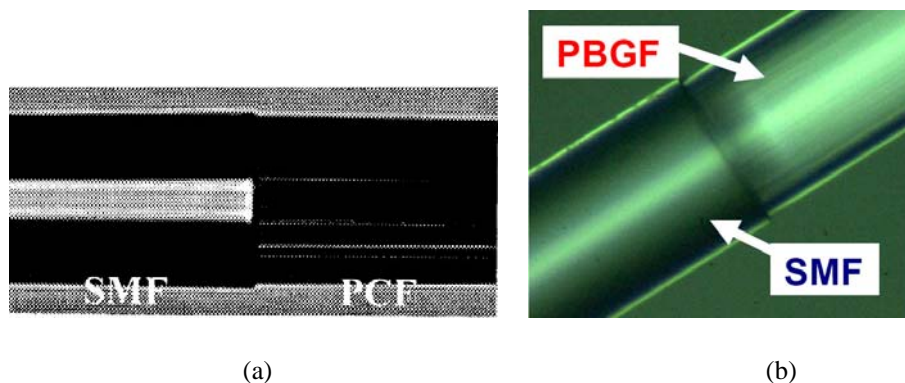


Figure 2.31 (a) SMF-PCF splice without hole collapse [116]; (b) Micrograph of the splice between a hollow-core bandgap PCF HC-1550-02 and a SMF [118].

## 2.7 Summary

We have reviewed the guiding mechanisms of PCFs, and the properties and applications of index-guiding PCFs and bandgap PCFs. Particularly, the modified and combined structure of PCFs are reviewed; the combination of PCFs with various materials is outlined. In the final section, PCF splice techniques are described, which is one of the main topics of this thesis and will be further investigated especially in chapters 3 and 4.

## References for Chapter 2

1. A. Bjarklev, J. Broeng, and A. S. Bjarklev, *Photonic Crystal Fibres*, Kluwer Academic Publishers, Boston, MA, 2003.
2. F. Zolla, G. Renversez, A. Nicolet, B. Kuhlmeiy, S. Guenneau, and D. Felbacq, *Foundations of Photonic Crystal Fibres*, Imperial College Press, London, 2005.
3. J. D. Joannopoulos, P. R. Meade, and J. N. Winn, *Photonic Crystals: Molding the Flow of Light*, Princeton University Press, Princeton, New Jersey, 1995.
4. J. M. Lourtioz, H. Benisty, V. Berger, J. M. Gérard, D. Maystre, and A. Tchebnokov, *Photonic Crystals: Towards Nanoscale Photonic Devices*, Springer, Berlin, 2005.
5. K. Busch, S. Lölkes, R. B. Wehrspohn, and H. Föll, *Photonic Crystals: Advances in Design, Fabrication, and Characterization*, Wiley-VCH, Weinheim, 2004.
6. J. C. Knight, "Photonic crystal fibres," *Nature*, vol. 424, pp. 847-851, (2003).
7. P. Russell, "Photonic crystal fibers," *Science*, vol. 299, pp. 358-362, (2003).
8. P. Russell, "Photonic-crystal fibers," *J. Lightwave Technol.*, vol. 24, pp.

- 4729-4749, (2006).
9. J. C. Knight, T. A. Birks, P. Russell, and D. M. Atkin, "All-silica single-mode optical fiber with photonic crystal cladding," *Opt. Lett.*, vol. 21, pp. 1547-1549, (1996).
  10. P. Yeh, A. Yariv, and E. Marom, "Theory of Bragg fiber," *J. Opt. Soc. Am.*, vol. 68, pp. 1196-1201, (1978).
  11. T. A. Birks, P. J. Roberts, P. Russell, D. M. Atkin, and T. J. Shepherd, "Full 2-D photonic bandgaps in silica/air structures," *Electron. Lett.*, vol. 31, pp. 1941-1942, (1995).
  12. J. C. Knight, J. Broeng, T. A. Birks, and P. Russell, "Photonic band gap guidance in optical fibers," *Science*, vol. 282, pp. 1476-1478, (1998).
  13. R. F. Cregan, B. J. Mangan, J. C. Knight, T. A. Birks, P. Russell, P. J. Roberts, and D. C. Allan, "Single-mode photonic band gap guidance of light in air," *Science*, vol. 285, pp. 1537-1539, (1999).
  14. A. Cerqueira, F. Luan, C. M. B. Cordeiro, A. K. George, and J. C. Knight, "Hybrid photonic crystal fiber," *Opt. Express*, vol. 14, pp. 926-931, (2006).
  15. T. A. Birks, J. C. Knight, and P. Russell, "Endlessly single-mode photonic crystal fiber," *Opt. Lett.*, vol. 22, pp. 961-963, (1997).
  16. A. Ferrando, E. Silvestre, J. J. Miret, P. Andrés, and M. V. Andrés, "Full-vector analysis of a realistic photonic crystal fiber," *Opt. Lett.*, vol. 24, pp. 276-278, (1999).
  17. A. Ferrando, E. Silvestre, J. J. Miret, P. Andrés, and M. V. Andrés, "Vector description of higher-order modes in photonic crystal fibers," *J. Opt. Soc. Am. A*, vol. 17, pp. 1333-1340, (2000).
  18. M. Koshiba, "Full-vector analysis of photonic crystal fibers using the finite

- element method,” *IEICE Trans. Electron.*, vol. E85-C, pp. 881-888, (2002).
19. N. A. Mortensen, J. R. Folkenberg, M. D. Nielsen, and K. P. Hansen, “Modal cutoff and the V parameter in photonic crystal fibers,” *Opt. Lett.*, vol. 28, pp. 1879-1881, (2003).
20. J. C. Knight, T. A. Birks, P. Russell, and J. P. de Sandro, “Properties of photonic crystal fiber and the effective index model,” *J. Opt. Soc. Am. A*, vol. 15, pp. 748-752, (1998).
21. M. Yan and P. Shum, “Guidance varieties in photonic crystal fibers,” *J. Opt. Soc. Am. B*, vol. 23, pp. 1684-1691, (2006).
22. Y. Fink, D. J. Ripin, S. Fan, C. Chen, J. D. Joannopoulos, and E. L. Thomas, “Guiding Optical Light in Air Using an All-Dielectric Structure,” *J. Lightwave Technol.*, vol. 17, pp. 2039-2041, (1999).
23. B. Temelkuran, S. D. Hart, G. Benoit, J. D. Joannopoulos, and Y. Fink, “Wavelength-scalable hollow optical fibres with large photonic bandgaps for CO<sub>2</sub> laser transmission,” *Nature*, vol. 420, pp. 650–653, (2002).
24. E. Yablonovitch, “Photonic band-gap structures,” *J. Opt. Soc. Am. B*, vol. 10, pp. 283-295, (1993).
25. Y. Fink, J. N. Winn, S. Fan, C. Chen, J. Michel, J. D. Joannopoulos, and E. L. Thomas, “A dielectric omnidirectional reflector,” *Science*, vol. 282, pp. 1679-1682, (1998).
26. M. Ibanescu, Y. Fink, S. Fan, E. L. Thomas, and J. D. Joannopoulos, “An all-dielectric coaxial waveguide,” *Science*, vol. 289, pp. 415-419, (2000).
27. S. Johnson, M. Ibanescu, M. Skorobogatiy, O. Weisberg, T. Engeness, M. Soljacic, S. Jacobs, J. Joannopoulos, and Y. Fink, “Low-loss asymptotically single-mode propagation in large-core OmniGuide fibers,” *Opt. Express*, vol. 9,

- pp. 748-779, (2001).
28. P. R. Villeneuve, and M. Piché, “Photonic band gaps in two-dimensional square and hexagonal lattices,” *Phys. Rev. B*, vol. 46, pp. 4969-4972, (1992).
  29. V. V. R. Kumar, A. George, W. Reeves, J. Knight, P. Russell, F. Omenetto, and A. Taylor, “Extruded soft glass photonic crystal fiber for ultrabroad supercontinuum generation,” *Opt. Express*, vol. 10, pp. 1520-1525, (2002).
  30. P. Petropoulos, H. E. Heidepriem, V. Finazzi, R. Moore, K. Frampton, D. Richardson, and T. Monro, “Highly nonlinear and anomalously dispersive lead silicate glass holey fibers,” *Opt. Express*, vol. 11, pp. 3568-3573, (2003).
  31. X. Feng, A. K. Mairaj, D. W. Hewak, and T. M. Monro, “Nonsilica Glasses for Holey Fibers,” *J. Lightwave Technol.*, vol. 23, pp. 2046-2054, (2005).
  32. M. Eijkelenborg, M. Large, A. Argyros, J. Zagari, S. Manos, N. Issa, I. Bassett, S. Fleming, R. McPhedran, C. M. de Sterke, and N. A. Nicorovici, “Microstructured polymer optical fibre,” *Opt. Express*, vol. 9, pp. 319-327, (2001).
  33. E. Pone, C. Dubois, N. Gu, Y. Gao, A. Dupuis, F. Boismenu, S. Lacroix, and M. Skorobogatiy, “Drawing of the hollow all-polymer Bragg fibers,” *Opt. Express*, vol. 14, pp. 5838-5852, (2006).
  34. M. Mignanelli, K. Wani, J. Ballato, S. Foulger, and P. Brown, “Polymer microstructured fibers by one-step extrusion,” *Opt. Express*, vol. 15, pp. 6183-6189, (2007).
  35. S. Guo and S. Albin, “Simple plane wave implementation for photonic crystal calculations,” *Opt. Express*, vol. 11, pp. 167-175, (2003).
  36. S. Johnson and J. Joannopoulos, “Block-iterative frequency-domain methods for Maxwell's equations in a planewave basis,” *Opt. Express*, vol. 8, pp. 173-190,

- (2001).
37. A. Abeeluck, N. Litchinitser, C. Headley, and B. Eggleton, "Analysis of spectral characteristics of photonic bandgap waveguides," *Opt. Express*, vol. 10, pp. 1320-1333, (2002).
  38. N. M. Litchinitser, A. K. Abeeluck, C. Headley, B. J. Eggleton, "Antiresonant reflecting photonic crystal optical waveguides," *Opt. Lett.*, vol. 27, pp. 1592-1594, (2002).
  39. T. P. White, R. C. McPhedran, C. M. de Sterke, N. M. Litchinitser, B. J. Eggleton, "Resonance and scattering in microstructured optical fibers," *Opt. Lett.* vol. 27, pp. 1977-1979, (2002).
  40. N. M. Litchinitser, S. C. Dunn, B. Usner, B. J. Eggleton, T. P. White, R. C. McPhedran, and C. M. de Sterke, "Resonances in microstructured optical waveguides," *Opt. Express*, vol. 11, pp. 1243-1251, (2003).
  41. N. Litchinitser, S. Dunn, P. Steinvurzel, B. Eggleton, T. White, R. McPhedran, and C. de Sterke, "Application of an ARROW model for designing tunable photonic devices," *Opt. Express*, vol. 12, pp. 1540-1550, (2004).
  42. P. Steinvurzel, B. Kuhlmeiy, T. White, M. Steel, C. de Sterke, and B. J. Eggleton, "Long wavelength anti-resonant guidance in high index inclusion microstructured fibers," *Opt. Express*, vol. 12, pp. 5424-5433, (2004).
  43. A. Argyros, T. Birks, S. Leon-Saval, C. M. B. Cordeiro, and P. Russell, "Guidance properties of low-contrast photonic bandgap fibres," *Opt. Express*, vol. 13, pp. 2503-2511, (2005).
  44. P. Steinvurzel, C. Martijn de Sterke, M. J. Steel, B. T. Kuhlmeiy, and B. J. Eggleton, "Single scatterer Fano resonances in solid core photonic band gap fibers," *Opt. Express*, vol. 14, pp. 8797-8811, (2006).

45. S. G. Johnson, S. Fan, P. R. Villeneuve, J. D. Joannopoulos, and L.A. Kolodziejski, "Guided modes in photonic-crystal slabs," *Phys. Rev. B*, vol. 60, pp. 5751-5780, (1999).
46. K. Tajima, K. Kurokawa, K. Nakajima, and I. Sankawa, "Photonic crystal fiber," *NTT Technical Review*, vol. 3, pp. 57-61, (2005).
47. K. Tajima, and J. Zhou, "Ultra low loss and long length photonic crystal fiber," *IEICE Trans. Electron.*, vol. E88-C, pp. 870-875, (2005).
48. J. C. Knight, T. A. Birks, R. F. Cregan, P. Russell and J. P. de Sandro, "Large mode area photonic crystal fiber," *Electron. Lett.*, vol. 34, pp. 1347-1348, (1998).
49. J. C. Baggett, T. M. Monro, K. Furusawa, and D. J. Richardson, "Comparative study of large mode holey and conventional fibers," *Opt. Lett.*, vol. 26, pp. 1045-1047, (2001).
50. W. Reeves, J. Knight, P. Russell, and P. Roberts, "Demonstration of ultra-flattened dispersion in photonic crystal fibers," *Opt. Express*, vol. 10, pp. 609-613, (2002).
51. W. J. Wadsworth, R. M. Percival, G. Bouwmans, J. C. Knight, T. A. Birks, T. D. Hedley, and P. Russell, "Very High Numerical Aperture Fibers," *Photonics Technol. Lett.*, vol. 16, pp. 843-845, (2004).
52. K. Furusawa, A. Malinowski, J. Price, T. Monro, J. Sahu, J. Nilsson, and D. Richardson, "Cladding pumped Ytterbium-doped fiber laser with holey inner and outer cladding," *Opt. Express*, vol. 9, pp. 714-720, (2001).
53. W. Wadsworth, R. Percival, G. Bouwmans, J. Knight, and P. Russell, "High power air-clad photonic crystal fibre laser," *Opt. Express*, vol. 11, pp. 48-53, (2003).

54. J. Limpert, T. Schreiber, S. Nolte, H. Zellmer, T. Tunnermann, R. Iliew, F. Lederer, J. Broeng, G. Vienne, A. Petersson, and C. Jakobsen, "High-power air-clad large-mode-area photonic crystal fiber laser," *Opt. Express*, vol. 11, pp. 818-823, (2003).
55. J.C. Knight, J. Arriaga, T. A. Birks, A. Ortigosa-Blanch, W. J. Wadsworth, and P. Russell, "Anomalous dispersion in photonic crystal fiber," *Photon. Technol. Lett.*, vol. 12, pp. 807-809, (2000).
56. J. K. Ranka, R. S. Windeler, and A. J. Stentz, "Visible continuum generation in air-silica microstructure optical fibers with anomalous dispersion at 800 nm," *Opt. Lett.*, vol. 25, pp. 25-27, (2000).
57. I. Hartl, X. D. Li, C. Chudoba, R. K. Ghanta, T. H. Ko, J. G. Fujimoto, J. K. Ranka, and R. S. Windeler, "Ultrahigh-resolution optical coherence tomography using continuum generation in an air-silica microstructure optical fiber," *Opt. Lett.*, vol. 26, pp. 608-610, (2001).
58. A. Zhang and M. S. Demokan, "Broadband wavelength converter based on four-wave mixing in a highly nonlinear photonic crystal fiber," *Opt. Lett.*, vol. 30, pp. 2375-2377, (2005).
59. T. Udem, R. Holzwarth, and T. W. Hänsch, "Optical frequency metrology," *Nature*, vol. 416, pp. 233-237, (2002).
60. B. J. Eggleton, C. Kerbage, P. Westbrook, R. Windeler, and A. Hale, "Microstructured optical fiber devices," *Opt. Express*, vol. 9, pp. 698-713, (2001).
61. C. Kerbage, A. Hale, A. Yablon, R. S. Windeler, and B. J. Eggleton, "Integrated all-fiber variable attenuator based on hybrid microstructure fiber," *Appl. Phys. Lett.*, vol. 79, pp. 3191-3193, (2001).

62. P. Mach, M. Dolinski, K. W. Baldwin, J. A. Rogers, C. Kerbage, R. S. Windeler, and B. J. Eggleton, "Tunable microfluidic optical fiber," *Appl. Phys. Lett.*, vol. 80, pp. 4294-4296, (2002).
63. C. Kerbage, R. S. Windeler, B. J. Eggleton, P. Mach, M. Dolinski, and J. A. Rogers, "Tunable devices based on dynamic positioning of micro-fluids in micro-structured optical fiber," *Opt. Commun.*, vol. 204, pp. 179-184, (2002).
64. C. Kerbage, P. Steinvurzel, P. Reyes, P. S. Westbrook, R. S. Windeler, A. Hale, and B. J. Eggleton, "Highly tunable birefringent microstructured optical fiber," *Opt. Lett.*, vol. 27, pp. 842-844, (2002).
65. Y. Bing, K. Ohsono, Y. Kurosawa, T. Kumagai, M. Tachikura, "Low-loss holey fiber," *Hitachi Cable Review*, vol. 24, pp. 1-5, (2005).
66. A. Ortigosa-Blanch, J. C. Knight, W. J. Wadsworth, J. Arriaga, B. J. Mangan, T. A. Birks, and P. S. J. Russell, "Highly birefringent photonic crystal fibers," *Opt. Lett.*, vol. 25, pp. 1325-1327, (2000).
67. T. P. Hansen, J. Broeng, E. B. Libori, E. Knudsen, A. Bjarklev, J. R. Jensen, and H. Simonsen, "Highly birefringent index-guiding photonic crystal fibers," *Photon. Tech. Lett.*, vol. 13, pp. 588-590, (2001).
68. K. Suzuki, H. Kubota, S. Kawanishi, M. Tanaka, and M. Fujita, "Optical properties of a low-loss polarization-maintaining photonic crystal fiber," *Opt. Express*, vol. 9, pp. 676-680, (2001).
69. M. J. Steel and R. M. Osgood, "Elliptical-hole photonic crystal fibers," *Opt. Lett.*, vol. 26, pp. 229-231, (2001).
70. N. A. Issa, M. A. V. Eijkelenborg, M. Fellew, F. Cox, G. Henry, and M. C. J. Large, "Fabrication and study of microstructured optical fibers with elliptical holes," *Opt. Lett.*, vol. 29, pp. 1336-1338, (2004).

71. H. Kubota, S. Kawanishi, S. Koyanagi, M. Tanaka, and S. Yamaguchi, "Absolutely Single Polarization Photonic Crystal Fiber," *Photon. Technol. Lett.*, vol. 16, pp. 182-184, (2004).
72. J. Ju, W. Jin, and M. S. Demokan, "Design of Single-Polarization Single-Mode Photonic Crystal Fiber at 1.30 and 1.55  $\mu\text{m}$ ," *J. Lightwave Technol.*, vol. 24, pp. 825-830, (2006).
73. A. Michie, J. Canning, K. Lyttikäinen, M. Åslund, and J. Digweed, "Temperature independent highly birefringent photonic crystal fibre," *Opt. Express*, vol. 12, pp. 5160-5165, (2004).
74. F. Brechet, P. Roy, J. Marcou, and D. Pagnoux, "Singlemode propagation into depressed-core-index photonic-bandgap fibre designed for zero-dispersion propagation at short wavelengths," *Electron. Lett.*, vol. 36, pp. 514-515, (2000).
75. S. Février, P. Viale, F. Gerome, P. Leproux, P. Roy, J. M. Blondy, B. Dussardier, G. Monnom, "Very large effective area singlemode photonic bandgap fiber," *Electron. Lett.*, vol. 39, pp. 1240-1242, (2003).
76. S. Février, R. Jamier, J. -M. Blondy, S. L. Semjonov, M. E. Likhachev, M. M. Bubnov, E. M. Dianov, V. F. Khopin, M. Y. Salganskii, and A. N. Guryanov, "Low-loss singlemode large mode area all-silica photonic bandgap fiber," *Opt. Express*, vol. 14, pp. 562-569, (2006).
77. T. Katagiri, Y. Matsuura, and M. Miyagi, "All-Solid Single-Mode Bragg Fibers for Compact Fiber Devices," *J. Lightwave Technol.*, vol. 24, pp. 4314-4318, (2006).
78. G. Vienne, Y. Xu, C. Jakobsen, H. J. Deyerl, J. Jensen, T. Sorensen, T. Hansen, Y. Huang, M. Terrel, R. Lee, N. Mortensen, J. Broeng, H. Simonsen, A. Bjarklev, and A. Yariv, "Ultra-large bandwidth hollow-core guiding in all-silica Bragg

- fibers with nano-supports,” *Opt. Express*, vol. 12, pp. 3500-3508, (2004).
79. F. Luan, A. K. George, T. D. Hedley, G. J. Pearce, D. M. Bird, J. C. Knight, and P. Russell, “All-solid photonic bandgap fiber,” *Opt. Lett.*, vol. 29, pp. 2369-2371, (2004).
80. G. Ren, P. Shum, L. Zhang, X. Yu, W. Tong, and J. Luo, “Low-loss all-solid photonic bandgap fiber,” *Opt. Lett.*, vol. 32, pp. 1023-1025, (2007).
81. A. Argyros, T. Birks, S. Leon-Saval, C. M. Cordeiro, F. Luan, and P. Russell, “Photonic bandgap with an index step of one percent,” *Opt. Express*, vol. 13, pp. 309-314, (2005).
82. T. Larsen, A. Bjarklev, D. Hermann, and J. Broeng, “Optical devices based on liquid crystal photonic bandgap fibres,” *Opt. Express*, vol. 11, pp. 2589-2596, (2003).
83. P. Roberts, F. Couny, H. Sabert, B. Mangan, D. Williams, L. Farr, M. Mason, A. Tomlinson, T. Birks, J. Knight, and P. Russell, “Ultimate low loss of hollow-core photonic crystal fibres,” *Opt. Express*, vol. 13, pp. 236-244, (2005).
84. H. K. Kim, M. J. F. Digonnet, and G. S. Kino, “Air-Core Photonic-Bandgap Fiber-Optic Gyroscope,” *J. Lightwave Technol.*, vol. 24, pp. 3169-3174, (2006).
85. S. Blin, H. K. Kim, M. J. F. Digonnet, and G. S. Kino, “Reduced Thermal Sensitivity of a Fiber-Optic Gyroscope Using an Air-Core Photonic-Bandgap Fiber,” *J. Lightwave Technol.*, vol. 25, pp. 861-865, (2007).
86. D. G. Ouzounov, F. R. Ahmad, A. L. Gaeta, D. Muller, N. Venkataraman, M. Gallagher, C. M. Smith, and K. W. Koch, “Generation of megawatt solitons in hollow-core photonic band-gap fibers,” *Science*, vol.301, pp. 1702-1704, (2003).
87. F. Benabid, J. C. Knight, G. Antonopoulos, P. Russell, “Stimulated Raman scattering in hydrogen-filled hollow-core photonic crystal fiber,” *Science*, vol.

- 298, pp. 399–402, (2002).
88. F. Benabid, G. Bouwmans, J. C. Knight, P. Russell, and F. Couny, “Ultra-high efficiency laser wavelength conversion in a gas-filled hollow core photonic crystal fiber by pure stimulated rotational Raman scattering in molecular hydrogen,” *Phys. Rev. Lett.*, vol. 93, id. 123903, (2004).
89. F. Benabid, J. Knight, and P. Russell, “Particle levitation and guidance in hollow-core photonic crystal fiber,” *Opt. Express*, vol. 10, pp. 1195-1203, (2002).
90. T. Takekoshi, and R. J. Knize, “Optical Guiding of Atoms through a Hollow-Core Photonic Band-Gap Fiber,” *Phys. Rev. Lett.*, vol. 98, id. 210404, (2004).
91. Y. L. Hoo, W. Jin, H. L. Ho, J. Ju, and D. N. Wang, “Gas diffusion measurement using hollow-core photonic bandgap fiber,” *Sens. Actuators B*, vol. 105, pp. 183-186, (2005).
92. J. M. Fini, “Microstructure fibres for optical sensing in gases and liquids,” *Meas. Sci. Technol.*, vol. 15, pp. 1120-1128, (2004).
93. N. A. Mortensen, M. D. Nielsen, J. R. Folkenberg, A. Petersson, and H. R. Simonsen, “Improved large-mode-area endlessly single-mode photonic crystal fibers,” *Opt. Lett.*, vol. 28, pp. 393-395, (2003).
94. P. Roberts, D. Williams, B. Mangan, H. Sabert, F. Couny, W. Wadsworth, T. Birks, J. Knight, and P. Russell, “Realizing low loss air core photonic crystal fibers by exploiting an antiresonant core surround,” *Opt. Express*, vol. 13, 8277-8285, (2005).
95. A. Bétourné, V. Pureur, G. Bouwmans, Y. Quiquempois, L. Bigot, M. Perrin, and M. Douay, “Solid photonic bandgap fiber assisted by an extra air-clad structure

- for low-loss operation around 1.5  $\mu\text{m}$ ,” *Opt. Express*, vol. 15, pp. 316-324, (2007).
96. D. Chen, and L. F. Shen, “Ultrahigh birefringent photonic crystal fiber with ultralow confinement loss,” *Photon. Technol. Lett.*, vol. 19, pp. 185-187, (2007).
97. M. Bayindir, O. Shapira, D. Saygin-Hinczewski, J. Viens, A. F. Abouraddy, J. D. Joannopoulos, and Y. Fink, “Integrated fibres for self-monitored optical transport,” *Nat. Mater.*, vol. 4, pp. 820-825, (2005).
98. A. F. Abouraddy, M. Bayindir, G. Benoit, S. D. Hart, K. Kuriki, N. Orf, O. Shapira, F. Sorin, B. Temelkuran, and Y. Fink, “Towards multimaterial multifunctional fibres that see, hear, sense and communicate,” *Nat. Mater.*, vol. 6, pp. 336-347, (2007).
99. F. Benabid, F. Couny, J. C. Knight, T. A. Birks and P. Russell, “Compact, stable and efficient all-fiber gas cells using hollow-core photonic crystal fibers,” *Nature*, vol. 434, pp. 488-491, (2005).
100. Y. L. Hoo, W. Jin, H. L. Ho, D. N. Wang, and R. S. Windeler, “Evanescent-wave gas sensing using microstructure fiber,” *Opt. Eng.*, vol. 41, pp. 8-9, (2002).
101. J. B. Jensen, L. H. Pedersen, P. E. Hoiby, L. B. Nielsen, T. P. Hansen, J. R. Folkenberg, J. Riishede, D. Noordegraaf, K. Nielsen, A. Carlsen, and A. Bjarklev, “Photonic crystal fiber based evanescent-wave sensor for detection of biomolecules in aqueous solutions,” *Opt. Lett.*, vol. 29, pp. 1974-1976, (2004).
102. Y. Huang, Y. Xu, and A. Yariv, “Fabrication of functional microstructured optical fibers through a selective-filling technique,” *Appl. Phys. Lett.*, vol. 85, pp. 5182-5184, (2004).
103. S. Yiou, P. Delaye, A. Rouvie, J. Chinaud, R. Frey, G. Roosen, P. Viale, S.

- Février, P. Roy, J. L. Auguste, and J. M. Blondy, "Stimulated Raman scattering in an ethanol core microstructured optical fiber," *Opt. Express*, vol. 13, pp. 4786-4791, (2005).
104. R. Zhang, J. Teipel, and H. Giessen, "Theoretical design of a liquid-core photonic crystal fiber for supercontinuum generation," *Opt. Express*, vol. 14, pp. 6800-6812, (2006).
105. F. Du, Y. Lu, and S. Wu, "Electrically tunable liquid-crystal photonic crystal fiber," *Appl. Phys. Lett.*, vol. 85, pp. 2181-2183, (2004).
106. M. W. Haakestad, T. T. Alkeskjold, M. D. Nielsen, L. Scolari, J. Riishede, H. E. Engan, and A. Bjarklev, "Electrically tunable photonic bandgap guidance in a liquid-crystal-filled photonic crystal fiber," *Photon. Technol. Lett.*, vol. 17, pp. 819-821, (2005).
107. T. T. Alkeskjold, J. Lagsgaard, A. Bjarklev, D.S. Hermann, Anawati, J. Broeng, J. Li, and S. Wu, "All-optical modulation in dye-doped nematic liquid crystal photonic bandgap fibers" *Opt. Express*, vol. 12, pp. 5857-5871, (2004).
108. J. H. Chong, and M. K. Rao, "Development of a system for laser splicing photonic crystal fiber," *Opt. Express*, vol. 11, pp. 1365-1370, (2003).
109. J. H. Chong, M. K. Rao, Y. Zhu, and P. Shum, "An effective splicing method on photonic crystal fiber using CO2 laser," *Photon. Technol. Lett.*, vol. 15, pp. 942-944, (2003).
110. A. D. Yablon, R. T. Bise, "Low-loss high-strength microstructured fiber fusion splices using grin fiber lenses," *Photon. Technol. Lett.*, vol. 17, pp. 118-120, (2005).
111. J. K. Chandalia, B. J. Eggleton, R. S. Windeler, S. G. Kosinski, X. Liu and C. Xu, "Adiabatic coupling in tapered air-silica microstructured optical fiber,"

- Photon. Technol. Lett.*, vol. 13, pp. 52-54, (2001).
112. W. Wadsworth, A. Witkowska, S. Leon-Saval, and T. Birks, "Hole inflation and tapering of stock photonic crystal fibres," *Opt. Express*, vol. 13, pp. 6541-6549, (2005).
113. S. G. Leon-Saval, T. A. Birks, N. Y. Joly, A. K. George, W. J. Wadsworth, G. Kakarantzas, and P. Russell, "Splice-free interfacing of photonic crystal fibers," *Opt. Lett.*, vol. 30, pp. 1629-1631, (2005).
114. P. J. Bennett, T. M. Monro, and D. J. Richardson, "Toward practical holey fiber technology: fabrication, splicing, modeling, and characterization," *Opt. Lett.*, vol. 24, pp. 1203-1205, (1999).
115. B. Bourliaguet, C. Paré, F. Émond, A. Croteau, A. Proulx, R. Vallée, "Microstructured fiber splicing," *Opt. Express*, vol. 11, pp. 3412-3417, (2003).
116. B. H. Park, J. Kim, U.C. Paek, B.H. Lee, "The optimum fusion splicing conditions for a large mode area photonic crystal fiber," *IEICE Trans. Electron.*, vol. E88-C, pp. 883-888, (2005).
117. T. P. Hansen, J. Broeng, C. Jakobsen, G. Vienne, H. R. Simonsen, M. D. Nielsen, P. M. W. Skovgaard, J. R. Folkenberg, and A. Bjarklev, "Air-guiding photonic bandgap fibers: spectral properties, macrobending loss, and practical handling," *J. Lightwave Technol.*, vol. 22, pp. 11-15, (2004).
118. R. Thapa, K. Knabe, K. L. Corwin, and B. R. Washburn, "Arc fusion splicing of hollow-core photonic bandgap fibers for gas-filled fiber cells," *Opt. Express*, vol. 14, pp. 9576-9583, (2006).

## Chapter 3

### Fusion splice PCFs

#### 3.1 Introduction

To realize the full potential of PCFs, it is necessary to couple light efficiently from conventional single mode fibers (SMFs) to PCFs. However, because PCFs have micro-hole structures which are totally different from conventional fibers, splicing different PCFs to conventional fibers is a significant challenge.

Since Bennett et al. first reported splicing SMFs and PCFs experimentally in 1999 [1], many splice methods have been proposed for the PCFs. One solution is to design special solid-core PCFs which have the same mode field diameters (MFDs) as SMFs [2, 3] or to design PCFs with doped core which will guide light even when the air holes have completely collapsed during splicing [4-6]; however, those methods will limit the flexibility in PCF designs. For solid-core PCFs and SMFs having similar MFDs, low-loss splices were achieved by using fusion splicers [1, 7, 8] or CO<sub>2</sub> lasers [9, 10]; another type of low-loss high-strength splice between a solid-core PCF and a SMF having similar MFDs was achieved by using a GRIN fiber lens [11]. For hollow-core PCFs and SMFs having similar MFDs, low-loss splices were reported by using fusion splicers [12-14]. However, these splice

methods are limited in PCFs having similar MFDs compared with those of SMFs. For small-core PCFs and SMFs, several indirect splicing methods have been proposed, such as tapered intermediate PCFs [15, 16], integrating a SMF with a PCF during the manufacturing stage of the PCF [17]. The drawbacks of these methods are time-consuming and expensive, which will limit their wide development.

Because the splicing problem between PCFs and SMFs is still a major limitation which hinders the incorporation of PCFs into conventional fiber systems, it is significant important to find a simple and low-cost way to splice different PCFs with conventional SMFs. Since fusion splicing is the most mature technology in splicing fibers and that commercial fusion splicers are widely used, it will be a simple and practical solution to splice SMFs and PCFs. However, fusion splicers are mostly reported for use in splicing SMFs and PCFs having similar MFDs, and fusion splicers from different companies or different types have different parameter sets, therefore the value of the optimized parameters will be limited for splicing PCFs with different structures.

The micro-hole collapse phenomenon of fusion splicing and its effect on splice loss is a new issue which is important to an understanding of the splice loss. In order to explore novel splice methods between different types of PCFs and SMFs, a systematic investigation needs to be conducted which has not been done so far.

In this chapter, we investigate the nature of micro-hole collapse when splicing and its effect on splicing loss. Different kinds of PCFs have different micro-hole structures, and the properties of heat-induced collapse when splicing are quite different. One solution which is suitable for one kind of PCF will fail when applying to other kinds of PCF. A detailed study about the effect of micro-hole collapse on

the splice loss for different kinds of PCFs is conducted, which explains the physical mechanism of the splice loss clearly and visually, and helps us to find the best way to splice different PCFs. Also, the optimized parameters corresponding to the status of micro-hole collapse are valuable for users in finding the optimized values when using other splicers. In this chapter, we provide the guidelines and demonstrate the simple techniques for low-loss splicing five different kinds of PCFs with SMFs using a conventional fusion splicer.

### **3.2 Challenges in splicing PCFs**

The splice loss is generally due to two reasons: one is the mode field mismatch between PCFs and SMFs; the other is that the air holes in PCFs may completely collapse in the vicinity of the splice joint during the splicing process, which significantly increases the coupling loss by destroying the light guiding structure of PCF near the joint interface.

In this chapter, we investigated the splicing of five different PCFs with conventional SMFs. The PCFs are LMA-10, HC-1550-02, LMA-5, NL-3.3-880 and PM-1550-01 from Crystal-Fiber A/S, as shown in Fig. 3.1. Fig. 3.1(a) shows Scanning Electron Microscope (SEM) micrographs of these PCF cross-sections; Fig. 3.1(b) shows side views of these PCFs through an optical microscope. We can observe the micro-hole channels from the side views, which will be of benefit in determining the degree of collapse of the air holes after fusion splicing in our experiments. The conventional SMF used in our experiments is SMF-28 from Corning. The fiber parameters are listed in Table 3.1. An Ericsson FSU-975 fusion splicer was used in the experiments.

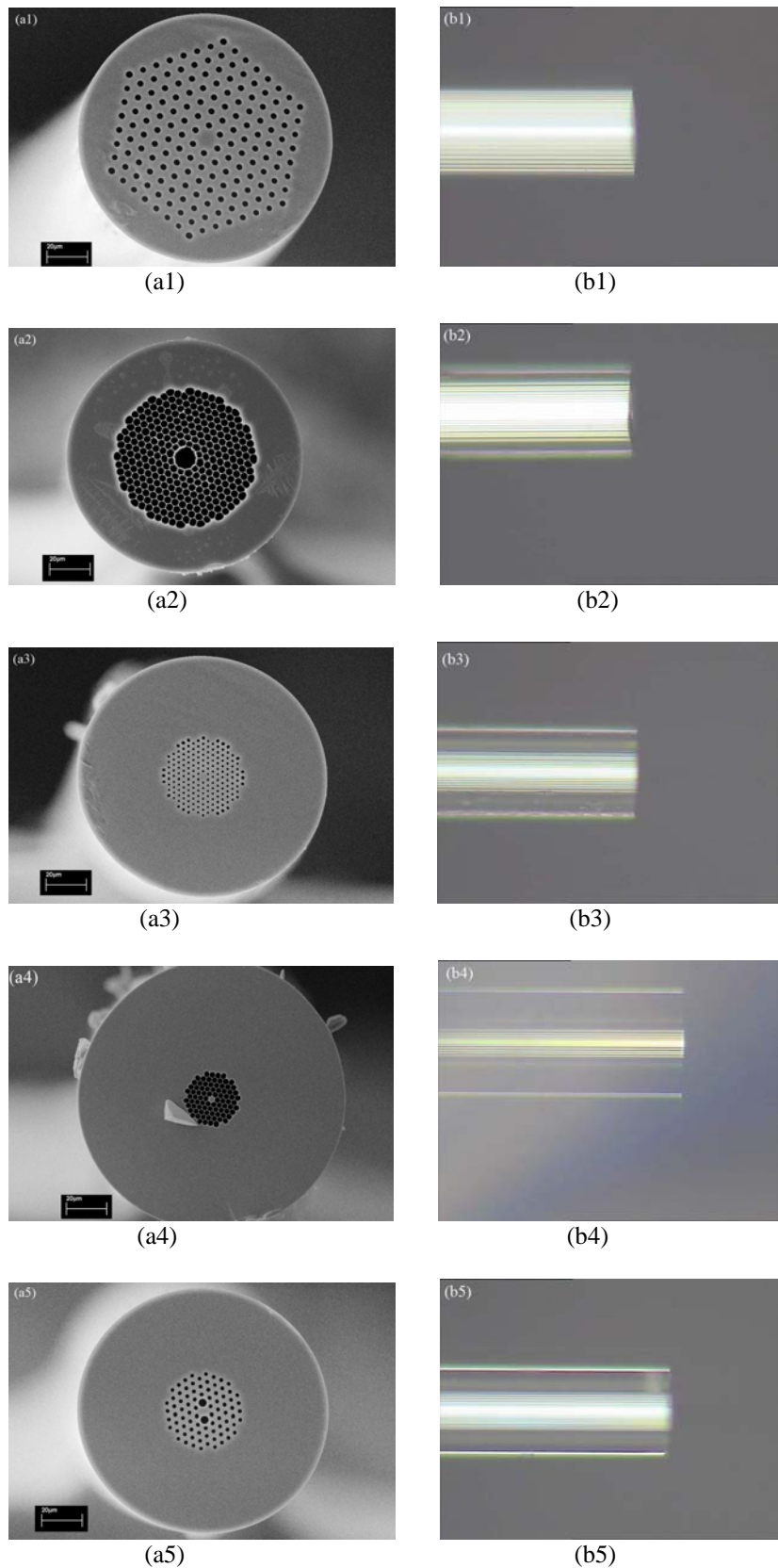


Figure 3.1 SEM photographs of the cross section of the different PCFs used for the experiments: (a1) LMA-10, (a2) HC-1550-02, (a3) LMA-5, (a4) NL-3.3-880, (a5) PM-1550-01; Optical microscope image of the side view of corresponding PCFs used for the experiments: (b1) LMA-10, (b2) HC-1550-02, (b3) LMA-5, (b4) NL-3.3-880, (b5) PM-1550-01.

Table 3.1 Fiber parameters @ 1550 nm

Fiber	Core diameter (μm)	Relative hole size d/Λ	Pitch Λ (μm)	MFD (μm)	Numerical aperture NA
LMA-10	10.71	0.46	7.14	8.5	0.14
HC-1550-02	10.9	>90%*	3.8	7.5	0.12
LMA-5	4.5	0.44	2.9	4.1	0.23
NL-3.3-880	3.4	>89%*	3.0	2.2	0.41
PM-1550-01	—	Large hole 0.97 Small hole 0.51	4.17	Long axis 3.6 Short axis 3.1	—
SMF-28	8.3	—	—	10.4	0.14

\* Air filling fraction

### 3.2.1 Collapse of air holes

When fusion splicing conventional fibers, the fiber tips are heated above the softening point and then are pressed together to form a joint. However, when the temperature of heated PCFs exceeds the softening point, the surface tension will overcome the viscosity and cause the PCF's cylindrical air holes to collapse. What's more, the softening point of the PCFs is in general lower than that of SMFs because PCFs have smaller average solid silica diameter (due to air-silica structures) than that of conventional SMFs [9, 10], assuming that the heat absorption coefficient is almost the same for PCFs and SMFs. The rate of air hole collapse can be given by [11, 18]

$$V_{collapse} = \frac{\gamma}{2\eta} \quad (1)$$

where  $\gamma$  is the surface tension and  $\eta$  is the viscosity. Surface tension of silica is not very sensitive to temperature over the range encountered in splicing, but the viscosity of silica decreases sharply with increasing temperature, so the rate of the

air holes collapse increases with temperature. If we use the program which is set for conventional SMFs, the total arc discharge energy is too high for a PCF so that the applied heat will collapse the air holes of the PCF completely at the joint part. This causes the splice loss to become very large because the waveguide structure of the PCF near the splice joint is destroyed. For the PCFs (LMA-10, LMA-5, NL-3.3-880 and PM-1550-01), the length of collapse region is about 600  $\mu\text{m}$ . As an example, Fig. 3.2(a) shows the splicing joint of LMA-10/SMF-28, the dotted circle encloses the collapsed region of LMA-10. So the light will expand significantly due to the disappearance of the difference between the refractive indices of the core and the cladding, thus causing huge splice loss. The splice losses measured were respectively 10.73 dB, 20.11 dB, 21.56 dB and 25.78 dB for SMF-28/LMA-10, SMF-28/ LMA-5, SMF-28/ NL-3.3-880 and SMF-28/ PM-1550-01 at 1550 nm. In the case of SMF-28/ HC-1550-02, the splicing joint could not even be formed because of serious collapsing due to excessive heating to HC-1550-02, as shown in Fig. 3.2(b). So it is very important to avoid serious collapse of air holes when fusion splicing PCFs and SMFs.

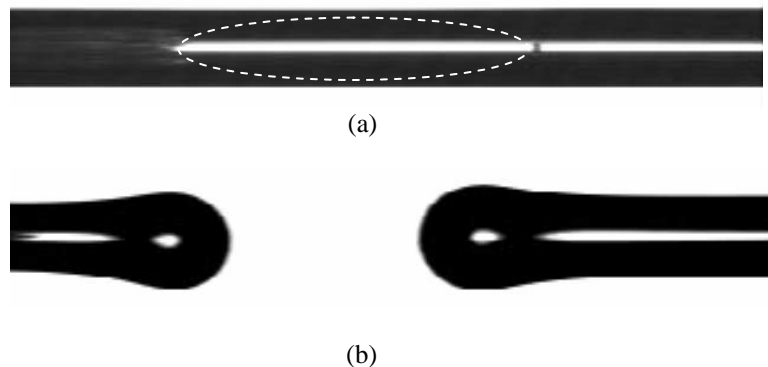


Figure 3.2 Side views of the splicing joint on the screen of FSU-975 splicer using the program set for conventional SMFs: (a) LMA-10/SMF-28, the dotted circle encloses the collapsed region of LMA-10; (b) HC-1550-02/SMF-28.

### 3.2.2 Mode field mismatch

The butt coupling loss  $\alpha$  between a PCF and a SMF in optimal alignment, can be approximately expressed by [9, 14].

$$\alpha = -20 \log \left( \frac{2\omega_{PCF}\omega_{SMF}}{\omega_{PCF}^2 + \omega_{SMF}^2} \right) \quad (2)$$

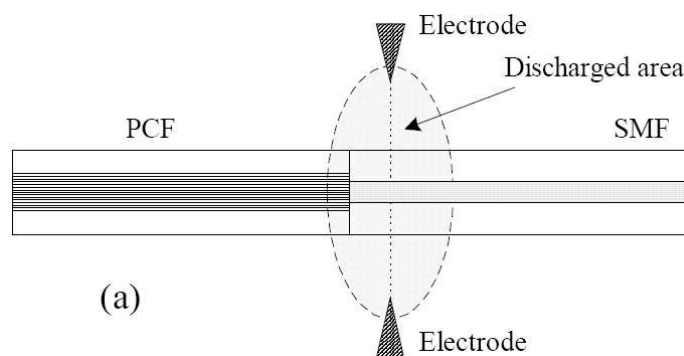
when the mode field distribution of the PCF is approximately Gaussian. Where  $2\omega_{PCF}$  and  $2\omega_{SMF}$  are respectively the MFDs of the PCF and the SMF. The butt coupling loss for light propagating from a SMF to a PCF was experimentally measured at 1550 nm. The butt coupling losses of SMF-28/LMA-10, SMF-28/HC-1550-02, SMF-28/LMA-5, SMF-28/NL-3.3-880 and SMF-28/PM-1550-01 are 0.41 dB, 1.50 dB, 3.62 dB, 8.14 dB and 4.88 dB respectively, which agree well with the theoretical estimation given by Eq. (2), i.e., 0.18 dB, 0.46 dB, 3.32 dB, 7.85 dB and 4.70 dB. The good agreement between the theoretical and the experimental results indicates that the loss mechanism is due to the mode mismatch between the PCF and the SMF. For PCFs, such as LMA-10 and HC-1550-02, which have similar MFDs as the SMFs, low-loss splicing can be achieved when the splice does not alter the MFD of the PCF. However, for the small-core PCF having much smaller MFD than the SMF, the splice loss is large, even when the air holes are kept intact, because of mode field mismatch.

### 3.3 The Principle of Low-loss Splicing

For fusion splicing of PCF/PCF, the PCFs have the same MFD for each other, so the splice loss between PCFs will be significantly low when avoiding air holes collapse in splicing; For the case of fusion splicing PCF/SMF, to avoid or minimize air hole collapse in splicing a PCF and a SMF, an effective way is to choose weaker fusion current and shorter fusion time, compared to the parameters of splicing SMF/SMF when fusion splicing PCF/SMF. However, suitable arc energy should be obtained to

soften the tips of the PCF and the SMF to achieve a good mechanical strength of the joint, and at the same time, minimize the collapse of air holes. So there is a tradeoff between the splice loss and mechanical strength. Another important parameter is “overlap”, which has not been paid much attention in previous research. “Overlap” means the overlap distance in which the two fibers are pushed further together because they have been softened as compared to when they are merely touched each other in butt-coupling. The tip part of the PCF is not softened enough when the arc discharge energy is low, so a large overlap may cause bend misalignment when the two fibers are pushed together, thus increasing the coupling loss. Therefore, choosing a suitable overlap during splicing is also very important.

Because the softening point of the PCF is lower than that of the SMF, it’s better to introduce a suitable offset [19], as shown in Fig. 3.3(a), between the joint and the central axis of the arc discharge, which will cause the arc discharge to affect the tip of the PCF weakly as compared with the tip of the SMF. This offset splicing method has two advantages: the first one is that it ensures a smaller amount of heat being applied to the PCF and thus it is easier to control the collapse of the air holes. The other is that it can balance the melting status by applying more heat to the SMF because the SMF in general has higher softening point than the PCF as mentioned above.



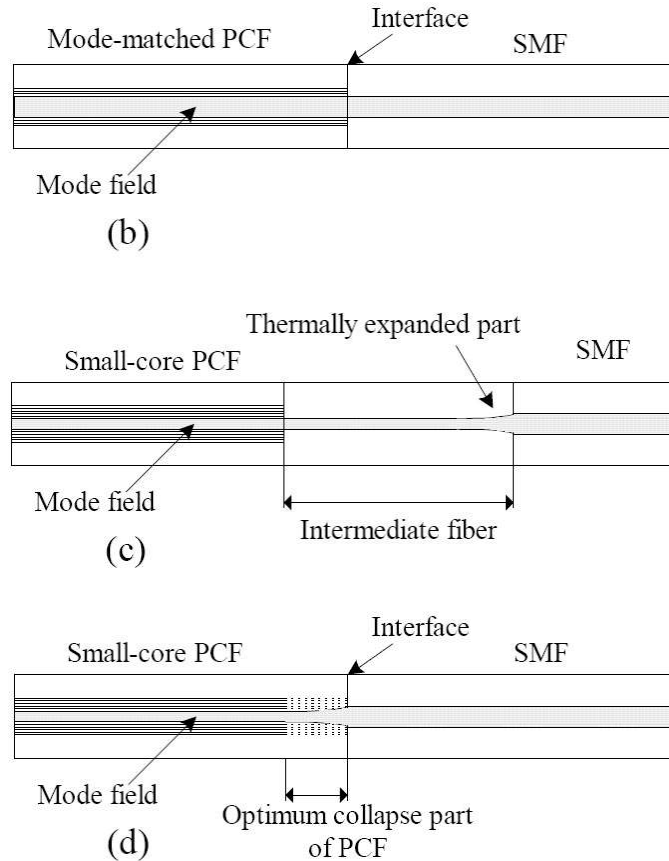


Figure 3.3 (a) splicing a SMF to a PCF with an offset of the joint to the central axis of arc discharge; (b) splicing a SMF to a PCF having the same MFD; (c) splicing a SMF to a small-core PCF with an intermediate fiber; (d) splicing a SMF to a small-core PCF with an optimum mode field match at the interface.

For fusion splicing SMFs and PCFs having similar MFDs, a low-loss joint with good mechanical strength can be formed by choosing a suitably weak fusion current, short fusion time, offset and overlap to minimize the collapse of air holes and well melt two fibers together, as shown in Fig. 3.3(b). However, for splicing small-core PCFs and SMFs, mode field mismatch can cause large splice loss even when the air holes do not collapse. It is generally the practice to use an intermediate fiber as a bridge section between the two fibers to decrease the splice loss. Here we will use a small-core fiber as an intermediate fiber, which will match the mode field of the small-core PCF when the core of the intermediate fiber is not expanded, and make a match with the SMF when the core is thermally treated to expand so as to have the

same MFD of the SMF, as shown in Fig. 3.3(c). Another simpler solution is to control the degree of the air hole collapse to realize low-loss splicing between a small-core PCF and a SMF without any intermediate fiber by repeated arc discharges. The principle of the method is to control the collapse of the air holes of the PCF gradually using a fusion splicer to obtain an enlarged mode field at the interface of the PCF that matches the mode field of the SMF, and at the same time, to optimize the rate of hole collapse in the PCF to achieve an adiabatic mode field variation in the longitudinal direction to reduce the transition loss. To gradually collapse the holes in the PCF, repeated weak arc discharges with a short duration after an initial arc discharge are applied over the splice joint to achieve the optimum mode field match between the PCF and the SMF at the splice interface, as shown in Fig. 3.3(d). However, for small-core PCFs with high air-filling fraction, the mode field will not expand even when the air holes collapse, so this method cannot be used in this kind of small-core PCF, and we have to use an intermediate fiber to decrease the splice loss. We provide a detailed analysis of the various techniques in the next sections.

### **3.4 Fusion splicing PCF/PCF experiment**

In our experiment, the PCF we chose to splice each other was LMA-10. To accurately measure the splice loss, we set the experiment as follows: first, two ends of a PCF LMA-10 with a length of about 1.5 meters were spliced to SMF-28 fibers, and the transmission power was recorded as a reference; secondly, the PCF LMA-10 was cleaved at the middle part and then the two cleaved ends were spliced to each other, and then the transmission power was measured again. The difference of the two measurements was taken as the PCF-PCF splice loss. To avoid air hole collapse, we chose the weak fusion current and short fusion time. The PCF was cleaved using

a Furukawa S324 cleaver. The possibility of high quality cleaving (a flat end-face of PCF) is above 90%. Because the tip of the PCF is not totally softened during splicing, any defect (such as large cleave angle) will cause extra splice loss and make the joint fragile, so the PCF with a flat end-face must be chosen. It should be mentioned that in practical handling the PCF cannot be cleaned with solvents after cleaving because the solvent will seep into the air holes of the PCF by capillary action, thus changing the light guiding properties, which will result in huge splice loss.

To compare the parameters-set of PCF/PCF splicing with that of conventional SMF/SMF splicing, we first give the typical parameters of an Ericsson FSU-975 fusion splicer set for splicing two conventional SMFs. The parameters are: gap 50  $\mu\text{m}$ , overlap 10  $\mu\text{m}$ , pre-fusion time 0.2 s, pre-fusion current 10.0 mA; fusion time one 0.3 s, fusion current one 10.5 mA; fusion time two 2.0 s, fusion current two 16.3 mA; fusion time three 2.0 s, fusion current three 12.5 mA; the center position is 255. During pre-fusion the fibers are cleared of some dirt on the fiber surface by low level heating, pre-fusion time and current are the duration and magnitude of discharge current applied to the electrodes when the two fibers are cleared by low level heating before splicing. The main fusion process is fusion time two and fusion current two, which are the duration and magnitude of discharge current applied to the electrodes when the two fiber ends are pushed together. Fusion time one and fusion current one are the duration and magnitude of discharge current applied to the electrodes to soften the fiber ends before the ends are pushed together. Fusion time three and fusion current three are to anneal the fusion joint. To avoid applying excess energy and easily perform discharge tests, we set the fusion time one and three to zero, and then set fusion time two to 0.3 s and fusion current two to 9.5 mA.

The prefusion current and overlap were set to 5.0 mA and 5  $\mu\text{m}$ , respectively. The other parameters are chosen to be the same as the parameters for splicing conventional fibers, and then the PCFs are aligned and spliced by the splicer automatically. The smallest splice loss (0.11 dB) was achieved and the corresponding splicing joint is shown in Fig. 3.4.

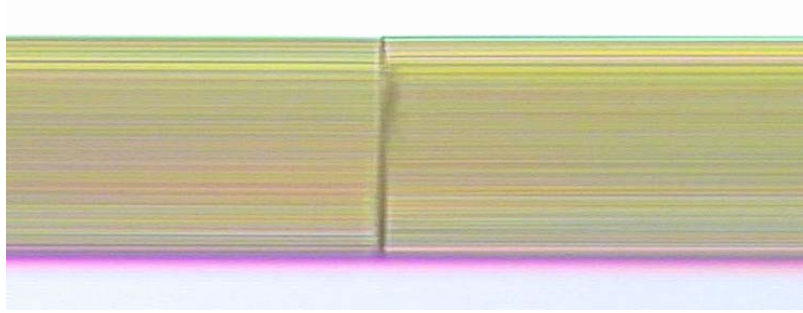


Figure 3.4 Optical microscopy image of the fusion joint of LMA-10/LMA-10 when the splice loss is 0.11 dB.

We cannot observe any visible difference of air hole structures between the spliced region of the LMA-10 and the region of far away from the splice joint, so the collapse of air holes can be avoided, and the corresponding splicing joint has good mechanical strength and can be bent in a circle with the radius of about 1.3 cm before breaking. Five splices were done that yielded an average splice loss of 0.17 dB with a standard deviation of 0.04 dB.

### 3.5 Low-loss fusion splicing SMF/PCF experiments

In this section, we investigated low-loss fusion splicing different PCFs with SMF-28 experimentally. First, the power of the 1550 nm source at the output of a SMF-28 fiber was measured, and then the PCF with one end coupled to a power meter was spliced to the SMF-28 fiber to detect the coupling power, and then the un-spliced end of the PCF was subsequently spliced to another SMF-28 fiber in the same condition and the output power was again measured to observe splice reciprocity.

In our experiments, to investigate the effect of arc discharge and easily perform

discharge tests, we set the fusion time one and three to zero and then set fusion time two to 0.3s and varied fusion current two. The prefusion current was set to 5.0 mA instead of 10 mA to avoid any heat collapse of the holes of the PCF before fusion splicing. We set the center position to 205, corresponding to an offset distance of 50  $\mu\text{m}$ . We chose suitable overlap for different PCFs during fusion splicing. The other parameters are chosen to be the same as the parameters for splicing conventional fibers, and then the two fibers are aligned and spliced by the splicer automatically.

### 3.5.1 Splicing SMF to Solid-core PCF with Similar MFDs

The PCF LMA-10 and SMF-28 having similar MFDs were chosen to perform splicing experiments. We set overlap to 5  $\mu\text{m}$ , the fusion current time to 0.3 s and varied the fusion current from 9 mA to 14 mA with a step of 1 mA. The results are shown in Fig. 3.5.

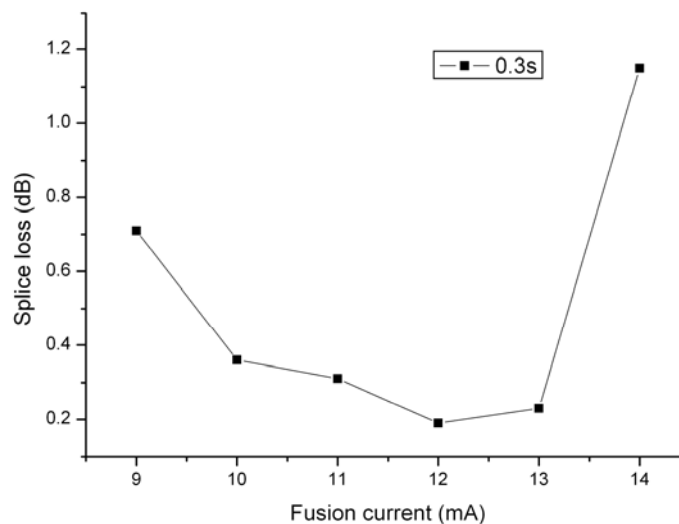


Figure 3.5 The splice losses of SMF-28/LMA-10 as a function of the fusion current when the fusion time is fixed at 0.3s. The offset and overlap are respectively 50  $\mu\text{m}$  and 5  $\mu\text{m}$ .

The splice losses are less than 0.4 dB when the fusion current is in the range of 10 mA to 13 mA, they are respectively 0.36 dB, 0.31 dB, 0.19 dB and 0.23 dB for fusion currents of 10 mA, 11 mA, 12 mA and 13 mA; the corresponding splicing

joints have good mechanical strength and can be bent in a circle with the radii of about 6 cm, 4 cm, 1.8 cm and 1 cm respectively before breaking. The smallest splice loss (0.19 dB) was achieved when the fusion current was 12 mA; the corresponding splicing joint is shown in Fig. 3.6.

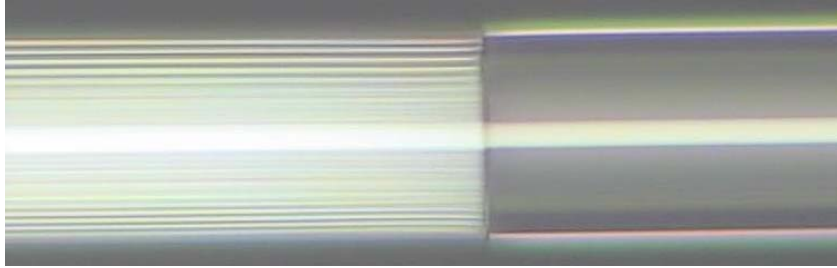


Figure 3.6 Optical microscopy image of the fusion joint of LMA-10/SMF-28 when the splice loss is 0.19 dB.

We can observe that there is no visible difference of air hole structures between the spliced region of the LMA-10 and the region of far away from the splice joint, which means that a low-loss splicing joint was formed because air hole collapse was largely avoided. Statistically, ten splices were done that yielded an average splice loss of 0.32 dB with a standard deviation of 0.07 dB. The splice loss from LMA-10 to SMF-28 was 0.30 dB. The loss difference in two opposite directions is within the deviation, thus the splice is optical reciprocal.

### 3.5.2 Splicing SMF to hollow-core PCF with similar MFDs

Low-loss fusion splicing between a hollow-core PCF (also named PBG fiber) and a SMF is more difficult [ 12-14] and only one paper [14] provided the details on the fusion process and fusion parameters recently. Here, we first investigated the effect of the fusion current on the collapse of the air holes of a hollow-core PCF, and then measured the splice loss for different values of fusion current.

The hollow-core PCF HC-1550-02 and SMF-28 having similar MFDs were chosen to perform the experiments. Because the hollow-core PCF reaches softening

point more readily and its central region caves in [12] due to surface tension, we set overlap 10  $\mu\text{m}$  to obtain good mechanical strength when fusion splicing. We fixed fusion time to 0.3 s and changed the fusion current from 9 mA to 11.5 mA in steps of 0.5 mA. By withdrawing the SMF-28 just before the start of the arc discharge, the tip of the HC-1550-02 was not spliced to the SMF-28 but heated by the arc discharge, so we could check the degree of air collapse. Fig. 3.7 shows the SEM images of the end face of HC-1550-02 when the fiber was subjected to an arc discharge from various fusion currents.

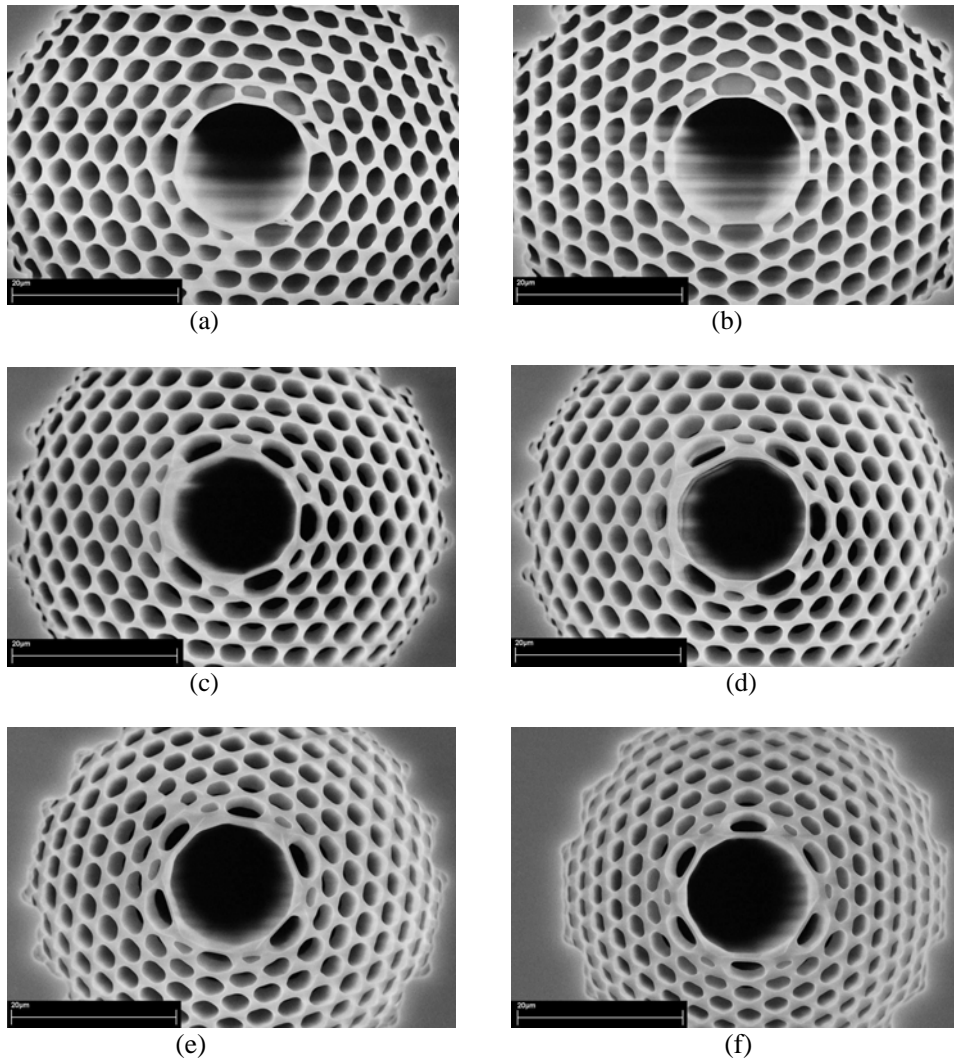


Figure 3.7 End views of the HC-1550-02 with different fusion current when the fusion time was fixed at 0.3 s, the offset was fixed at 50  $\mu\text{m}$ : (a) 9 mA, (b) 9.5 mA, (c) 10 mA, (d) 10.5 mA, (e) 11 mA, (f) 11.5 mA.

We can observe that the collapse of the cladding holes increases with the increase of the fusion current. Because of the high air-filling fraction of the air-silica cladding, there is a thermal gradient when the heat transfers from the solid silica ring cladding to the center of the holey region. When the fusion current is 9 mA, only the first outer air holes collapse partially; when the fusion current is increased to 10 mA, two outer air holes collapse; fusion current 11 mA and 11.5 mA correspond to the collapse of three and four outer air holes respectively. The surface tension also makes the central air-silica region cave in and the degree of the recess of the end part of the PCF increases with the increase of the fusion current. The splice loss was increased when the fusion current increased from 9 mA to 11.5 mA, as shown in Fig. 3.8.

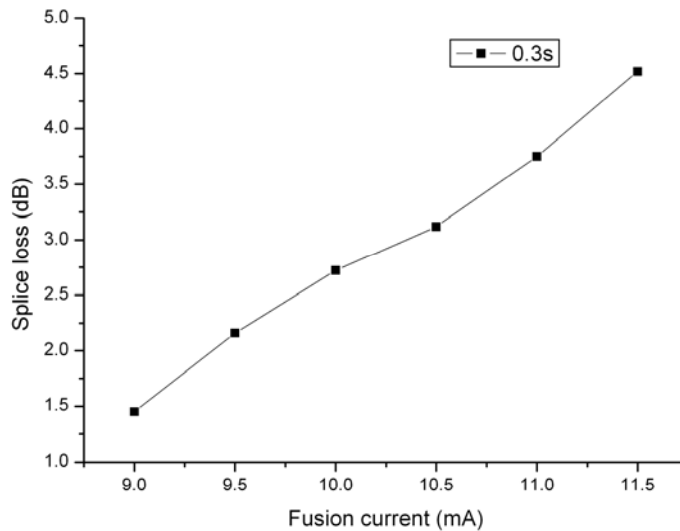


Figure 3.8 The splice losses of SMF-28/HC-1550-02 measured versus the fusion current with the fixed fusion time 0.3s. The offset and overlap are respectively 50  $\mu\text{m}$  and 10  $\mu\text{m}$ .

The increasing splice loss with the fusion current is due to two reasons: one is that distorting the periodic air-silica cladding structure will increase the confine loss at the splice joint, the other is that the increasing recess which created an air gap

between two fiber cores will increase the coupling loss because the light coming out from the SMF will expand quickly when there is an air gap. The lowest splice loss (1.45 dB) was achieved when the fusion current was 9 mA, the corresponding splicing joint, which is shown in Fig. 3.9, had good mechanical strength and could be bent to a radius of about 2.5 cm before breaking. The splicing result is of the same order of the best result reported [14] and only need one arc discharge. From Fig. 3.9, we cannot observe visible collapse when we compare the spliced and un-spliced region of the PCF. Thus, we have demonstrated that low-loss splicing between hollow-core PCF and SMF can be achieved even with a single arc discharge when we choose suitable parameters. Ten splices were done using the above method that yielded an average splice loss of 1.87 dB with a standard deviation of 0.18 dB in the range of 1.45 dB ~ 2.01 dB. The splice loss from HC-1550-02 to SMF-28 was 2.48 dB, thus the difference of the splice losses in two opposite directions is significant large. It is because the higher order modes were excited in the HC-1550-02 which can not couple well to the SMF-28 [14].

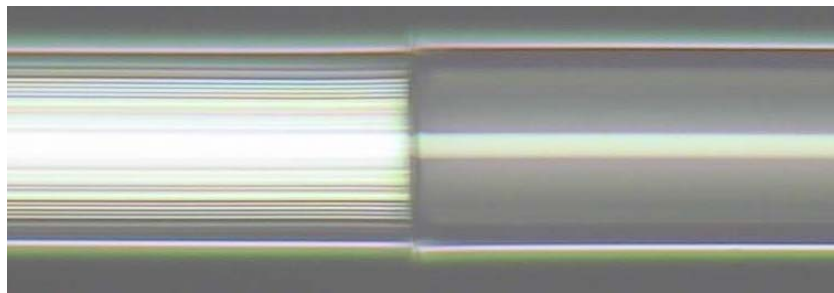


Figure 3.9 Optical microscopy image of the fusion joint of HC-1550-02/SMF-28 with the splice loss of 1.45 dB.

### 3.5.3 Splicing SMF to small-core PCF with low-air filling fraction

In Ref. [20], Frazão et al. achieved low-loss splicing between a small-core PCF (NL- 2.3-1555) and SMF-28 using a fusion splicer. However, the authors did not give a proper explanation about the results because low-loss splicing cannot be

achieved due to mode field mismatch when the air holes of small-core PCF are not collapsed, as explained earlier.

In our experiments, the small-core PCF we chose to splice to SMF-28 was LMA-5. It has a pitch of  $2.9 \mu\text{m}$  and relative hole size of 0.44. Because the total silica area of the PCF remains constant during air hole collapse, we can obtain the approximate relation [21]:

$$\left(\frac{\Lambda}{\Lambda_0}\right)^2 = \frac{\frac{\sqrt{3}}{2} - \frac{\pi}{4} \left(\frac{d_0}{\Lambda_0}\right)^2}{\frac{\sqrt{3}}{2} - \frac{\pi}{4} \left(\frac{d}{\Lambda}\right)^2} \quad (3)$$

where  $\Lambda_0$  and  $d_0$  are the initial values of pitch and air hole diameter, and  $\Lambda$  and  $d$  are the values of pitch and air hole diameter after collapsing. When air holes collapse, the pitch decreases with the decrease of the relative hole size according to Eq. (3). The MFD can be calculated by finite element method [22-23]. It increases with the decrease of relative hole size, as shown in Fig. 3.10, the corresponding intensity distributions are shown in Fig. 3.11.

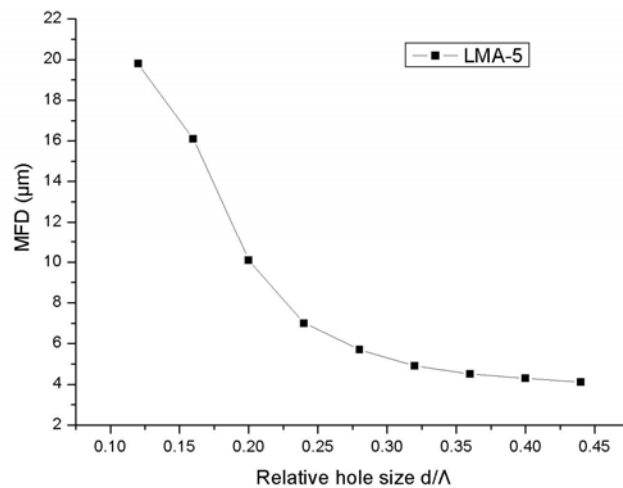


Figure 3.10 The mode field diameter (MFD) of PCF LMA-5 as a function of the relative hole size ( $d/\Lambda$ ).

The initial MFD is  $4.1 \mu\text{m}$  at the wavelength of  $1550 \text{ nm}$ ; it increases to  $4.5 \mu\text{m}$  when  $d/\Lambda$  decreases to from  $0.44$  to  $0.36$ , and it reaches  $10.1 \mu\text{m}$  when  $d/\Lambda$  is  $0.2$ , which has a perfect MFD match with the conventional SMF, as shown in Fig. 3.11(c). However, when the air holes collapse further and  $d/\Lambda$  decreases more, such as  $0.12$ , the mode field of LMA-5 expands dramatically to be  $19.8 \mu\text{m}$ , as shown in Fig. 3.11(d), which will cause large mode mismatching loss again.

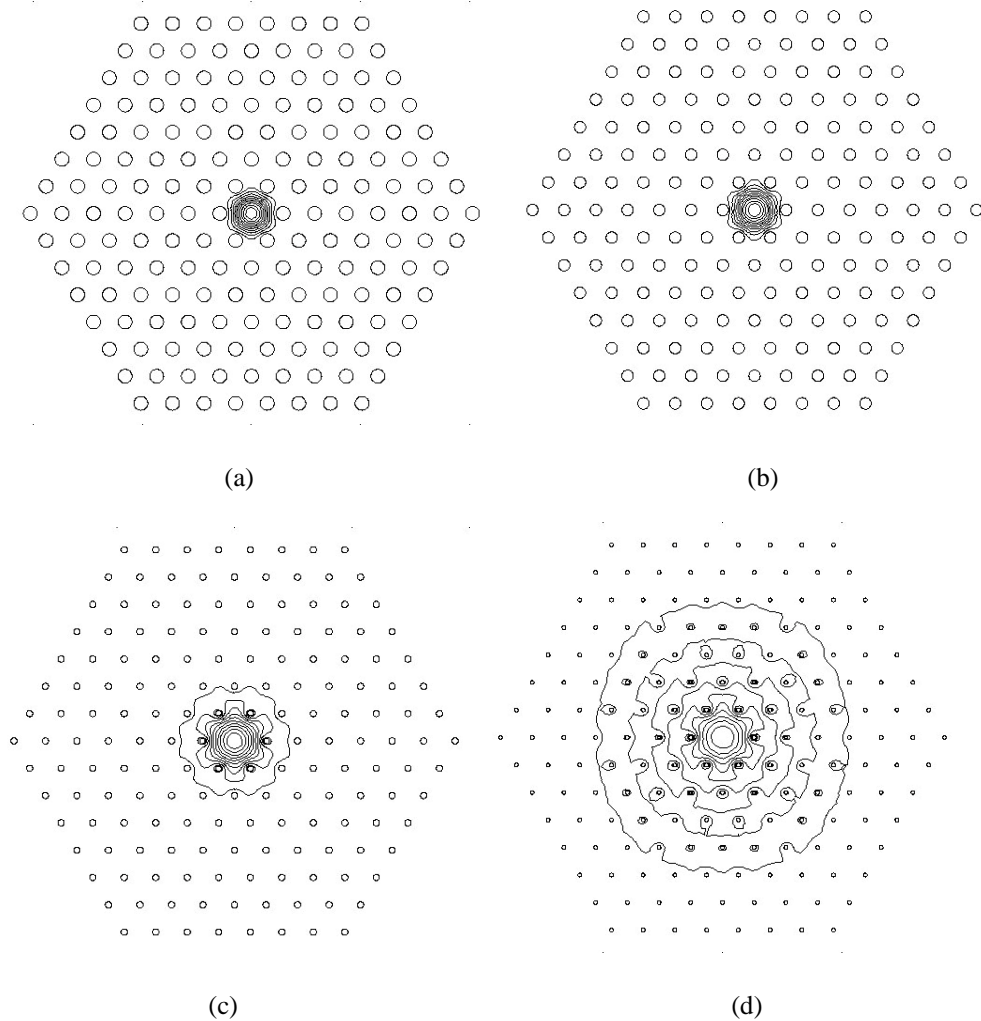


Figure 3.11 Contour plots of intensity distribution of the PCF LMA-5 with different relative hole size: (a)  $0.44$  (b)  $0.36$  (c)  $0.20$  (d)  $0.12$  at  $1.55 \mu\text{m}$ .

The theoretical splice loss between LMA-5 with various relative hole size and SMF-28 can be calculated according to Eq. (2). The minimum theoretical splice loss

can be as low as 0.003 dB when  $d/\Lambda$  is 0.2, as shown in Fig. 3.12. However, the main experimental challenge is how to control the rate of air hole collapse and obtain the optimum air-hole size. Our method is to control the collapse of the air holes of the PCF gradually using a fusion splicer to obtain an enlarged mode field at the interface of the PCF that matches the mode field of the SMF. To achieve the optimum mode field match between the PCF and the SMF at the splice interface, repeated weak arc discharges with a short duration after an initial arc discharge are applied over the splice joint to gradually collapse the holes in the PCF, as mentioned in section 3.3.

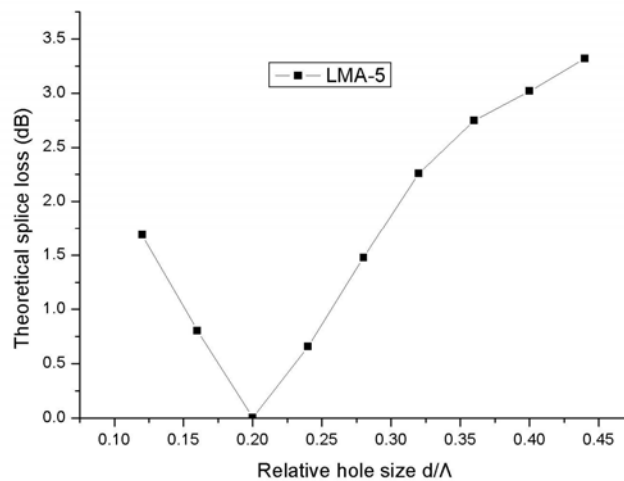


Figure 3.12 Theoretical splice loss of SMF-28/LMA-5 as a function of relative hole size ( $d/\Lambda$ ).

Another important problem is how to achieve an adiabatic mode field variation in the longitudinal direction to reduce the transition loss, as shown in Fig. 3.3 (d). Fig. 3.13 illustrates the temperature distribution near the end of the small-core PCF during fusion splicing. The temperature decreases gradually along the fiber axis away from the splicing joint [18], which will cause an adiabatic air-hole collapse along the longitudinal direction of the small-core PCF, so an adiabatic mode field

enlargement toward the splice interface can be formed.

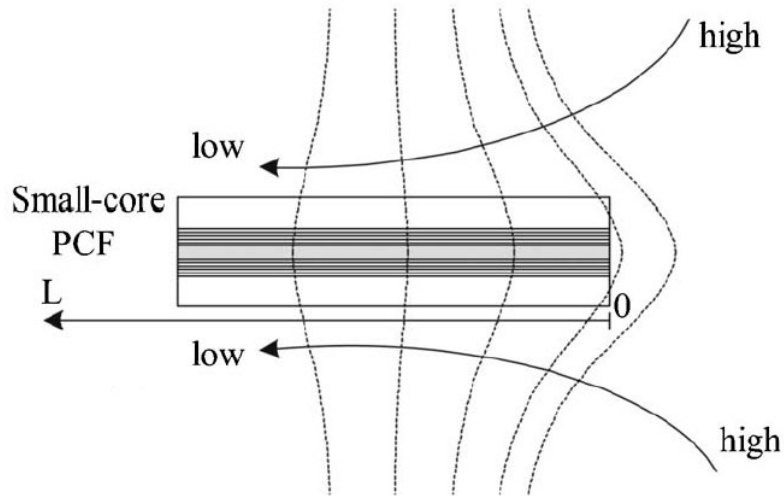


Figure 3.13 The temperature distribution field along the longitudinal direction of the small core PCF when fusion splicing.

After introducing the detailed mechanism of low-loss splicing of SMF-28/LMA-5, we investigated low-loss fusion splicing them experimentally. We set overlap  $1\ \mu\text{m}$ , the offset  $50\ \mu\text{m}$  and fixed fusion time at  $0.3\ \text{s}$ . To illustrate the degree of air hole collapse, we firstly observed the end face of the LMA-5 by SEM after various arc-discharges. The fusion current used was  $10.0\ \text{mA}$ . By withdrawing the SMF just before the start of the arc discharge (the method we mentioned above), we can observe the collapse of the end face of the PCF as a result of the arc discharge. We applied repeatedly arc discharges with the same power to heat the LMA-5. Figs. 3.14(a), (b), (c) and (d) show the SEM images of the LMA-5 end face after respectively 2, 5, 7 and 9 discharges; the time gap between two consecutive discharges is  $2\ \text{s}$ .

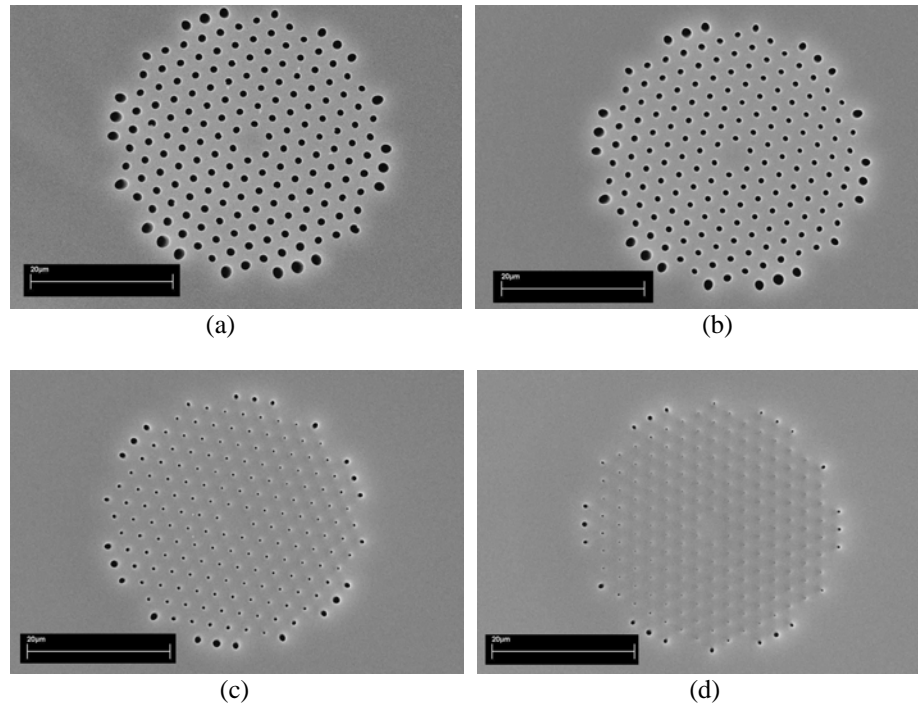


Figure 3.14 End views of the LMA-5 after (a) 2, (b) 5, (c) 7 and (d) 9 discharges. The fusion time, current, and offset are respectively 0.3s, 10 mA and 50  $\mu\text{m}$ .

We observed that the average hole diameter was 0.83  $\mu\text{m}$  when the number of arc discharges was 2, the holes shrunk to 0.70  $\mu\text{m}$  and 0.24  $\mu\text{m}$  after 5 and 7 discharges, and almost all the holes are closed after 9 discharges. We found that the micro-hole collapse of LMA-5 was quite different from the collapse of HC-1550-02. All the holes shrunk at the same rate and there was almost no recess in the air-silica region. This is because heat can transfer quickly in the low air-filling fraction air-silica structure, thus no significant thermal gradient exists in the PCF's cross section. And because the solid silica part, from which most of the air-silica cladding is made of, can sustain the air-silica structure when the air holes shrink, the end surface of the PCF will not cave in when exposed to heat during splicing.

We then performed fusion splicing between LMA-5 and SMF-28. It should be mentioned that the collapse of holes is expected, for the same number of discharges, to be slower during the actually splicing process. This is because more heat will

apply to the end of the LMA-5 due to the exposure of the end face when they are not fused together. The splicing losses measured at 1550 nm, for light propagating from SMF-28 to LMA-5, as functions of the number of discharges and the fusion current, are shown in Fig. 3.15.

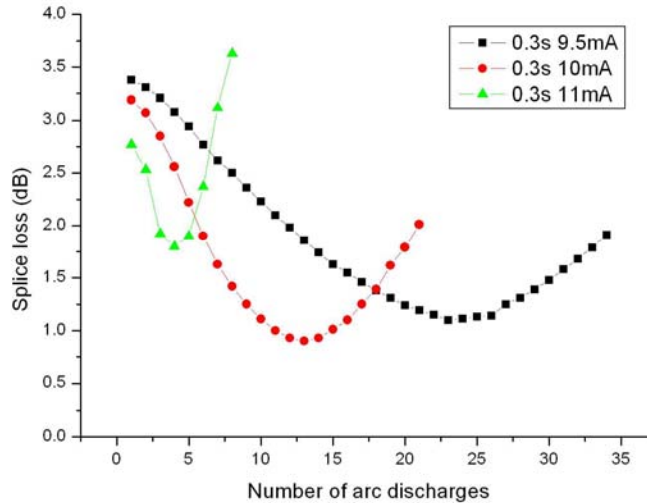


Figure 3.15 The splice losses of SMF-28/LMA-5 as a function of the number of arc discharges with fusion current as a parameter. The fusion time, offset and overlap are respectively 0.3s, 50  $\mu\text{m}$  and 1  $\mu\text{m}$ .

The splicing loss, after a single discharge, are respectively 3.38 dB, 3.19 dB, and 2.77 dB for fusion currents of 9.5 mA, 10 mA, and 11 mA. The single discharge splice loss for 11 mA fusion current is considerably lower than the theoretical value (3.32 dB). This is because of the hole-collapse induced by the relatively larger current, which enlarges the mode field area and make it matches more to that of the SMF. The splice loss obtained from a single discharge cannot be further reduced if we use a fusion current greater than 11 mA. It is because we find that the microholes of small-core PCF LMA-5 collapse significantly when the fusion current is larger than 11 mA. However, it is difficult to achieve optimal hole-collapse and hence minimum splice loss. It would be much easier to apply repeated weak discharges

and to optimize the splice loss by controlling the number of discharges. It can be seen from Fig. 3.15 that, for fusion currents of 9.5 mA, 10.0 mA and 11 mA, the minimum splice loss of 1.1 dB, 0.9 dB and 1.8 dB can be obtained after 23, 13 and 4 arc discharges. We can find that the plots in Fig. 3.15 show different minimum values. It is because the degree of optimized hole-collapse is different, then the degree of mode-matching is different when we use various fusion current and times of arc discharge. Fig. 3.16 shows that the side views of the splicing joints with 10.0 mA discharge current after 1, 13 and 21 times of discharges.

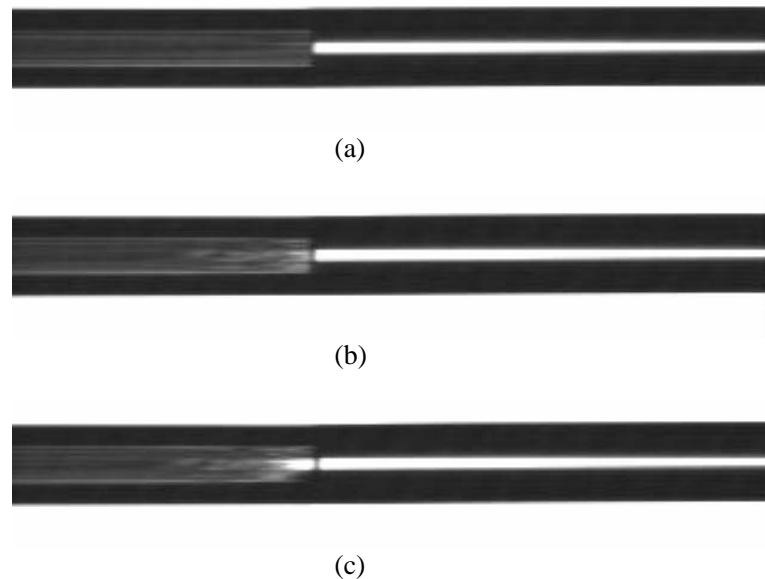


Figure 3.16 Side views on the screen of FSU-975 splicer of the splicing joints between LMA-5 and SMF-28 fibers after (a) 1, (b) 13, (c) 21 discharges. The fusion time, current and the offset distance are respectively 0.3 s, 10 mA and 50  $\mu\text{m}$ .

In Fig. 3.16(a), the hole-collapse is minimal and the splice loss is large (3.19 dB) due to the mode field mismatch. In Fig. 3.16(b), the holes of the PCF collapse to certain degree that enlarges the mode field in the PCF and optimizes the mode field match between the two fibers and hence minimizes the splicing loss (0.9 dB). In Fig. 3.16(c), the holes are collapsed significantly, which makes the mode field area in

PCF larger than that of the SMF and hence increases the splice loss. As expected, the number of arc discharges required to reach the minimum splicing loss was reduced when using a larger fusion current because the degree of air hole collapse increases with the increase of the heating power. The use of a smaller fusion current is easier to achieve the minimum splicing loss by controlling the step of collapsing more precisely. Fig. 3.17 shows optical microscopy image of the splicing joint with 10.0 mA discharge current after 13 discharges. We can observe clearly that the holes of the LMA-5 have collapsed gradually to a certain degree, resulting in an enlarged mode field in the PCF which optimized the mode field match between the two fibers and hence minimized the splice loss. The minimum experimental loss (0.9 dB) obtained may be caused by non-perfect mode field mismatch at the PCF/SMF interface and by the mode field expansion (transition) loss in the gradual hole-collapsing part of the small-core PCFs. Because of the short transition length as can be observed from the side views of the collapse part in Fig. 3.16(b) and Fig. 3.17, the mode field transition loss may not be neglected. We believe the splicing loss should be further reduced by optimizing the transition length through the use of a wider electrode gap as has been used in splicing the SMF and the small-core Er-doped fiber [24].

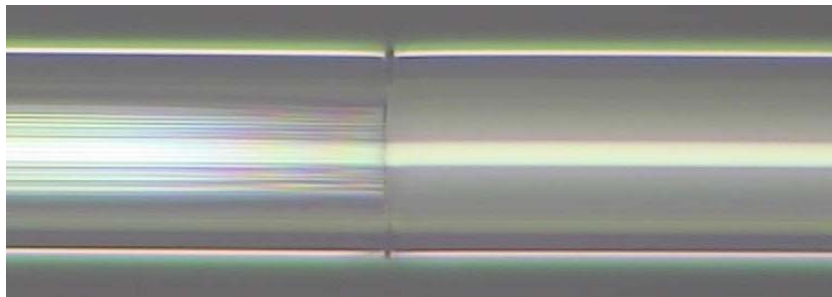


Figure 3.17 Optical microscopy image of the fusion joint of LMA-5/SMF-28 with the splice loss 0.90 dB.

Five splices were done and the measured loss was in the range of 0.90 ~ 1.41 dB

that yielded an average splice loss of 1.14 dB with a standard deviation of 0.18 dB. The splice loss from LMA-5 to SMF-28 was 1.09 dB, which proved it has good splice reciprocity. The mechanical strength was not very good: the bending radius was about 10 cm before the fibers broke when the overlap was 1  $\mu\text{m}$ . However, the splicing joint can be bent in a circle with a minimum radius of about 2 cm before breaking when the overlap changed to 3  $\mu\text{m}$ , with the splice loss still being approximately the same.

The same method was used to splice SMF-28/NL-1550-POS-1, as shown in Fig. 3.18. The NL-1550-POS-1 has an average core diameter of about 2.1  $\mu\text{m}$ . The MFD and NA of the NL-1550-POS-1 are about 2.8  $\mu\text{m}$  and 0.4 at 1550 nm.

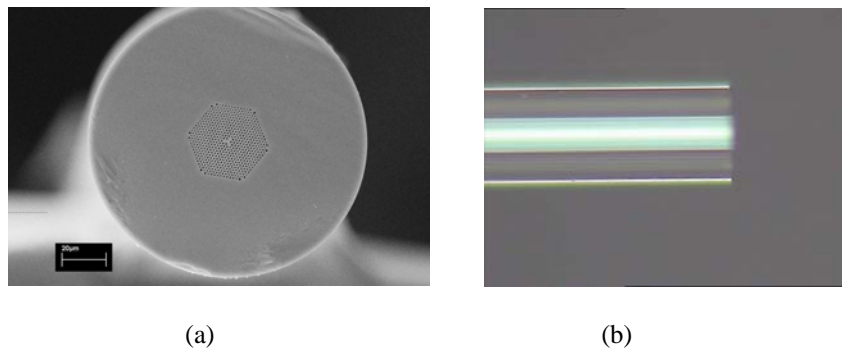


Figure 3.18 (a) SEM photographs of the cross section and (b) optical microscope image of the side view of NL-1550-POS-1.

The butt-coupling loss of SMF-28/ NL-1550-POS-1 is 6.30 dB, which agrees well with the theoretical estimation given by Eq. (2), i.e., 5.98 dB. The minimum splice loss was significantly less than the butt-coupling loss; the results are shown in Fig. 3.19. For splicing SMF-28/NL-1550-POS-1 (Fig. 3.19), when the fusion currents were 9.5 mA and 10.0 mA, the minimum splicing losses of 1.20 dB and 1.75 dB were obtained after 33 and 8 discharges, respectively. The splicing joint for a loss of 1.20 dB is shown in Fig. 3.20. We can observe clearly the difference of the PCF structure in the region near and away from the splice.

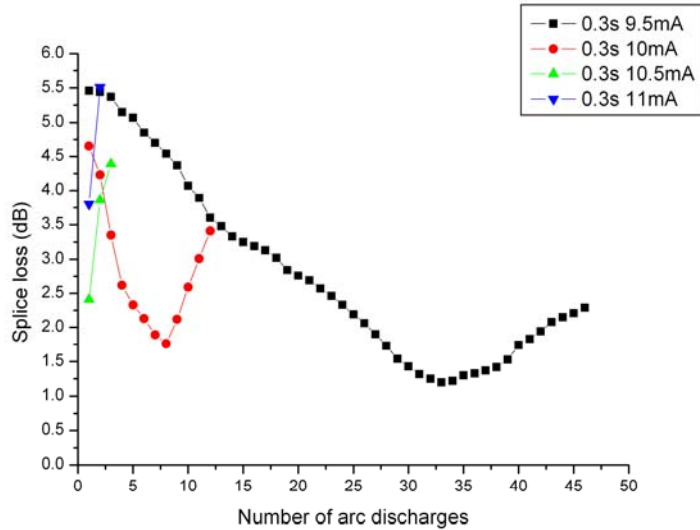


Figure 3.19 The splicing losses of SMF-28/NL-1550-POS-1 as a function of the number of arc discharges with fusion current as a parameter. The fusion time, offset and overlap are respectively 0.3s, 50  $\mu\text{m}$  and 3  $\mu\text{m}$ .

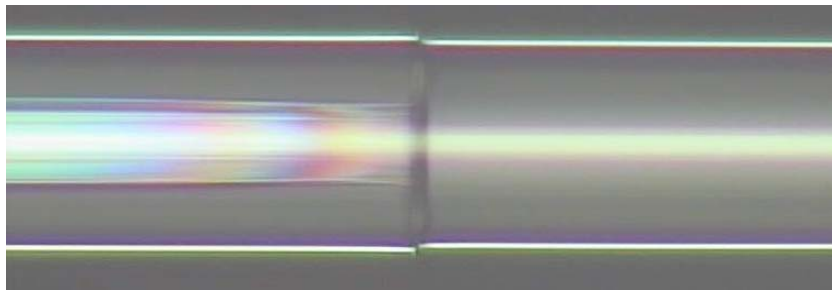


Figure 3.20 Optical microscopy image of the fusion joint of NL-1550-POS-1 and SMF-28 with the splice loss 1.20 dB.

Five splices were done when the fusion current was 9.5 mA that yielded an average splice loss of 1.61 dB with a standard deviation of 0.37 dB. The splicing joint can be bent in a circle with a minimum radius of about 2 cm when the overlap is 3  $\mu\text{m}$ . For fusion current of 10.5 mA and 11 mA, the minimum splicing losses (2.41 dB and 3.80 dB) occurred after the first discharge; further discharges increased the splicing loss. The standard deviation of experimental losses of the splicing between SMF-28/NL-1550-POS-1 was larger than that of SMF-28/LMA-5. This might be caused by the aberration of the transverse alignment because the smaller core is more sensitive to misalignment when the two fibers are aligned and

spliced automatically.

The small-core PCFs we successfully tested have low air-filling fraction cladding, and thus the guiding mode of this kind of small-core PCFs pervades into the air-silica cladding, hence the MFD is generally larger than the diameter of the solid core. When the micro-holes shrink, the guiding mode can expand and the end surface of the collapsed PCF keeps flat, which contributes to the low-loss splice of this kind of PCF to the SMF. However, this method cannot be used to improve the coupling efficiency between the SMF and the small-core PCF with high air-filling fraction, as will be discussed in the next part.

#### **3.5.4 Splicing SMF to small-core PCF with high-air filling fraction**

The small-core PCF with high air-filling fraction generally has about 90% air-filling ratio in the air-silica cladding region. For this kind of small-core PCF, the function of the air-silica cladding is to support the extremely small silica core with a very low refractive index (just over 1) medium. The optical properties of the core closely resemble those of a glass micro-rod suspended in the air, resulting in strong confinement of the light and a large nonlinear coefficient. The MFD of this kind of small-core PCF is generally smaller than the diameter of the core. The small-core PCF we chose in our experiment was NL-3.3-880.

To explore the micro-hole collapse property of this kind of small-core PCF, the same method as in 3.5.2 section (withdraw the SMF before the start of arc discharge) was used. Fig. 3.21 shows the end views of NL-3.3-880 when the fiber was subjected to an arc discharge from 12 mA to 14.5 mA.

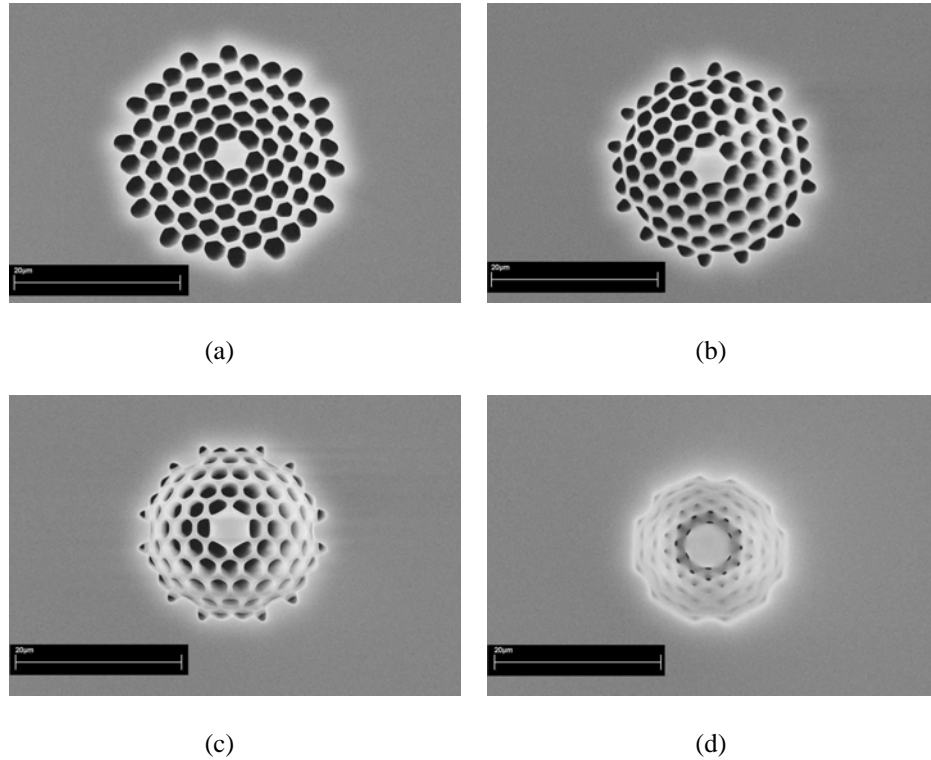


Figure 3.21 End views of the NL-3.3-880 with different fusion current when the fusion time was fixed at 0.3 s, the offset was fixed at 50  $\mu\text{m}$ : (a) 12 mA, (b) 13 mA, (c) 14 mA, (d) 14.5 mA.

We can observe that the collapse of the cladding holes of NL-3.3-880 is similar to that of the hollow-core PCF. When the fusion current is 14 mA, two outer air holes collapse totally but three inner air holes are still open, as shown in Fig. 3.21(c). The guiding light is still strongly confined to the small-core by the inner six holes around the core, rather than pervades into the air-silica cladding. This does not give rise to an increase in the MFD of the PCF, thus the partial collapse of air holes in this kind of small-core PCF does not improve the coupling efficiency. Furthermore, the central part of the small-core PCF caves in when air holes collapse because of the high air-filling fraction of the air-silica cladding. Consequently, just like the hollow-core PCF, the air gap between the two fibers gives rise to an increase in the splice loss due to the cave-in. When the fusion current increases to 14.5 mA, the inner air holes shrink to about 0.4  $\mu\text{m}$ , as shown in Fig. 3. 21(d). At this time, the mode field expands, however, the degree of recess also increases, so it is hard to

judge whether the partial collapse can be of benefit to the coupling efficiency. The experiments, by repeated arc discharges, were then done, as shown in Fig. 3.22. The splice losses increased with the number of arc discharges, which proves that the partial collapse of air holes cannot improve the coupling efficiency and the recess of the end face of the PCF increases the coupling loss. After eleven arc discharges with a fusion current of 13 mA, the splice loss increased from 8.58 dB to 10.74 dB. As shown in Fig. 3.23, the recess part of the PCF is clearly visible from the side view.

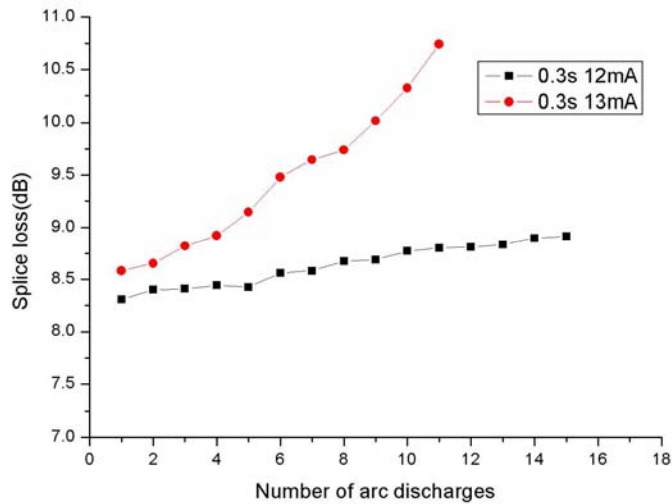


Figure 3.22 The splice losses of SMF-28/NL-3.3-880 as a function of the number of arc discharges with fusion current as a parameter. The fusion time, offset and overlap are respectively 0.3s, 50  $\mu\text{m}$  and 5  $\mu\text{m}$ .

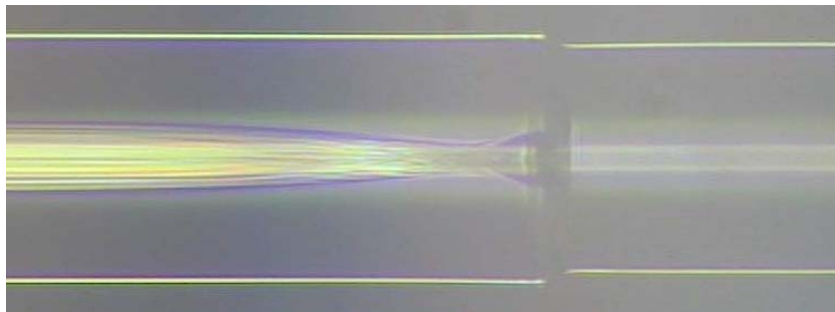


Figure 3.23 Optical microscopy images of the fusion joints of NL-3.3-880/SMF-28 with the splice loss 10.74 dB.

Because partial collapse cannot be used to splice the small-core PCF with high

air-filling fraction to the conventional SMF, another method using an intermediate fiber to solve the mode mismatch problem should be utilized, as mentioned in section 3.3. Here we use the fiber UHNA3 from Nufern company as an intermediate fiber. The MFD and NA of UHNA3 at 1550 nm are about  $4.1 \mu\text{m}$  and 0.35. The theoretical losses of UHNA3/SMF-28 and UHNA3/NL-3.3-880 are about 3.32 dB and 1.58 dB respectively according to Eq. (2). UHNA3 has a thermally expanded core (TEC), thus making it possible for the mode field to expand, so that it matches the mode field of SMF-28 when suitable heating is applied by the fusion splicer. TEC technology for conventional mode mismatch fibers such as erbium-doped fibers has been widely used and the fusion splicer has the splice parameter set for this operation. We used Program 06 of Ericsson FSU-975 to splice SMF-28 to UHNA3 to achieve a splice loss of about 0.60 dB, and then we spliced UHNA3 to NL-3.3-880 without collapsing the air holes, using the same method described in section 3.5.1. The splice joint of UHNA3/NL-3.3-880 is shown in Fig. 3.22, corresponding to a loss of about 1.93 dB, which is a little larger than the butt-coupling loss. We can conclude that the total splice loss can decrease to about 2.53 dB using an intermediate fiber.

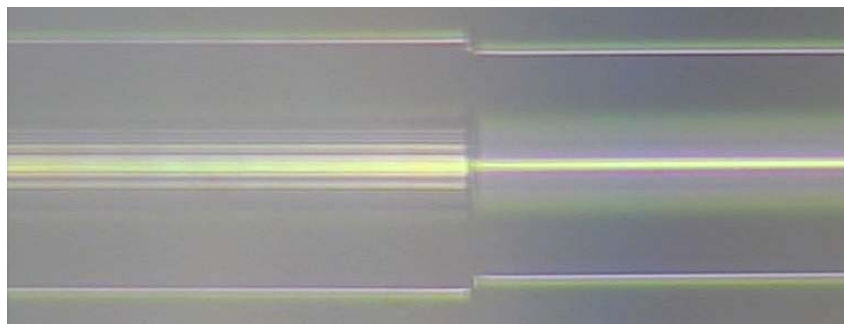


Figure 3.24 Optical microscopy images of the fusion joints of NL-3.3-880/UHNA3 with the splice loss 1.93 dB.

### 3.5.5 Splicing SMF to polarization maintaining PCF

Polarization maintaining PCF we used in our experiments was PM-1550-01, which has different micro-hole sizes in two perpendicular transverse directions. Because the air-filling fraction of PM-1550-01 is not high, the nature of its hole collapse is similar to the small-core PCF with low air-filling fraction, so partial collapse of air holes can increase the coupling efficiency when the MFD of PM-PCF is smaller than that of the conventional fiber. However, because the rate of hole collapse is almost same and the size of micro-holes is rather different, the larger holes still open when the small holes collapse to close, as shown in Fig. 3.25.

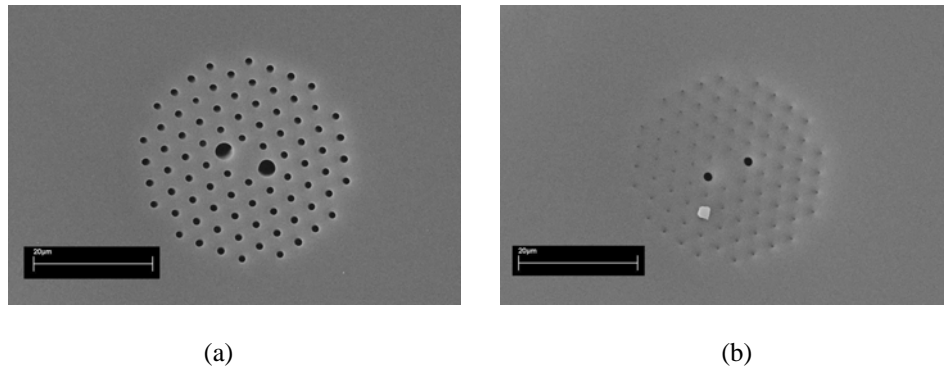


Figure 3.25 End views of the PM-1550-01 with different fusion current when the fusion time was fixed at 0.3 s, the offset was fixed at 50  $\mu\text{m}$ : (a) 12 mA, (b) 13 mA.

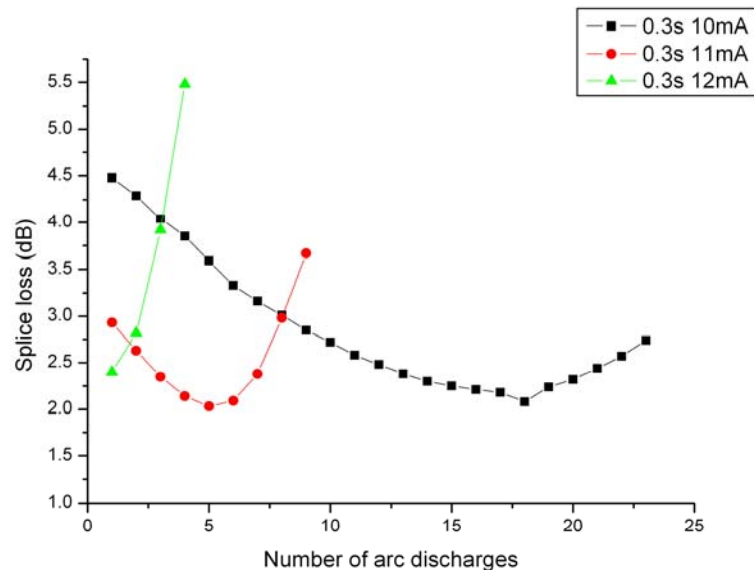


Figure 3.26 The splice losses of SMF-28/PM-1550-01 as a function of the number of arc discharges with fusion current as a parameter. The fusion time, offset and overlap are respectively 0.3s, 50  $\mu\text{m}$  and 5  $\mu\text{m}$ .

Fig. 3.25 shows the end views of PCF-1550-01 when the fusion currents are 12 mA and 13 mA. So the expanded mode field in two perpendicular transverse directions will more different, which will limit the improvement of the coupling efficiency between PM-1550-01 and SMF-28 when repeated weak arc discharges are applied. For splicing SMF-28/PM-1550-01 (Fig. 3.26), when the fusion currents were 10 mA and 11 mA, the minimum splice loss of 2.08 dB and 2.03 dB were obtained after 18 and 5 discharges, respectively. The splice loss from PM-1550-01 to SMF-28 in the same condition was about 1.80 dB, which is almost splice reciprocity. When the fusion current was 12 mA, the minimum splice loss was 2.41 dB after the first discharge; further discharges increased the splice loss. The structure of the splicing joint when the loss is 2.03 dB is shown in Fig. 3.27. We can observe that the air holes collapse gradually toward the splicing interface, as we expected. When we set overlap 5  $\mu\text{m}$ , five splices were done when the fusion current was 11 mA that yielded an average splice loss of 2.22 dB with a standard deviation of 0.22 dB, and the splicing joint can be bent in a circle of about 1.5 cm before breaking. The splice loss decreased significantly compared with the splice loss when butt-coupled. However, the experimental loss of SMF-28/PM-1550-01 was larger than that of SMF-28/LMA-5. This is because the mode field shape difference between PM-1550-01 and SMF-28 will lead to extra loss in addition to the transition loss.

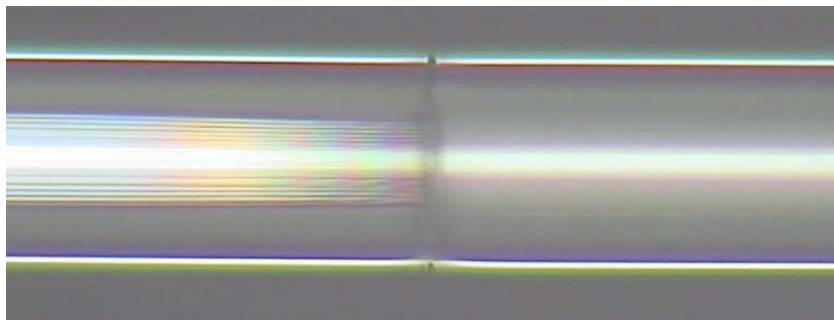


Figure 3.27 Optical microscopy image of the fusion joint of PM-1550-01/SMF-28 with the splice loss 2.03 dB.

### 3.6 Summary

In conclusion, we have investigated the micro-hole collapse property of five different kinds of PCFs by observing the side views of PCFs using optical microscopy and the end views of PCFs using scanning electron microscopy after splicing. The physical mechanism of the splice loss was studied in detail and then different methods were proposed according to the different structure of PCFs to achieve low-loss splicing. A precise alignment and proper heat energy being applied to the joint of PCF/SMF is the key in achieving low-loss splicing, so changing the fusion current or changing the fusion time in a suitable range can lead to optimum results. For the splicing between PCFs, and between the PCF and the SMF having similar MFDs, low-loss splicing can be achieved by minimizing the collapse of air holes of the PCF. For the small-core PCF with low air-filling fraction, including the PM-PCF, low-loss splicing can be achieved by applying repeated arc discharges over the splicing joint to gradually collapse the air holes of the small-core PCF. For the small-core PCF with high air-filling fraction, an intermediate fiber should be used to decrease the splice loss. We have demonstrated the low-loss splice of these different PCFs with conventional SMFs. The optimized splice results and splice parameters are listed in Table 2 and Table 3 respectively. We believe the results can be further improved by using a fusion splicer which has higher precision in alignment and in controlling fusion energy. The experimental results prove that fusion splicing is a simple and practical solution to solve the coupling problem between PCFs and SMFs, which will benefit the development of different PCF devices and sensors for practical applications.

Table 2. Comparison of connection losses from SMF to different PCFs

Splice type	Theoretical estimation loss (dB)	Butt-coupling loss (dB)	Optimized splice loss (dB)
SMF-28/LMA-10	0.18	0.41	0.19
SMF-28/HC-1550-02	0.46	1.50	1.45
SMF-28/LMA-5	3.32	3.62	0.90
SMF-28/NL-3.3-880	7.85	8.14	2.53
SMF-28/PM-1550-01	4.70	4.88	2.03

Table 3. The optimized parameters of splicing SMF28 to different fibers

Splice parameters	Fiber				
	SMF-28	LMA-10	HC-1550-02	LMA-5	PM-1550-01
Prefusion time	0.2 s				
Prefusion current	10 mA	5 mA	5 mA	5 mA	5 mA
Gap	50 $\mu$ m				
Overlap	10 $\mu$ m	5 $\mu$ m	10 $\mu$ m	3 $\mu$ m	5 $\mu$ m
Fusion time one	0.3 s	0	0	0	0
Fusion current one	10.5 mA	—	—	—	—
fusion time two	2.0 s	0.3 s	0.3 s	0.3 s	0.3 s
fusion current two	16.3 mA	12 mA	9 mA	10 mA	11 mA
fusion time three	2.0 s	0	0	0	0
fusion current three	12.5 mA	—	—	—	—
Center position	255	205	205	205	205
Number of repeated discharges	—	—	—	13	5

### References for Chapter 3

1. P. J. Bennett, T. M. Monro, and D. J. Richardson, "Toward practical holey fiber technology: fabrication, splicing, modeling, and characterization," *Opt. Lett.*, vol. 24, pp. 1203-1205, (1999).
2. J. T. Lizier, and G. E. Town, "Splice losses in holey optical fibers," *Photon. Technol. Lett.*, vol. 13, pp. 794-796, (2001).
3. Y. L. Hoo, W. Jin, J. Ju, and H. L. Ho, "Loss analysis of single-mode fiber/photonic-crystal fiber splice," *Microw. Opt. Tech. Lett.*, vol. 40, pp. 378-380, (2004).
4. C. Kerbage, A. Hale, A. Yablon, R. S. Windeler, and B. J. Eggleton, "Integrated all-fiber variable attenuator based on hybrid microstructure fiber," *Appl. Phys. Lett.*, vol. 79, pp. 3191-3193, (2001).
5. K. Nakajima, K. Hogari, J. Zhou, K. Tajima, and I. Sankawa, "Hole-assisted fiber design for small bending and splice losses," *Photon. Technol. Lett.*, vol. 15, pp. 1737-1739, (2003).
6. Y. Bing, K. Ohsono, Y. Kurosawa, T. Kumagai, M. Tachikura, "Low-loss holey fiber," *Hitachi Cable Review*, vol. 24, pp. 1-5, (2005).
7. B. Bourliaguet, C. Paré, F. Émond, A. Croteau, A. Proulx, R. Vallée, "Microstructured fiber splicing," *Opt. Express*, vol. 11, pp. 3412-3417, (2003).
8. B. H. Park, J. Kim, U. C. Paek, B. H. Lee, "The optimum fusion splicing conditions for a large mode area photonic crystal fiber," *IEICE Trans. Electron.*, vol. E88-C, pp. 883-888, (2005).
9. J. H. Chong, and M. K. Rao, "Development of a system for laser splicing

- photonic crystal fiber,” *Opt. Express*, vol. 11, pp. 1365-1370, (2003).
10. J. H. Chong, M. K. Rao, Y. Zhu, and P. Shum, “An effective splicing method on photonic crystal fiber using CO<sub>2</sub> laser,” *Photon. Technol. Lett.*, vol. 15, pp. 942-944, (2003).
  11. A. D. Yablon, and R. T. Bise, “Low-loss high-strength microstructured fiber fusion splices using grin fiber lenses,” *Photon. Technol. Lett.*, vol. 17, pp. 118-120, (2005).
  12. F. Benabid, F. Couny, J. C. Knight, T. A. Birks and P. Russell, “Compact, stable and efficient all-fiber gas cells using hollow-core photonic crystal fibers,” *Nature*, vol. 434, pp. 488-491, (2005).
  13. T. P. Hansen, J. Broeng, C. Jakobsen, G. Vienne, H. R. Simonsen, M. D. Nielsen, P. M. W. Skovgaard, J. R. Folkenberg, and A. Bjarklev, “Air-guiding photonic bandgap fibers: spectral properties, macrobending loss, and practical handling,” *J. Lightwave Technol.*, vol. 22, pp. 11-15, (2004).
  14. R. Thapa, K. Knabe, K. L. Corwin, and B. R. Washburn, “Arc fusion splicing of hollow-core photonic bandgap fibers for gas-filled fiber cells,” *Opt. Express*, vol. 14, pp. 9576-9583, (2006).
  15. J. K. Chandalia, B. J. Eggleton, R. S. Windeler, S. G. Kosinski, X. Liu and C. Xu, “Adiabatic coupling in tapered air-silica microstructured optical fiber,” *Photon. Technol. Lett.*, vol. 13, pp. 52-54, (2001).
  16. W. Wadsworth, A. Witkowska, S. Leon-Saval, and T. Birks, “Hole inflation and tapering of stock photonic crystal fibres,” *Opt. Express*, vol. 13, pp. 6541-6549, (2005).
  17. S. G. Leon-Saval, T. A. Birks, N. Y. Joly, A. K. George, W. J. Wadsworth, G. Kakarantzas, and P. Russell, “Splice-free interfacing of photonic crystal fibers,”

- Opt. Lett.*, vol. 30, pp. 1629-1631, (2005).
18. A. D. Yablon, *Optical fiber fusion splicing*, Springer-Verlag press, Heidelberg, Germany, 2005.
  19. J. C. Fajardo, M. T. Gallagher, and Q. Wu, "Splice joint and process for joining a microstructured optical fiber and a conventional optical fiber," *US Patent* 20030081915A1.
  20. O. Frazão, J. P. Carvalho, and H. M. Salgado, "Low-loss splice in a microstructured fibre using a conventional fusion splicer," *Microw. Opt. Tech. Lett.*, vol. 46, pp. 172-174, (2005).
  21. J. Lægsgaard and A. Bjarklev, "Reduction of coupling loss to photonic crystal fibers by controlled hole collapse: a numerical study," *Opt. Commun.*, vol. 237, pp. 431-435, (2004).
  22. M. Koshiba, "Full-vector analysis of photonic crystal fibers using the finite element method," *IEICE Trans. Electron.*, vol. E85-C, pp. 881-888, (2002).
  23. K. Saitoh and M. Koshiba, "Numerical modeling of photonic crystal fibers," *J. Lightwave Technol.*, vol. 23, pp. 3580-3580, (2005).
  24. H. Y. Tam, "Simple fusion splicing technique for reducing splice loss between standard single mode fibres and erbium-doped fibre," *Electron. Lett.*, vol. 27, pp. 1597-1599, (1991).

## Chapter 4

### Microtips for optical coupling to PCFs

#### 4.1 Introduction

Fusion splicing provides a simple and practical way for low-loss connection of PCFs with SMFs. Important advantages of fusion splicing over free-space-coupling include robust alignment, lower reflectance and ultra-compactness; moreover, fusion splicing creates a hermetical seal at the ends of PCFs which prevents moisture or other contaminants from entering the holes, and fusion splicing offers an all-glass optical path that is robust during high power operation [1]. However, in some applications such as gas or liquid sensing using PCFs [2-5], it is preferred to use free-space-coupling to keep the holes of PCFs open to allow efficient gas diffusion from environment into the hole-columns. Free-space coupling requires the use and alignment of lenses to achieve good coupling efficiency. The experimental coupling efficiency of small-core PCFs is generally about 50% using conventional bulky lens system [6, 7], which makes the fiber connection bulky and expensive in practical applications. In this chapter, we demonstrate the use of a photopolymer micro-tip directly grown on a SMF to achieve efficient coupling between small-core PCFs and SMFs, while still keeping the holes of the PCFs open, which can allow

gas species to get into the hole-columns. This compact and efficient butt-coupling method is particularly suitable for PCF gas sensor applications.

## 4.2 Method of fabricating photopolymer microtips

Bachelot et al. [8, 9] first introduced the method of self-growing photopolymer micro-tips at the end of fibers. The photopolymerizable formulation is made of three basic components: a sensitizer dye, an amine cosynergist, and a multifunctional acrylate monomer. As shown in Fig. 4.1, eosin Y (2', 4', 5', 7'-tetrabromofluorescein disodium salt) is used as the sensitizer dye; methyldiethanolamine (MDEA) is used as the cosynergist; and pentaerythritol triacrylate (PETIA) is used as the multifunctional acrylate monomer, which forms the backbone of the polymer network. The formulation system is developed mainly because of its high sensitivity in the spectral region from 450 nm to 550 nm (maximum at 530 nm), which is particularly suitable for argon laser (514 nm) and green He-Ne laser (543.5 nm). In addition, this liquid system is very flexible, which makes it possible to modify the components independently to adjust the physical and chemical properties of the formulation, such as viscosity, spectral sensitivity, and polymerization threshold energy and so on; and the liquid formulation can be washed out easily with a solvent such as methanol or ethanol.

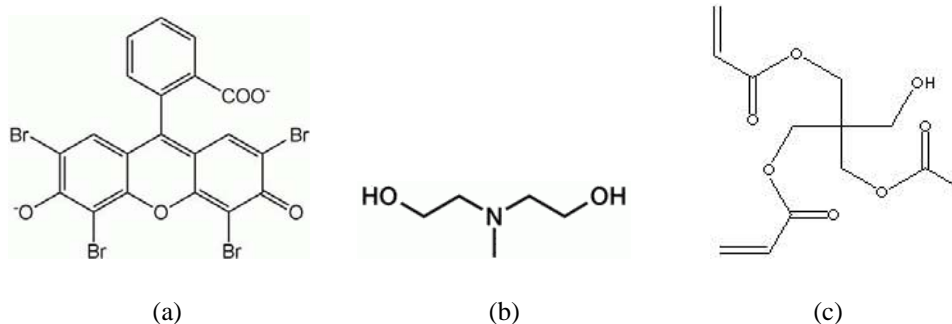


Figure 4.1 Chemical structures of (a) eosin Y, (b) methyldiethanolamine, and (c) pentaerythritol triacrylate.

The liquid formulation is a mixture containing 0.5% in weight of eosin Y, 8% in weight of MDEA and 91.5% in weight of PETIA. The principle of the photopolymerizable formulation can be simply described as follows [9-12]: after the actinic light is absorbed by eosin, the triplet state of the dye reacts with the amine to form radicals. Radicals initiate the polymerization of the monomer. Because of the monomer's multifunctionality, the polymer quickly develops into a three dimensional network. The sensitivity of the liquid system is characterized by a curve that shows the degree of cross-linking as a function of the received energy. The curve is showed in Fig. 4.2 [9]; it corresponds to the typical behavior of a formulation that can be polymerized following a radical process.

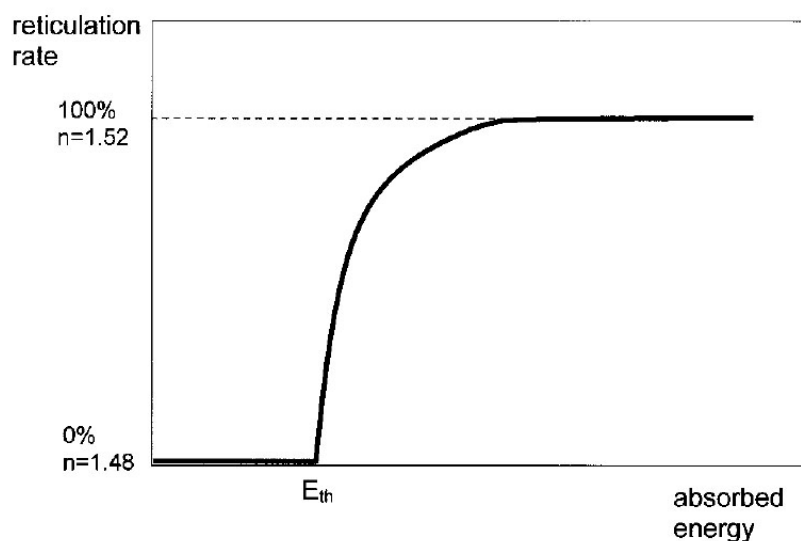


Figure 4.2 Reticulation rate of the formulation plotted versus the absorbed energy.  $E_{th}$  is the threshold energy (when it is achieved polymerization starts), and  $n$  is the refractive index of the formulation [9].

The polymerization starts only when the absorbed energy is greater than a threshold value  $E_{th}$ . Typically, this threshold energy is about  $100 \text{ mJ/cm}^2$  when the  $\text{O}_2$  diffusion process within the formulation is neglected. In contrast, when  $\text{O}_2$

diffused into the liquid can not be neglected, the inhibition process arises from the sensitivity of the initiating radicals to oxygen. The triplet state of the dye is readily deactivated by oxygen either through a physical process or through a chemical reaction. Hence, as long as some quencher remains present in the formulation, this reaction is predominant and no radical forms. Radical formation becomes the predominant channel of triplet decay when the residual oxygen concentration is less than approximately  $10^{-5}$  M. In this case polymer chains start growing, and the cross-linking reaction proceeds rapidly. The optical refractive index of this formulation varies as a function of the degree of cross-linking from 1.48 (0% cross-linking) to 1.52 (100% cross-linking). Hence, as soon as the formulation is polymerized, it will act as an optical waveguide with the core as the polymerized area and the cladding as the surrounding un-polymerized material, which will prevent the light from diverging.

After introducing the principle of the polymerization of the liquid formulation, we demonstrate our micro-tip fabrication process. As shown in Fig. 4.3, a drop of liquid formulation was firstly deposited at the end part of a SMF, as shown in Fig. 4.3(a) on the fiber on the right hand side; a freshly cleaved second SMF that was prepared to grow the tip was then aligned and moved to touch the drop (Fig. 4.3(b)); the fiber was then moved away and a convex-shape liquid was deposited at the end face of the fiber because of liquid surface tension (Fig. 4.3(c)). The height of the droplet is about 30  $\mu\text{m}$ , and the shape of the droplet fabricated with this method has good reproducibility. A green He-Ne laser with wavelength 543.5 nm was then coupled from the other end of the fiber and laser light interacted with the liquid at the end face. As a consequence of polymerization, a tip grew from the core of the SMF within the liquid, as shown in Fig. 4.3(d). After exposure, the part of the liquid

which did not interact with laser light (i.e. the liquid which covered the cladding part of the fiber and which therefore did not polymerize) was washed off by a few drops of ethanol and a robust micro-tip was integrated at the end face of the SMF, as shown in Fig. 4.3(e).

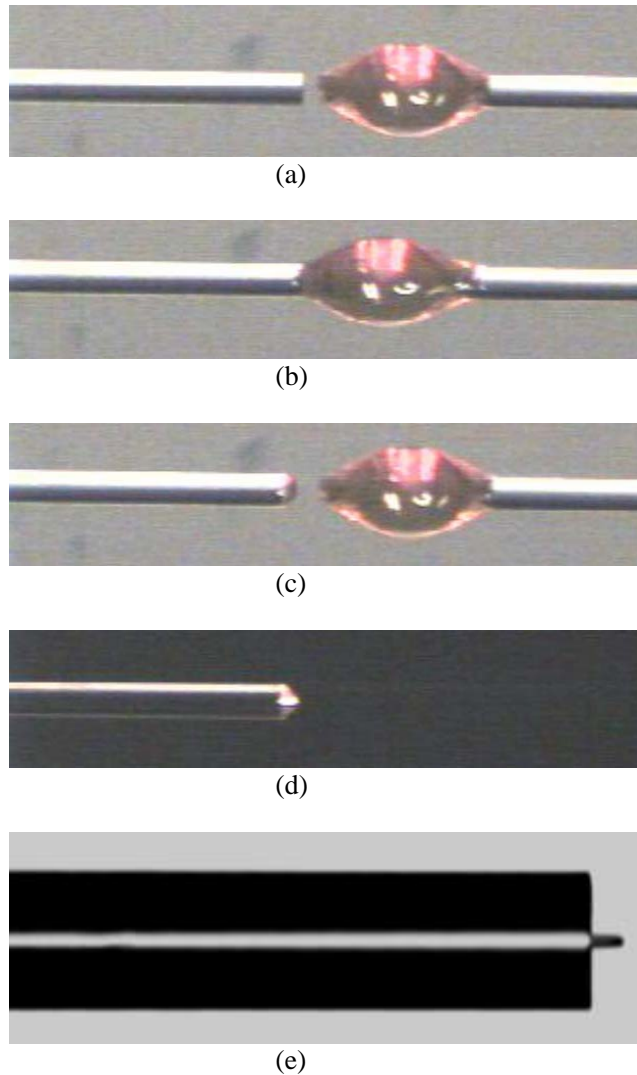


Figure 4.3 Images of the photopolymer micro-tip fabrication process: (a) a drop of liquid formulation is deposited at the end part of a SMF which is aligned with a freshly cleaved SMF; (b) the left SMF which is prepared to grow the tip is moved to touch the drop; (c) a droplet is deposited at the end face of the left SMF; (d) a green laser with suitable power is coupled from the other end of the left SMF; (e) the liquid which is not polymerized is washed off by a few drops of ethanol.

### 4.3 Controllable shape of microtips

The advantages of this micro-tip fabrication method are its simplicity, controllability, reproducibility and being inexpensive. The shape of the micro-tip can be controlled by adjusting the green laser power, exposure time, liquid shape of deposition and oxygen diffusion concentration. Bachelot et al. [8] reported that they used the photopolymer micro-tips as micro-lenses to collect the light from semiconductor lasers into single mode fibers so that efficient light coupling is achieved. The tip's radius of curvature can be optimized by controlling the exposure time when the laser power is kept low. However, the authors did not pay much attention to the effect of the laser power and the exposure time on the size of the tip, which is important for applications such as light coupling from a SMF to a small core PCF, where a micro-tip with a flat end of suitable size is preferred to achieve the best mode match.

Here, we investigated the effect of laser power on the size of the tip growing at the end of SMF fiber and find the suitable tip to best match the small-core PCF. The SMFs used in our experiments are SMF-28 from Corning. As the SMF-28 fiber is multi-mode at the green light wavelength, we applied mechanical stress to attenuate the higher order modes to only allow the fundamental mode to reach the micro-tip. The laser power from the fiber was detected before depositing the liquid. When the power is in the level of several microwatts, e.g., 3  $\mu\text{W}$ , the end of the tip is very small and the radius of curvature is very sensitive to the exposure time [8, 9]. When the power is above the level of 15  $\mu\text{W}$ , the tip's radius of curvature becomes flat in a very short time, which can be explained by the polymerization threshold at the air-formulation boundary. The oxygen diffusion concentration at the interface boundary is higher than that inside the liquid formulation, hence more energy is

needed for polymerization. When the laser power is lower than the polymerization threshold at the air-formulation boundary, the shape of the micro-tip is sensitive to the exposure time. When the laser power is higher than the polymerization threshold at the air-formulation boundary, the tip's end will be flat in a very short time.

Fig. 4.4 shows two examples of the fabricated micro-tips in a low green laser power. When the laser power is  $3 \mu\text{W}$  and the exposure time is 3s, the radius of curvature is  $0.7 \mu\text{m}$  (Fig. 4.4(a)), the radius of curvature can be optimized by controlling exposure time and thus the microtips can be used as micro-lenses to efficiently collect light into the fibers from semiconductor laser [8]. When the laser power is  $3 \mu\text{W}$  and the exposure time is 60s, the micro-tip's end is flat, and the diameter of the tip at its base is  $11.43 \mu\text{m}$  and decreases gradually to  $2.85 \mu\text{m}$  at the end of the tip of polymer protrusion over  $32 \mu\text{m}$  length (Fig. 4.4(b)). From the dimension of the tip's base, it should be deduced that it is not really single mode at the wavelength  $543.5 \text{ nm}$  although we applied mechanical stress to attenuate the high order modes. We will use this flat microtip to couple light from a SMF to a small-core PCF in the next section.

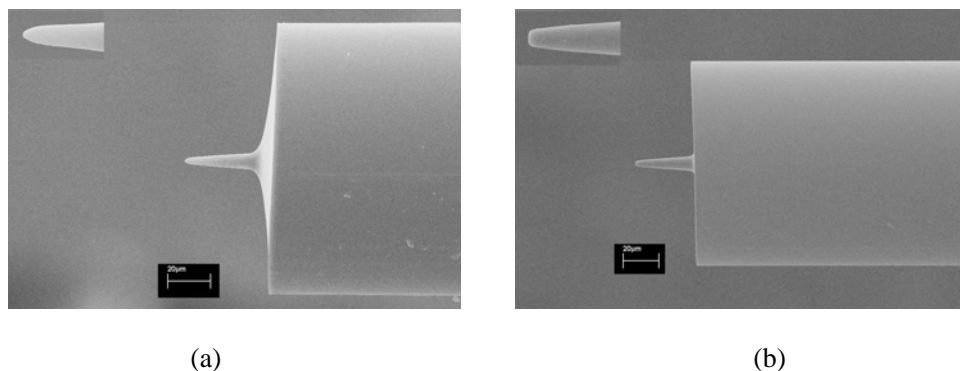


Figure 4.4 SEM images of the photopolymer micro-tips fabricated with low power green laser and various exposure times, the inserts are the close-up pictures of the end of the micro-tips. (a)  $3 \mu\text{W}$ , 3 s; (b)  $3 \mu\text{W}$ , 60 s.

Figure 4.5 shows two examples of the fabricated micro-tips in a relatively high

laser power. When the laser power is  $15\ \mu\text{W}$  and the exposure time is 3s, the diameter of the tip decreases gradually from  $11.71\ \mu\text{m}$  to  $5.71\ \mu\text{m}$  over  $29\ \mu\text{m}$  length (Fig. 4.5(a)); when the laser power is  $80\ \mu\text{W}$  and the exposure time is 3s, the diameter of the tip decreases gradually from  $14.28\ \mu\text{m}$  to  $8.57\ \mu\text{m}$  over  $25\ \mu\text{m}$  length (Fig. 4.5(b)). We will use the microtip in Fig.4.5(a) to implement coupling experiment from a SMF to a small-core PCF in the next section.

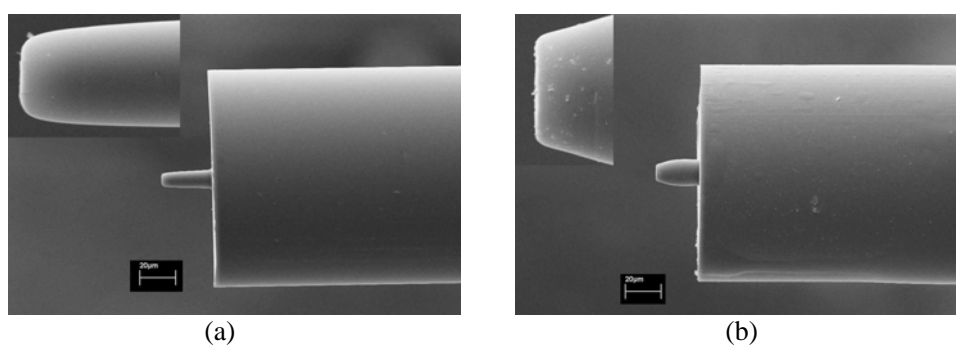


Figure 4.5 SEM images of the photopolymer micro-tips fabricated with different relatively high power green laser, the inserts are the close-up pictures of the end of the micro-tips. (a)  $15\ \mu\text{W}$ , 3 s; (b)  $80\ \mu\text{W}$ , 3 s.

In addition to the laser power energy and exposure time, the shape of microtips can also be controlled by liquid deposition and oxygen concentration. As an example, we can deposit a thin film of liquid formulation at the end of the SMF, instead of a convex-shape formulation. Fig. 4.6 shows two microtips for different deposition shapes when the laser power is  $15\ \mu\text{W}$  and the exposure time is 3s. For the microtip in Fig. 4.6(a), it is formed by convex-shape liquid deposition, as mentioned in section 4.2; for the microtip in Fig. 4.6(b), it is formed by thin film liquid deposition, the length of the microtip can be achieved as short as  $4.3\ \mu\text{m}$ . It proves that the length of the microtip can be flexibly controlled.

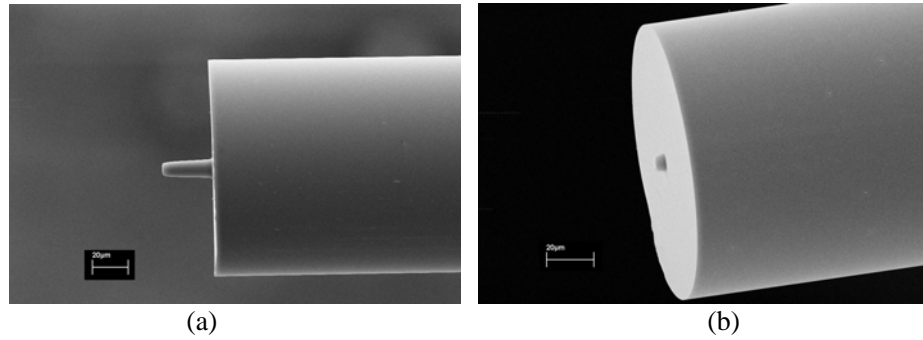


Figure 4.6 SEM images of the photopolymer micro-tips fabricated with a laser power of  $15 \mu\text{W}$  and exposure time of 3 s. (a) convex-shape liquid deposition; (b) thin film liquid deposition.

Because oxygen dissolved within the formulation plays an inhibiting role in the polymerization process, oxygen diffused concentration will affect the shape of the microtips. In the condition of the laser power of  $6 \mu\text{W}$  and the exposure time of 3 s, we fabricated the microtips in different environments: one is in an air atmosphere, the radius of the end of the tip of polymer protrusion is  $1.54 \mu\text{m}$  (Fig. 4.7(a)); the other is in an oxygen chamber, the radius of the end of the tip is  $0.25 \mu\text{m}$  (Fig. 4.7(b)). It demonstrates that the shape of the microtips can be controlled by oxygen diffused concentration. Because the microtip in Fig. 4.7(b) is in the nano-scale, it can be widely used as a probe for optical scanning microscopy [9].

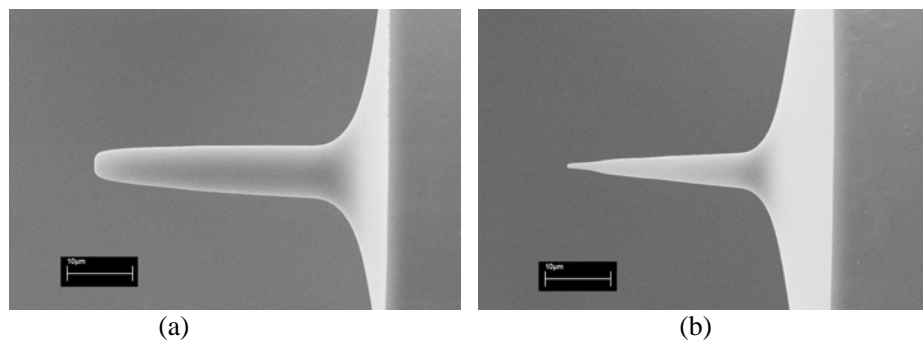


Figure 4.7 SEM images of the photopolymer micro-tips fabricated with a laser power of  $6 \mu\text{W}$  and exposure time of 3 s (a) in an air atmosphere; (b) in an oxygen chamber.

#### 4.4 Low loss coupling between PCFs and SMFs using microtips

After introducing the methods of fabricating microtips and controlling the shape of these microtips, we will use suitable-size microtips to couple light from SMFs to PCFs. The small-core PCFs used in our experiments are NL-3.3-880 and LMA-5 PCFs from Crystal-Fiber A/S, as shown in Fig. 4.8.

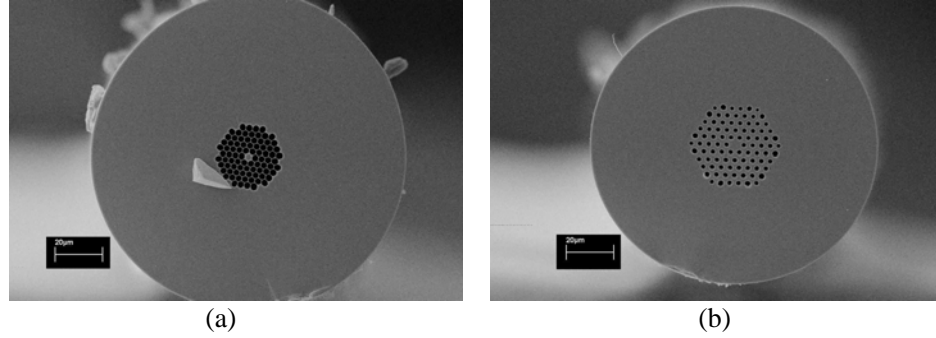


Figure 4.8 SEM images of the cross section of the silica core PCFs used for the experiments. (a) NL-3.3-880, (b) LMA-5.

The NL-3.3-880 PCF has a core diameter of 3.3  $\mu\text{m}$ . The central core is surrounded by a holey lattice of pitch 3.0  $\mu\text{m}$  with an air-filling fraction above 89%. The diameter of outer silica cladding is 138  $\mu\text{m}$ . The MFD of NL-3.3-880 at 1550nm is about 2.2  $\mu\text{m}$  with a numerical aperture (NA) of about 0.41. The LMA-5 PCF has a core diameter of 4.5  $\mu\text{m}$ , a pitch  $\Lambda=2.9$   $\mu\text{m}$  and a relative hole size  $d/\Lambda=0.44$ . The MFD and NA of the LMA-5 PCF are 4.1  $\mu\text{m}$  and 0.23 at 1550nm. The SMFs used in our experiments are SMF-28 from Corning that has a core diameter of 8.3  $\mu\text{m}$ , the core and cladding indices are 1.5362 and 1.5306, and the MFD and NA at 1550nm are about 10.4  $\mu\text{m}$  and 0.14. The butt coupling loss  $\alpha$  between a PCF and a SMF, for optimal alignment, can be estimated by

$$\alpha = -20 \log \left( \frac{2\omega_{PCF}\omega_{SMF}}{\omega_{PCF}^2 + \omega_{SMF}^2} \right) \quad (1)$$

where  $2\omega_{PCF}$  and  $2\omega_{SMF}$  are respectively the MFDs of the PCF and the SMF. The

butt coupling loss for light propagating from SMF-28 to NL-3.3-880 and LMA-5 fibers were experimentally measured at 1550nm and found to be 8.14 dB and 3.62 dB, respectively, which agree well with the theoretical estimation given by Eq.(1), i.e., 7.85 dB and 3.32 dB. The good agreement between the theoretical and the experimental results indicate that the main loss mechanism is due to the poor mode match between the small-core PCFs and the SMFs, as mentioned in Chapter 3. In the following, we will report the use of a photopolymer micro-tip integrated on the end face of a SMF-28 fiber to reduce the MFD and increase the NA of the light beam coming out from the SMF, so that there is a better match to the small MFD and the large NA of small-core PCFs.

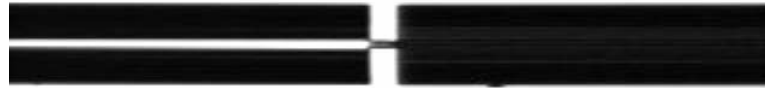
Because the micro-tip is perfectly aligned with the core of the SMF and the length of the tip is short, only the fundamental mode of the 1550  $\mu\text{m}$  light propagates in the SMF and the tip. The theoretical values of MFD and NA of the tip end in Fig. 4.4(b) are respectively about 2.25  $\mu\text{m}$  and 0.40, which approximately match that of the NL-3.3-880 fiber; the theoretical loss due to mode mismatch is estimated to be about 0.07 dB between the tip and this PCF, which is calculated from Eq. (1). The theoretical mode mismatch loss between the SMF and the base of micro-tip is about 0.27 dB. The theoretical values of MFD and NA of the tip in Fig. 4.5(a) are about 4.20  $\mu\text{m}$  and 0.23, which match the MFD and NA of the LMA-5 fiber, and the theoretical mode mismatch loss is calculated to be about 0.003 dB between the tip and the LMA-5 fiber. However, the theoretical mode mismatch loss between the SMF and the base of the micro-tip is about 0.22 dB.

To examine the improvement of coupling efficiency by the use of micro-tips, we conducted the coupling experiment using the alignment platform of a commercial fusion splicer. First, the power of the 1550nm source at the output of a

SMF-28 fiber without a polymer tip was measured, and then the PCF with one end coupled to a power meter was aligned optimally with the SMF-28 fiber to detect the coupling power. The coupling loss thus measured was 8.14 dB when the PCF was NL-3.3-880, and it was 3.62 dB when the PCF was LMA-5. Then the SMF-28 fibers, on which a micro-tip as shown in Fig. 4.4(b) and Fig. 4.5(a) had been grown were spliced, at the non-tipped end with the output fiber of the source, and the tipped-end of the SMF-28 fibers were aligned, in turn, with the the small-core PCFs (NL-3.3-880 and LMA-5) while keeping the PCFs and the power meter untouched. Care was taken to touch the PCF fiber lightly with the tip, otherwise it was possible that the tip may be broken, even though the polymer tip is elastic and strong. Fig. 4 shows the side view of the aligned SMF/NL-3.3-880 and SMF/LMA5 fiber pairs. The coupling loss reduced from 8.14 dB to 2.98 dB for NL-3.3-880 and the coupling loss reduced from 3.62 dB to 1.80 dB for LMA-5. The reduction of the loss is totally from the improvement of mode match because the other experimental conditions are the same. The experimental loss is larger than the theoretically calculated value above because of the unperfected edge of micro-tips, the interface reflection loss between the micro-tip and the SMF, the two end face Fresnel reflection loss of PCFs and the possible misalignment loss. The mechanical strength can be improved by packaging the joint after optimal alignment.



(a)



(b)

Figure 4.9 Optical images of butt-coupling between SMFs integrated with different-size micro-tips and small-core PCFs. (a) Coupling between a SMF with a tip as shown in Fig. 4.4(b) and NL-3.3-880; (b) Coupling between a SMF with a tip as shown in Fig. 4.5(a) and LMA-5.

## 4.5 Summary

In conclusion, we demonstrated the use of photopolymer micro-tip to improve the light coupling efficiency from SMFs to small-core PCFs. By controlling the laser power and exposure time, the shape and the size of the micro-tips can be optimized to match the mode field of the small-core PCFs. Experiments show that the coupling efficiency can be improved by up to 5 dB when compared with direct SMF/PCF joints which do not use the micro-tips. This compact and efficient butt-coupling method is particularly suited for SMF/PCF connections for gas sensor applications where holes in the PCF need to be kept open at the joint for easier access to the evanescent field and this method also may be suitable for connecting a SMF to a PCF with the central hole filled with a liquid sample for liquid sensor applications.

## References for Chapter 4

1. A. D. Yablon, and R. T. Bise, "Low-loss high-strength microstructured fiber fusion splices using grin fiber lenses," *Photon. Technol. Lett.*, vol. 17, pp. 118-120, (2005).
2. T. M. Monro, W. Belardi, K. Furusawa, J. C. Baggett, N. G. R. Broderick, D. J. Richardson, "Sensing with microstructured optical fibres," *Meas. Sci. Technol.*, vol. 12, pp. 854-858, (2001).
3. J. M. Fini, "Microstructure fibres for optical sensing in gases and liquids," *Meas. Sci. Technol.*, vol. 15, pp. 1120-1128, (2004).
4. Y. L. Hoo, W. Jin, H. L. Ho, D. N. Wang, and R. S. Windeler, "Evanescent-wave gas sensing using microstructure fiber," *Opt. Eng.*, vol. 41, pp. 8-9, (2002).
5. Y. L. Hoo, W. Jin, H. L. Ho, J. Ju, and D. N. Wang, "Gas diffusion measurement using hollow-core photonic bandgap fiber," *Sens. Actuators B*, vol. 105, pp. 183-186, (2005).
6. M. Rusu, A. Grudinin, and O. Okhotnikov, "Slicing the supercontinuum radiation generated in photonic crystal fiber using an all-fiber chirped-pulse amplification system," *Opt. Express*, vol. 13, pp. 6390-6400, (2005).
7. A. Aguirre, N. Nishizawa, J. Fujimoto, W. Seitz, M. Lederer, and D. Kopf, "Continuum generation in a novel photonic crystal fiber for ultrahigh resolution optical coherence tomography at 800 nm and 1300 nm," *Opt. Express*, vol. 14, pp. 1145-1160, (2006).
8. R. Bachelot, A. Fares, R. Fikri, D. Barchiesi, G. Lerondel, and P. Royer, "Coupling semiconductor lasers into single-mode optical fibers by use of tips grown by photopolymerization," *Opt. Lett.*, vol. 29, pp. 1971-1973, (2004).

9. R. Bachelot, C. Ecoffet, D. Deloeil, P. Royer, and D. J. Lounnot, "Integration of micrometer-Sized polymer elements at the end of optical fibers by free-radical photopolymerization," *Appl. Opt.*, vol. 40, pp. 5860-5871, (2001).
10. C. Ecoffet, A. Espanet, and D. J. Lounnot, "Photopolymerization by evanescent waves: a new method to obtain nanoparts," *Adv. Mater.*, vol. 10, pp. 411-414, (1998).
11. A. Espanet, C. Ecoffet, and D. J. Lounnot, "PEW: photopolymerization by evanescent wave II: revealing dramatic inhibiting effects of oxygen at submicrometer scale," *J. Polym. Sci. A: Polym. Chem.*, vol. 3, pp. 2075–2085, (1999).
12. M. Hocine, N. Fressengeas, G. Kugel, C. Carré, D. J. Lounnot, R. Bachelot, and P. Royer, "Modeling the growth of a polymer microtip on an optical fiber end," *J. Opt. Soc. Am. B*, vol. 23, pp. 611-620, (2006).

## Chapter 5

### Fabrication of selective injection PCFs

#### 5.1 Introduction

PCFs with their holes filled with gas or liquid have been actively studied for a number of years. The applications of these fibers include tunable fiber optic devices [1-5], laser sources [6, 7] and waveguide sensors [8-11]. Most of the PCF sensors studied previously have solid cores and exploit the interaction of light with samples through evanescent field extended into the air holes [8-10]. The air holes also act as channels to confine gas or liquid samples. The advantages of PCF sensors, compared with other evanescent wave sensors, include long interaction length which improves the sensitivity, and the robust structure without needing to remove the fiber cladding and polymer coating [9]. However, evanescent-field sensors have poor light field/sample overlap and hence relatively low sensitivity. Recently, it has been reported that hollow-core PCFs have been used for sensing in gas and liquid [11]. In liquid sensing, the core is formed by a liquid sample and is surrounded by an air-silica microstructured cladding; the filling of liquid into the core turns the photonic bandgap guidance into total internal reflection guidance [11]. This novel design has many key advantages over evanescent-field sensors: near-unity

light/sample overlap over a wide range of wavelength range, and a single mode or a few low-order modes can be propagated in the liquid core if the average air-silica cladding index is just below the index of the liquid. This novel structure not only introduces an effective way for liquid sensing applications, but also opens new perspectives for nonlinear applications by filling various functional materials into the central hole of a PCF.

In practical realization, however, filling only the central core of a hollow-core PCF but not the others is a major challenge [11, 12]. To our knowledge, only a few articles [4, 5, 13-15] reported works on the selective filling of the holes in a PCF. In [4, 5], selective filling of six-hole PCF to achieve tunable birefringence is described. Because the air holes are significant large (about 40  $\mu\text{m}$ ), certain air holes can be sealed with epoxy, so that only open air holes can be filled with polymer. However, this method can not be used in most PCFs because of their relative small holes. In [12], the authors fill the central hollow core by differential filling speed that depends on the size of the air holes. As shown in Fig. 5.1(a), the liquid fills the larger holes much faster than the smaller holes [12], after a given time, the infiltration length within the central hole is longer than that within the cladding holes. So a multi-step injection-cure-cleave process can be used to only fill the central hole with liquid. However, the fabrication process is very complicated, which will limit its applications. In [13], a single-hole hollow-core fiber is spliced to the PCF using a fusion splicer; the single-hole is aligned to the central hole of the PCF and cladding holes are sealed by the solid cladding of the single-hole fiber, as shown in Fig. 5.1(b). In this method, a hollow fiber with a suitable single-hole size is needed and the silica bridge between the central hole and cladding holes of the PCF can't be too thin, which limits this method for widespread applications.

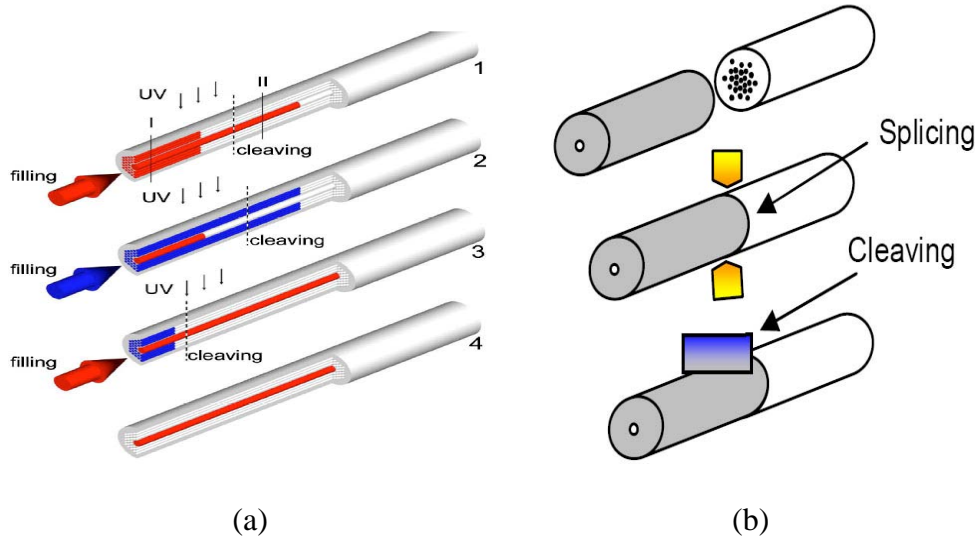


Figure 5.1 (a) Schematic flowchart on selective filling of the PCFs by different filling speed [12]; (b) Schematic of the fabrication process of the end caps to selective filling the central hole of the air-core Fresnel fiber [13].

In [14, 15], the authors mention briefly the use of a fusion splicer to collapse the cladding holes for the fabrication of liquid core PCF but don't give details on the fusion process and how the fusion parameters affect the results. In this chapter, we will report a simple method for selective filling of the central hole. The method uses only a conventional fusion splicer, and by proper selection of fusion parameters, the cladding holes can be closed while the central hole remains open. The effects of fusion current, fusion duration and offset position on the hole collapse property of the PCFs are investigated.

## 5.2 Method of fabrication: micro-hole collapse effect

Figure 5.2 shows a Scanning Electron Microscope (SEM) micrograph of the PCF cross-section. The PCF was purchased from Crystal-Fiber A/S and has a central hole of diameter  $10.9\mu\text{m}$ . The central hole is surrounded by a holey lattice of pitch  $3.8\mu\text{m}$ . The holey cladding region has a diameter of  $70\mu\text{m}$  and is surrounded by a ring of solid silica. The total diameter of the fiber is about  $120\mu\text{m}$ . The thickness of the silica layers between cladding holes is about  $0.36\mu\text{m}$ , and the air-filling fraction

in the holey region is above 90%. This fiber is a good candidate for fabricating a novel liquid-core PCF as discussed in Ref.[11] because the average index of air-silica cladding is sufficiently low to allow the guidance of light in almost any liquid-core through total internal reflection.

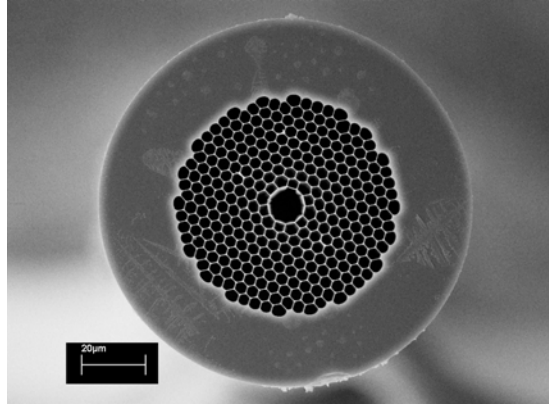


Figure 5.2 SEM image of the cross section of the PCF used for the experiment

In the following, we discuss the use of a conventional fusion splicer to selectively collapse some or all of the holes in the cladding but leave the central-hole remain open. The conventional fusion splicer has been used to splice a PCF to a standard single mode fiber (SMF). In such an operation, an effective approach to achieve low splicing loss is to use an arc of short duration and weak discharge current to avoid or reduce the collapse of the holes of the PCF [16, 17], as discussed in Chapter 3. Here we will give a further detailed investigation on the hole collapse of the hollow-core PCF.

In standard fiber splicing, the electrode axis is positioned at the center-line as shown in Fig. 5.3(a), and the ends of the two fibers are affected equally by the discharge. Since the holes in the end part of a PCF are easy to collapse, if the electrode axis is positioned as shown in Fig. 5.3(b), the arc discharge will affect the end face of a PCF only weakly as compared with the end-face of the solid SMF. We define the “offset” as the distance between the tip of the PCF and the electrode axis.

Such an arrangement avoids the total collapse of the cladding holes and hence reduces the splicing loss. We propose in this chapter to use the offset to selectively control the collapse of the holes at the end-face of a PCF. By removing the standard SMF just before the start of the arc discharge, the end face of the PCF will not be spliced to the SMF and it will only be heated by a weak arc discharge that will cause the collapse of some of the holes.

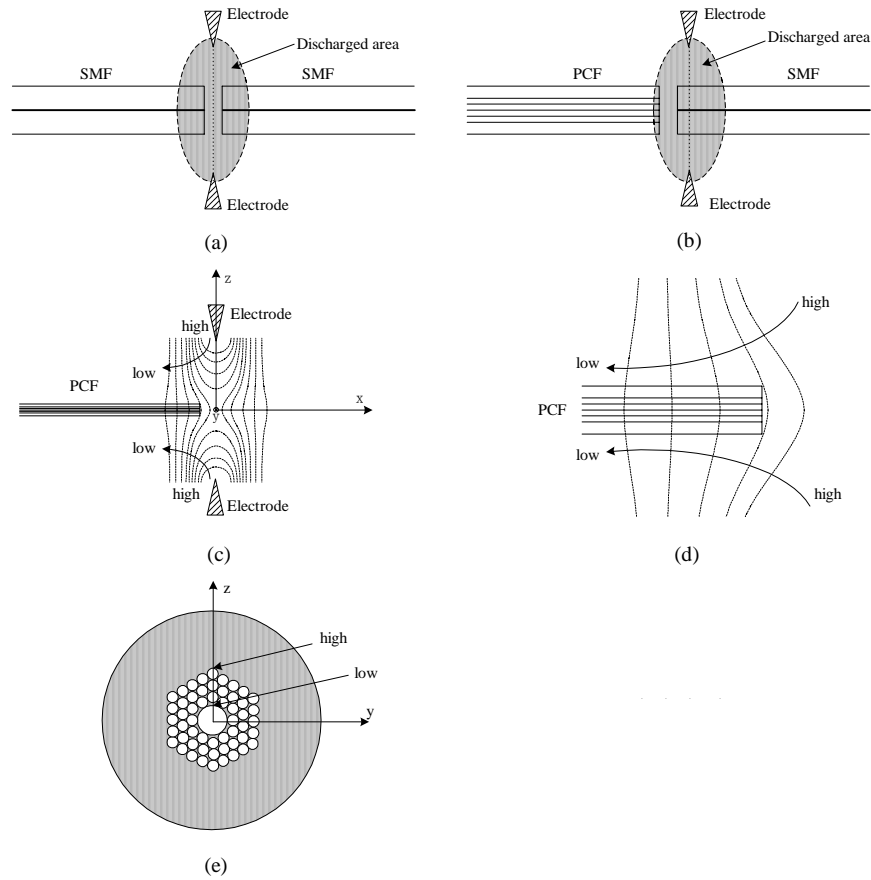


Figure 5.3 The positioning of the electrode axis when (a) two SMFs are to be fusion spliced, (b) a SMF is to be spliced to a PCF, (c) The current and energy density distribution in an arc fusion splicer [18, 19], (d) The close-up of the end part of the PCF in the temperature (energy density) distribution field of Fig. 5.3(c), (e) Illustration of the transverse temperature distribution in the PCF.

The current density between two electrodes is given by [18, 19]

$$i(r, z) = \frac{I_0}{2\pi\sigma^2(z)} \exp\left(-\frac{r^2}{2\sigma^2(z)}\right), \quad (1)$$

where

$$\sigma(z) = \sigma_0(1 + Cz^2)^{-1/3}, \quad r^2 = x^2 + y^2. \quad (2)$$

The coordinates  $x$ ,  $y$  and  $z$  are defined in Fig. 2(c).  $I_0$  is the total current that can be obtained by integrating the current density over all  $r$ .  $\sigma(z)$  is the Gaussian width of the current density at position  $z$ ,  $\sigma_0$  is the Gaussian width of the current density at the midpoint of the electrodes' separation ( $z=0$ ),  $C$  is a constant determined from the variation of the square of the current density in the  $z$  direction. Figure 5.3(c) shows the current density or energy density distribution by contour lines, Fig. 5.3(d) is the close-up of the end part of the PCF in the temperature (energy density) distribution field in Fig. 5.3(c). The energy density changes with the square of the current density and the temperature of the discharge is proportional to the energy density [18, 19]. From Eqs. (1) and (2), we can find the arc discharge is hottest at the electrode tips and the temperature at the midpoint between the electrode tips falls to a minimum along the electrode's axis, hence the temperature distribution of the end face of PCF is that the inner cladding temperature is lower than the outer cladding temperature (Fig. 5.3(d,e)) when the tip of the PCF is not too far from the electrode axis, i.e. when the offset is small. For a standard SMF, the fiber temperature is largely uniform along the fiber radial direction because the thermal conduction time of the solid SMF is very short, only a few milliseconds are required to transfer heat from the hottest spot of the outer surface to the center and other locations within the fiber cross-section and to establish a uniform temperature distribution across the whole cross-section [19]. For the solid silica ring cladding of the PCF, the condition is similar to the solid SMF, so the temperature of the solid ring cladding can be regarded as uniform. However, the heat transfer from the solid silica ring to the center of the holey region is much slower because of the presence of large air-holes

and the relative slow heat transfer in air than in solid silica. Hence it is believed that temperature of the inner cladding holes will keep lower than that of the outer cladding holes during the discharge duration which is typically a few hundreds milliseconds. It is difficult to accurately determine the temperature distribution around the holly region. However, from the data of [18], the temperature decreases by about 200 °C from the point  $z=500 \mu\text{m}$  to the midpoint along the electrode's axis, we may qualitatively estimate the temperature difference between the outer cladding holes and the inner cladding holes at about  $(200^\circ\text{C} / 500 \mu\text{m}) * 35 \mu\text{m} = 14^\circ\text{C}$ . The temperature decreases as a Gaussian function when the offset from the electrode axis increases. From [18], we also know that when the offset is changed by 100  $\mu\text{m}$  under the same fusion current and fusion duration, the temperature changes by about 100°C.

When the temperature of heated fiber exceeds the softening point which is around 1670°C, the surface tension will overcome the viscosity and cause the PCF's cylindrical air holes to begin collapsing. The rate of collapse is given by [17,19]

$$V_{collapse} = \frac{\gamma}{2\eta} \quad (3)$$

where  $\gamma$  is surface tension and  $\eta$  is viscosity. Surface tension of silica is not very sensitive to temperature over the range encountered in splicing; but in contrast, the viscosity of silica decreases sharply with increasing temperature, so the air holes collapse quickly in the high temperature region. Since the temperature at the center of the PCF will be lower as compared to the periphery and also since the smaller hole will close before the bigger hole, the air holes in the cladding will close before the central hole. The combined effect of temperature distribution and hole-size allows for the fabrication of selective injection PCFs by using arc discharge of a

conventional fusion splicer.

### **5.3 Experimental studies of fabrication**

We investigated experimentally the effects of fusion parameters on the collapse of holes of the PCF shown in Fig. 5.2. An Ericsson FSU-975 fusion splicer was used in the experiments. The typical parameters-set for splicing two SMFs and the explanation of the parameters are given in Chapter 3. Here we set the fusion time one and three to zero and varied fusion time two and fusion current two to perform discharge tests and the end-face image of the PCF was taken by a scanning electron microscope. The prefusion current was set to 8.0 mA instead of 10 mA to avoid heat collapse of the holes at the PCF end face. We firstly set the center position to 205 which means the offset distance is 50  $\mu\text{m}$ , and set the overlap to 0  $\mu\text{m}$  to get a precise offset distance of the PCF end-face that was subject to heating by arc discharge; we then varied the fusion time, fusion current, and fusion center position to see the effect of these parameters on the collapse of cladding and central holes. Optimal parameters that correspond to the collapse of the cladding holes with the central hole remaining open were then found and used to fabricate the selective injection of a PCF.

#### **5.3.1 The effect of fusion current**

We varied the fusion current in steps of 0.5 mA, kept the fusion duration constant at 0.3 s, and offset distance constant at 50  $\mu\text{m}$ . In Chapter 3, we observe the micro-hole collapse when the fusion current changes from 9 mA to 11.5 mA, most cladding holes are still partially open. So we continue to increase the fusion current to find the optimized parameters which correspond to the status of collapsing all cladding holes and keeping the central hole open. Fig. 5.4(b, c) shows the end-face of the PCF for two typical discharge conditions. The surface tension makes the PCF's

periphery less sharp and causes the central region to cave in. The detailed hole collapse pictures can be found in Fig.5.5.

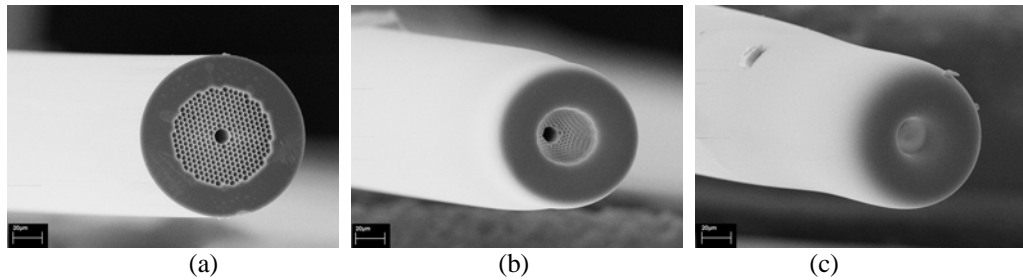


Figure 5.4. End-face of the PCF. (a) without arc discharge; (b) arc current =12.5mA; (c) arc current =14.5mA. The discharge duration and offset distance are kept constant at 0.3 second and 50  $\mu\text{m}$ , respectively.

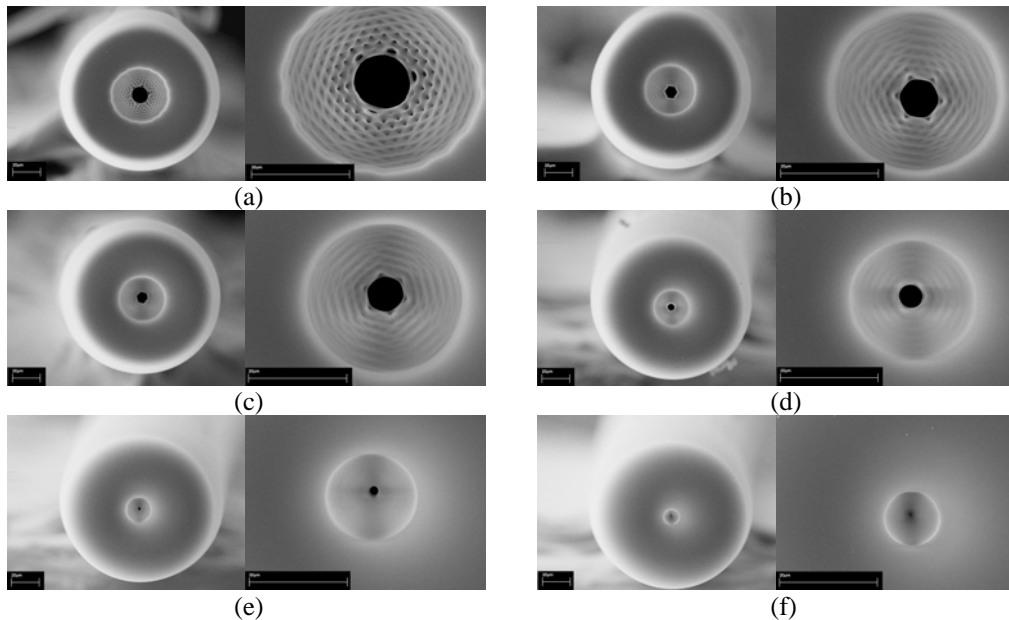


Figure 5.5. End views of the PCF with different arc currents when the arc duration is 0.3 second and the offset distance is 50  $\mu\text{m}$ . The right picture is the close-up of the center part of the left picture. (a) 12.5mA, (b) 13mA, (c) 13.5mA, (d) 14mA, (e) 14.5mA, (f) 15mA.

It can be seen from Fig. 5.5, when arc current is increased, the outer cladding holes collapse and close first when compared to the inner cladding holes. At 12.5 mA, the outer-most holes have already closed but the inner holes are still partially open, as shown in Fig. 5.5(a). From the close-up picture in Fig. 5.5(a), we can find the gradual change of the hole size along the radial direction of the fiber. The

nearer the holes to the center, the less complete will be the holes' collapse. As hole-sizes of the inner and outer claddings are more or less the same (as shown in Fig. 5.2), we believe that the variation in hole collapse along the fiber radial direction is due to a gradual decrease of temperature from the outer solid ring to the central hole. Increasing the temperature by increasing the fusion current enables more holes to collapse within the fusion duration, eventually all the holes in the cladding region close and the central hole can be kept partially open due to the combined effect of lower temperature at and the larger hole size of the central hole. If we continue to increase fusion current, the central hole will shrink and eventually also close. At 13 mA, almost all the cladding holes have closed except the inner six holes that are nearest to the central hollow-core (Fig. 5.5(b)). From Fig. 5.2, we can see that these six holes, due to fabrication imperfection, have slightly bigger sizes than the other six holes surrounding the central-hole. At 13.5 mA (Fig. 5.5(c)), all the holes in the cladding region are closed, although the edge of the central hole is not very smooth. The diameter of the central hole has reduced to about 7.2  $\mu\text{m}$ . When the fusion current reaches 14.0 mA, the collapsed region is very smooth and the central hole's diameter shrinks to about 4.7  $\mu\text{m}$ , as can be seen from Fig. 5.5(d). The diameter of the central hole decreases further at 14.5 mA and finally the hole closes totally (Fig. 5.5(f)) when the current is beyond 15 mA. The experimental observation agrees with the discussion in section 5.2.

### **5.3.2 The effect of fusion duration**

We also evaluated the effect of varying the duration of the arc current when the fusion current and offset distance were kept constant. Fig. 5.6 shows the results for arc current of 13.5 mA and offset distance of 50  $\mu\text{m}$  when the arc duration is varied from 0.3 second to 0.5 second. The central hole shrunk from 7.2  $\mu\text{m}$  to about 4.0  $\mu\text{m}$

when the arc duration was increased from 0.3 s to 0.4 s, and further reduced to about  $2.5\ \mu\text{m}$  when the arc duration increased to 0.5 s. Further increase the arc duration closed all the holes in the center and the cladding. From the discussion in section 2, the outer solid ring cladding will transfer heat to the holey cladding in the fiber radial direction. With the fusion duration increasing, more heat can be transferred to the central hole and the temperature of the central hole increases, so the central hole's size decreases when the fusion duration increases.

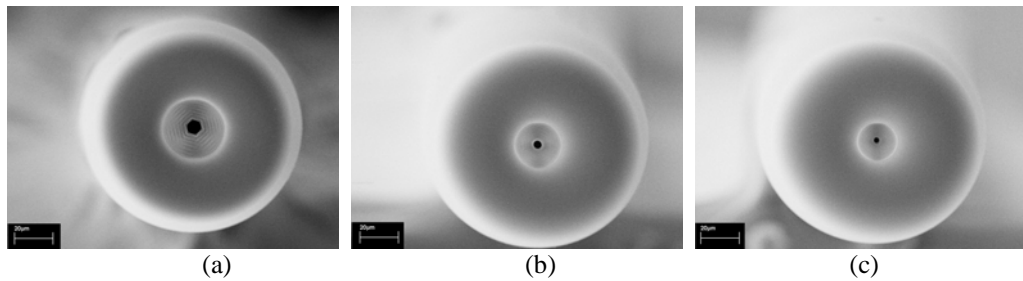


Figure 5.6. End views of the PCF with different arc durations. (a) 0.3 second, (b) 0.4 second, and (c) 0.5 second. The arc current and offset distance are kept constant at 13.5mA and  $50\ \mu\text{m}$ , respectively.

### 5.3.3 The effect of fusion offset

Figure 5.7 shows the SEM micrographs of the PCF end-face for various offset distances, varying from  $50\ \mu\text{m}$  to 0 (no offset). For the cases shown in Fig. 5.7, all the holes in the cladding are closed, and the size of the central hole reduces for smaller offset distance and closes for zero offset. This is because that temperature around the end-face is higher for smaller offset. From the discussion in section 5.2, the temperature increases by about  $10\ ^\circ\text{C}$  when the offset decreases by  $10\ \mu\text{m}$ , so the central hole collapses more quickly in the higher temperature caused by smaller offset.

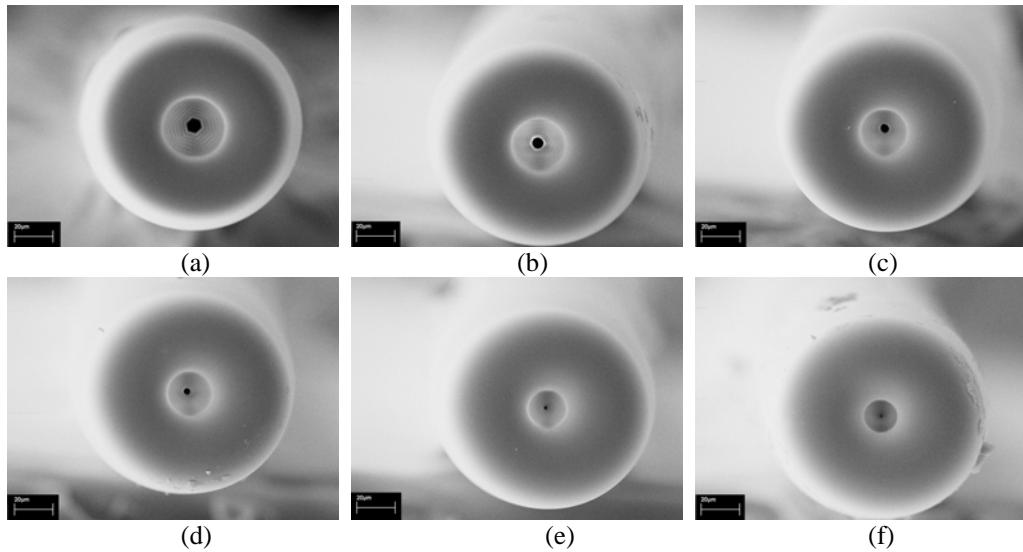


Figure 5.7. End views of the PCF with different offset distances when the arc duration and arc current are fixed at 0.3 second and 13.5mA, respectively. (a) 50 $\mu$ m, (b) 40 $\mu$ m, (c) 30 $\mu$ m, (d) 20 $\mu$ m, (e) 10 $\mu$ m, (f) 0 $\mu$ m.

#### 5.4 Filling the central hole of PCF

To demonstrate the above technique can be used to perform selective filling of the central hole, we used about 15 cm of PCF with cross-section similar to that shown in Fig. 5.1. We firstly treated the two ends of the PCF with an Ericsson FSU-975 fusion splicer with arc duration, fusion current and offset distance set respectively to 0.3 second, 14 mA and 50  $\mu$ m. After thermal treatment, both ends of the PCF were like Fig. 5.5(d), that is, the central hole is still partially open, and all the cladding holes are totally closed. The central hole was then filled with a type of polymer NOA74 by capillary action, the polymer was cured by a UV lamp and the ends of the PCF were cleaved. The two cleaved ends were then examined by using an optical microscope and a scanning electron microscope. The images of one of the ends are shown in Fig. 5.8. The central hole is perfectly filled and the holes in the cladding are not filled. We have thus demonstrated how the hollow core of a PCF can be filled with liquid or gas without filling the cladding holes at the same time. The same results have been obtained with other fusion conditions as given in Fig.

5.5(c) and Fig. 5.5(e). This demonstrates the effectiveness of the method for fabricating selective injection PCFs.

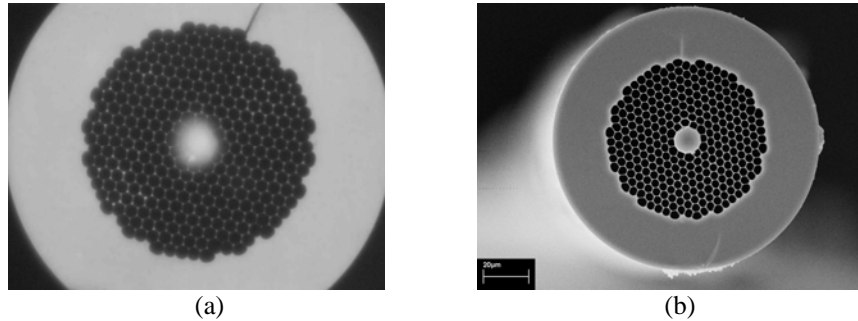


Figure 5.8. (a) Optical microscope image and (b) SEM image of the PCF with the central hole filled with NOA74.

## 5.5 Summary

In conclusion, we have developed a simple method for selective filling the central hole of PCFs. The method is based on a conventional fusion splicer to cause the cladding holes to collapse while leaving the central hollow core to remain open. Theoretical and experimental investigations show that the hole-collapse property of a PCF depends on fusion current, fusion duration and fusion offset position. The opening and closing of the central hole and the holes in the cladding may be controlled to a certain degree by controlling the fusion current, the fusion duration and the fusion offset position. Experiments show that this method can be used to make hybrid polymer/silica PCFs with the central hole filled by a polymer. The quality of the hybrid fiber is good and the fabrication process is highly reproducible. We believe that this method can also be used in other PCFs with different structures by adjusting the fusion parameters. This method can also be used to fabricate a hybrid PCF with a liquid or gas core surrounded by an air-silica microstructured cladding.

## References for Chapter 5

1. P. Domachuk, H. C. Nguyen, B. J. Eggleton, M. Straub, and M. Gu, "Microfluidic tunable photonic band-gap device," *Appl. Phys. Lett.*, vol. 84, pp. 1838-1840, (2004).
2. T. T. Larsen, A. Bjarklev, D.S. Hermann, and J. Broeng, "Optical devices based on liquid crystal photonic bandgap fibres," *Opt. Express*, vol. 11, pp. 2589-2596, (2003).
3. C. Kerbage, R. S. Windeler, B. J. Eggleton, P. Mach, M. Dolinski, and J. A. Rogers, "Tunable devices based on dynamic positioning of micro-fluids in micro-structured optical fiber," *Opt. Commun.*, vol. 204, pp. 179-184, (2002).
4. C. Kerbage, and B. J. Eggleton, "Numerical analysis and experimental design of tunable birefringence in microstructured optical fiber," *Opt. Express*, vol. 10, pp. 246-255, (2002).
5. C. Kerbage, P. Steinvurzel, P. Reyes, P. S. Westbrook, R. S. Windeler, A. Hale, and B. J. Eggleton, "Highly tunable birefringent microstructured optical fiber," *Opt. Lett.*, vol. 27, pp. 842-844, (2002).
6. F. Benabid, F. Couny, J. C. Knight, T. A. Birks, and P. J. Russell, "Compact, stable and efficient all-fibre gas cells using hollow-core photonic crystal fibres," *Nature*, vol. 434, pp. 488-491, (2005).
7. F. Benabid, G. Bouwmans, J. C. Knight, P. J. Russell, and F. Couny, "Ultrahigh efficiency laser wavelength conversion in a gas-filled hollow core photonic crystal fiber by pure stimulated rotational raman scattering in molecular hydrogen," *Phys. Rev. Lett.*, vol. 93,123903, (2004).
8. T. M. Monro, W. Belardi, K. Furusawa, J. C. Baggett, N.G. R. Broderick, and D. J. Richardson, "Sensing with microstructured optical fibres," *Meas. Sci. Technol.*,

- vol. 12, pp. 854-858, (2001).
9. J. B. Jensen, L. H. Pedersen, P. E. Hoiby, L. B. Nielsen, T. P. Hansen, J. R. Folkenberg, J. Riishede, D. Noordegraaf, K. Nielsen, A. Carlsen, and A. Bjarklev, "Photonic crystal fiber based evanescent-wave sensor for detection of biomolecules in aqueous solutions," *Opt. Lett.*, vol. 29, pp. 1974-1976, (2004).
  10. Y. L. Hoo, W. Jin, C. Shi, H. L. Ho, D. N. Wang, S. C. Ruan, "Design and modeling of a photonic crystal fiber gas sensor," *Appl. Opt.*, vol. 42, pp. 3509-3515, (2003).
  11. J. M. Fini, "Microstructure fibres for optical sensing in gases and liquids," *Meas. Sci. Technol.*, vol. 15, pp. 1120-1128, (2004).
  12. Y. Huang, Y. Xu, and A. Yariv, "Fabrication of functional microstructured optical fibers through a selective-filling technique," *Appl. Phys. Lett.*, vol. 85, pp. 5182-5184, (2004).
  13. C. Martelli, J. Canning, K. Lyytikainen, N. Groothoff, "Water-core fresnel fiber," *Opt. Express*, vol. 13, pp. 3890-3895, (2005).
  14. S. Yiou, P. Delaye, A. Rouvie, J. Chinaud, R. Frey, G. Roosen, P. Viale, S. Février, P. Roy, J. Auguste, and J. Blondy, "Stimulated raman scattering in an ethanol core microstructured optical fiber," *Opt. Express*, vol. 13, pp. 4786-4791, (2005).
  15. K. Nielsen, D. Noordegraaf, T. Sørensen, A. Bjarklev, and T. P. Hansen, "Selective filling of photonic crystal fibres," *J. Opt. A: Pure Appl. Opt.*, vol. 7, pp. L13-L20, (2005).
  16. B. Bourliaguet, C. Paré, F. Émond, A. Croteau, A. Proulx, and R. Vallée, "Microstructured fiber splicing," *Opt. Express*, vol. 11, pp. 3412-3417, (2003).
  17. A. D. Yablon, and R. T. Bise, "Low-loss high-strength microstructured fiber

- fusion splices using grin fiber lenses,” *Photonics Technol. Lett.*, vol. 17, pp. 118-120, (2005).
18. M. Tachikura, “Fusion mass-splicing for optical fibers using electric discharges between two pairs of electrodes,” *Appl. Opt.*, vol. 23, pp. 492-498, (1984).
19. A. D. Yablon, *Optical fiber fusion splicing*, Springer-Verlag press, Heidelberg, Germany, 2005.
20. User’s manual for the FSU 975 single fiber fusion splicer by Ericsson.

## Chapter 6

### Hybrid PCFs

#### 6.1 Introduction

As mentioned in Chapter 2, PCFs generally guide light by two different guiding mechanisms: index-guiding [1] or bandgap-guiding [2]. Most PCFs guide light by only one of these two different guiding mechanisms, although hybrid-guiding (combination of index-guiding and bandgap-guiding) has been utilized in photonic crystal slabs [3] for many years. Recently, Cerqueira et al. [4] first demonstrated a hybrid PCF which guided light by both index-guiding and bandgap-guiding simultaneously. This hybrid PCF was composed of air holes and Ge-doped silica rods disposed around an undoped silica core; the air holes were arranged in a hexagonal pattern as in an index-guiding PCF, while the high index rods replaced a single row of air holes along one of the PCF axes. The authors mentioned that this hybrid PCF shared properties of both index-guiding and bandgap-guiding. However, the hybrid PCF is a quite new issue; although Cerqueira et al. proposed a kind of hybrid PCF and gave some basic analysis, it was not a systematic investigation that offers insight into the nature of the hybrid PCF, and many significant properties of hybrid PCFs have not been investigated.

In this Chapter, we propose several hybrid PCF structures and carry out detailed investigations on two kinds of hybrid PCFs. The modal effective index, effective mode area, confinement loss, group velocity dispersion and birefringence are theoretically investigated. The properties of hybrid PCFs are compared with those of the corresponding index-guiding PCF and bandgap-guiding PCF, which gives a physical insight into the guiding mechanism of the hybrid PCFs. Finally, the potential applications of these hybrid PCFs are discussed.

## **6.2 Theory of hybrid PCFs**

### **6.2.1 Description of the approach**

The guiding mechanism of an index-guiding PCF can be simply explained by the effective-index model [5], which is similar to light propagation in a traditional step-index fiber. The guiding mechanism of a bandgap PCF can be predicted by photonic bandgap theory [6], and it also can be explained intuitively by antiresonant reflecting guidance [7]: light at wavelengths satisfying the antiresonant condition is guided in the core by antiresonant reflection from periodically placed high-index rods. Thus we can make an assumption that the light may propagate along the fiber when the light can be confined in the core by index-guiding in one direction and bandgap-guiding in the other direction in the transverse direction, even if the bandgap structure is not a full two dimensional photonic crystal structure.

The structure of a hybrid PCF is a modified PCF structure which is obtained by replacing one or more longitudinal sets of air holes of an air-silica index-guiding PCF by high-index rods as shown in Fig. 6.1, where black holes represent high-index rods and empty holes are air (or low-index) holes. In A1, A2, A3 and A4, air holes are in the majority. In B1, B2, B3 and B4, high-index rods are in majority. Of course there can be many other structures which can be devised by replacing

different lines of hexagonal structure or changing the size of replacing holes/rods, which we do not illustrate in Fig. 6.1. To clearly describe the properties of hybrid PCFs, we focus on investigating two categories of hybrid PCFs, namely A1 and B1.

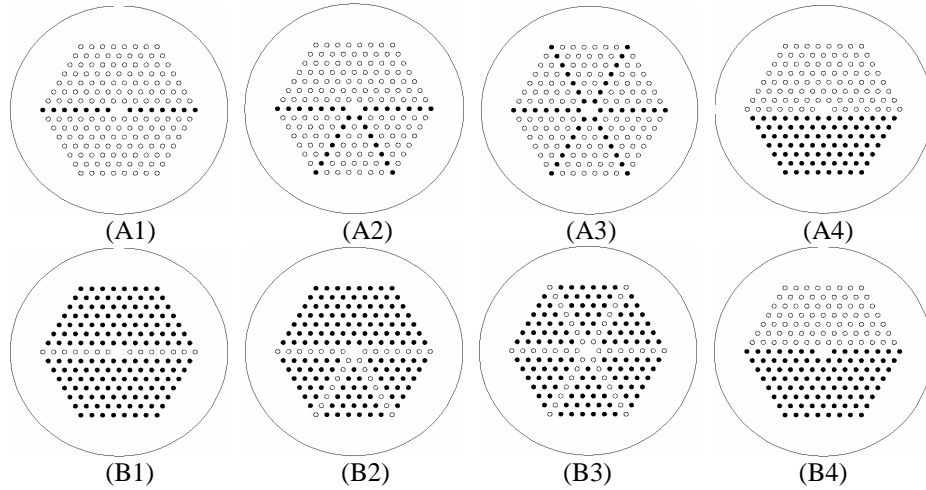


Figure 6.1 Schematics of cross-sections of different structures of hybrid PCFs, whereas black holes are high-index rods, empty holes are air holes.

In order to have a comprehensive understanding of the properties of the hybrid PCFs A1 and B1, it is necessary to investigate the properties of the corresponding index-guiding PCF and bandgap PCF at the same time and compare the properties of the hybrid PCFs with them. In our simulations, the hybrid PCFs A1 and B1 have 7 rings of holes arranged in a hexagonal pattern, the PCFs have a pitch  $\Lambda$  of  $7.5 \mu\text{m}$  and a relative hole size  $d/\Lambda$  of 0.4. We assume that the background silica refractive index is 1.45, and the high-index rod has a refractive index of 1.48.

To analyze PCFs accurately, we use full-vector plane-wave method (PWM) [8] to calculate the bandgap map of the bandgap-guiding PCF and full-vector finite-element method (FEM) [9-11] to model the properties of all PCFs, including index-guiding, bandgap-guiding, hybrid-guiding A1, hybrid-guiding B1. Because of the structure symmetry of these PCFs, one quarter of the fiber cross section is investigated to calculate the modal effective indices in two orthogonal directions [9]. We also model the whole cross section of the fiber, which agrees well with the

results from the quarter cross section. The cladding effective index of the fundamental space-filling mode is calculated by applying the full-vector FEM to an elementary piece of the index-guiding PCF cladding [9]. The effective mode area of a PCF,  $A_{eff}$ , is defined as [10]:

$$A_{eff} = \frac{(\iint_S |E_t|^2 dx dy)^2}{\iint_S |E_t|^4 dx dy} = \pi \omega^2 \quad (1)$$

where  $E_t$  is the transverse electric field vector and  $S$  denotes the whole fiber cross section.  $2\omega$  is mode field diameter (MFD) for a Gaussian shaped mode field distribution. The confinement loss  $L_c$  can be calculated by full-vector FEM with anisotropic perfectly matched layers (PMLs) [11, 12]:

$$L_c = 8.686\alpha \quad (2)$$

where  $\alpha$  is attenuation constant of the complex propagation constant. The unit of  $L_c$  is in decibels per meter. The group velocity dispersion (GVD),  $D_w$ , of a PCF can be deduced from [11]:

$$D_w = -\frac{\lambda}{c} \frac{d^2 n_{eff}}{d\lambda^2} \quad (3)$$

where  $n_{eff}$  is the wavelength dependent effective index,  $\lambda$  is the wavelength, and  $c$  is the velocity of light in vacuum. Material dispersion is neglected [11] in our simulations. The birefringence is defined as:

$$B = \left| n_{eff}^x - n_{eff}^y \right| \quad (4)$$

where  $n_{eff}^x$  and  $n_{eff}^y$  are the effective indices of the fundamental  $E_x$  mode and  $E_y$  mode respectively.

## 6.2.2 Analysis and Discussion

The wavelength range we considered is from 0.55  $\mu\text{m}$  to 2.1  $\mu\text{m}$ . For the index-guiding PCF and bandgap PCF, the fundamental modes of x-polarization and y-polarization are degenerate because of symmetry. However, for the hybrid PCF A1 and B1, the fundamental modes are not degenerate because the guiding mechanisms in two orthogonal directions are different. For hybrid PCFs, we only consider the x-polarized fundamental mode in our simulations because the effective index difference of the two orthogonal fundamental modes is quite small in our cases. The difference will be discussed in section 6.2.2.5.

### **6.2.2.1 Modal effective index**

The light can be guided in the core of the index-guiding PCF when the effective index of the guided mode is larger than the cladding effective index and smaller than the refractive index of the core. For bandgap PCF, only when the modal effective index is within the bandgap regions and smaller than the core index, the light can be guided in the core. According to the resonance theory in Ref. [16], the cut-off wavelengths can be only determined by analyzing an individual high-index rod, which agree well with the bandgap edges predicted by bandgap theory. So we can assume that although the hybrid PCF does not have a full two-dimensional bandgap structure, the bandgap maps can also be approximately suitable for representing the hybrid PCF A1 and B1. The hybrid PCF can guide the light only when the guiding conditions of both index-guiding and bandgap-guiding are satisfied.

As shown in the Fig. 6.2, the green line is the effective index of the fundamental mode of the index-guiding PCF and the red lines represent the effective indices of the bandgap PCF. The cladding line and silica line are the effective indices of the cladding and the core respectively. The solid black lines are the edges of the

bandgap of the bandgap-guiding PCF. We can find from Fig. 6.2 that the light in the whole wavelength range can be well guided in the index-guiding PCF, the effective index decreases gradually with the increase in wavelength. The bandgap PCF has three band gap regions in this range; the guided modes outside the bandgaps are cut off, thus light can propagate in three discrete transmission windows: about 1.26  $\mu\text{m}$  to 2.1  $\mu\text{m}$  in the first gap, 0.76  $\mu\text{m}$  to 1.18  $\mu\text{m}$  in the second gap and 0.55  $\mu\text{m}$  to 0.68  $\mu\text{m}$  in the third gap. The magnitude of the slope of the effective index curve of the bandgap PCF is larger than that of the index-guiding PCF. The crossing points of green line and red line are at the wavelengths about 0.57  $\mu\text{m}$ , 0.91  $\mu\text{m}$ , and 1.79  $\mu\text{m}$ . That means for these wavelengths, the guided modes have the same effective index even if the guiding mechanisms are different.

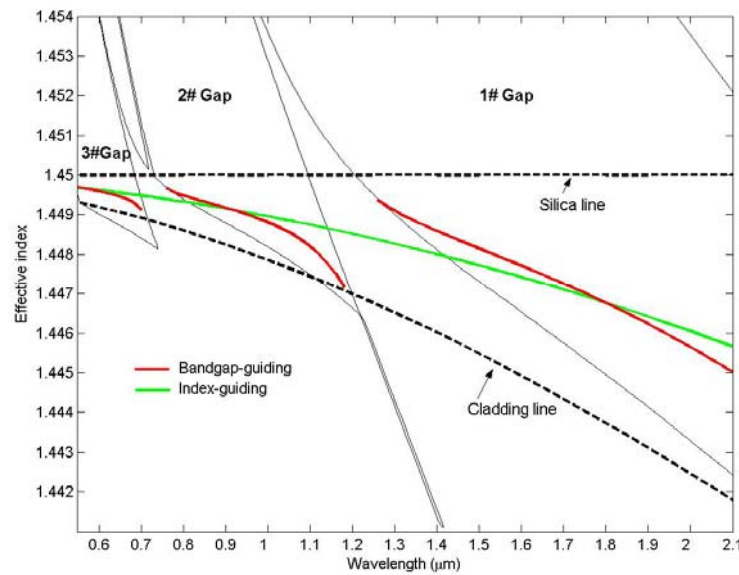


Figure 6.2 Modal effective index of the fundamental modes and bandgap map as a function of wavelength.

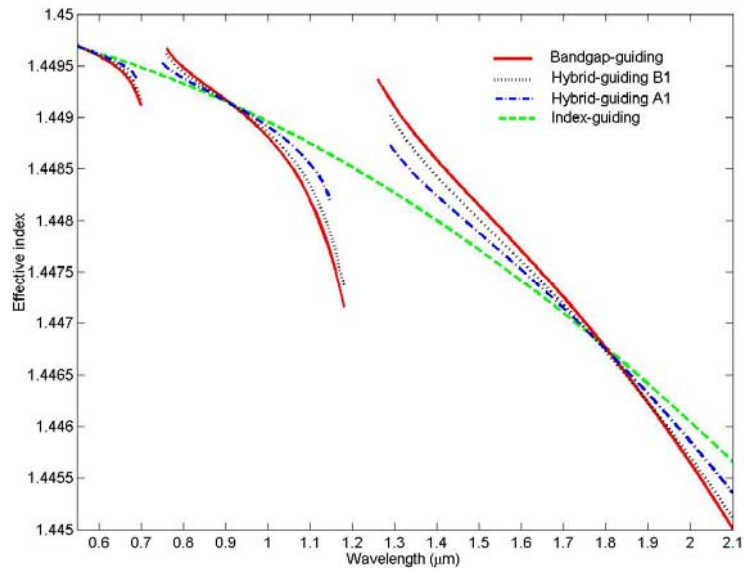


Figure 6.3 Modal effective index of fundamental mode as a function of wavelength. The green dashed line is index-guiding PCF; the red solid line is bandgap PCF; the blue dash-dot line is hybrid PCF A1 and the black dotted line is hybrid PCF B1.

The modal effective index of the hybrid PCFs A1 and B1 are shown in Fig. 6.3. We can find that the effective indices of hybrid PCFs are between the effective indices of the index-guiding PCF and bandgap PCF, and the hybrid PCF has the property of discrete frequency bands. This can be explained by the nature of hybrid-guiding. The hybrid PCF A1 confines light by bandgap effect in x direction and the hybrid PCF B1 confines light by bandgap effect in the cross-section except x direction. So the hybrid PCF should have properties of bandgap-guiding. The effective index curves of the hybrid PCF A1 are closer to the curve of index-guiding PCF compared with hybrid PCF B1, and the effective index curves of hybrid PCF B1 are closer to the curve of bandgap PCF. This is because the index-guiding is the main guiding mechanism in hybrid PCF A1 and bandgap-guiding is the main guiding mechanism according to their refractive index distribution in the cross-section. The cross points of the curves of the four PCFs in Fig. 6.3 correspond to almost the same wavelengths as the cross points of index-guiding PCF and

bandgap PCF shown in Fig. 6.2. That means if the effective index of index-guiding PCF and bandgap PCF is equivalent for one wavelength, the effective index of hybrid guiding PCF will have the same value at that wavelength, which proves again that the hybrid PCF guides light by a combination of both index-guiding and bandgap-guiding. It should be mentioned that in Ref. [4], the effective index curve of the hybrid PCF based on the preform A has an overlap with the curve of the index-guiding PCF for a range of wavelengths, that is because the refractive index of the high-index rod is a gradual variation, which cause the modal effective index of bandgap PCF to have an overlap with the index-guiding PCF, thus causing the overlap with the hybrid PCF.

### 6.2.2.2 Effective mode area

Effective mode area is an important parameter in investigating the modal properties; it has relevance to nonlinearity, confinement loss, bending loss, splicing loss and numerical aperture [13]. Fig. 6.4 shows the normalized effective mode area of different PCFs.

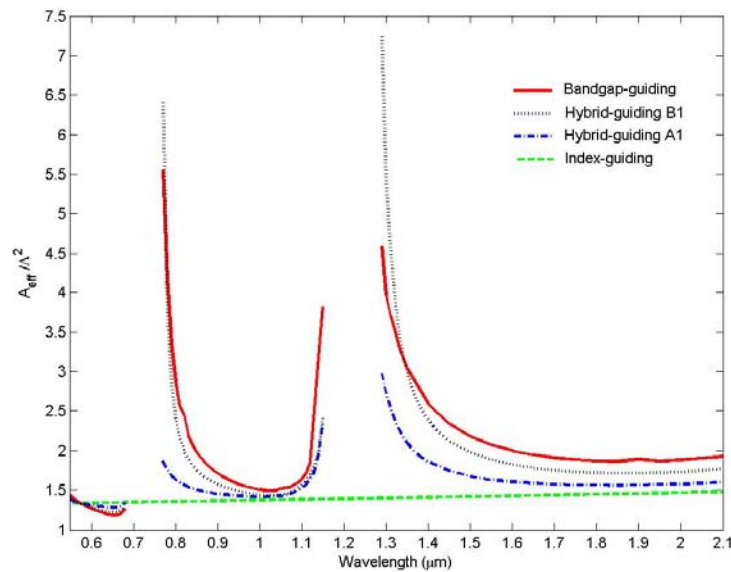


Figure 6.4 Normalized effective mode area of the fundamental mode as a function of wavelength.

For the index-guiding PCF, the effective mode area increases very slowly with an increase in the wavelength. The MFD is  $9.78 \mu\text{m}$  at the wavelength  $0.55 \mu\text{m}$  and increases to  $10.30 \mu\text{m}$  at the wavelength  $2.10 \mu\text{m}$ , as shown in Fig. 5a (1-5) for the wavelength range from  $0.65 \mu\text{m}$  to  $1.55 \mu\text{m}$ . However, for the bandgap PCF, the effective mode area changes dramatically.

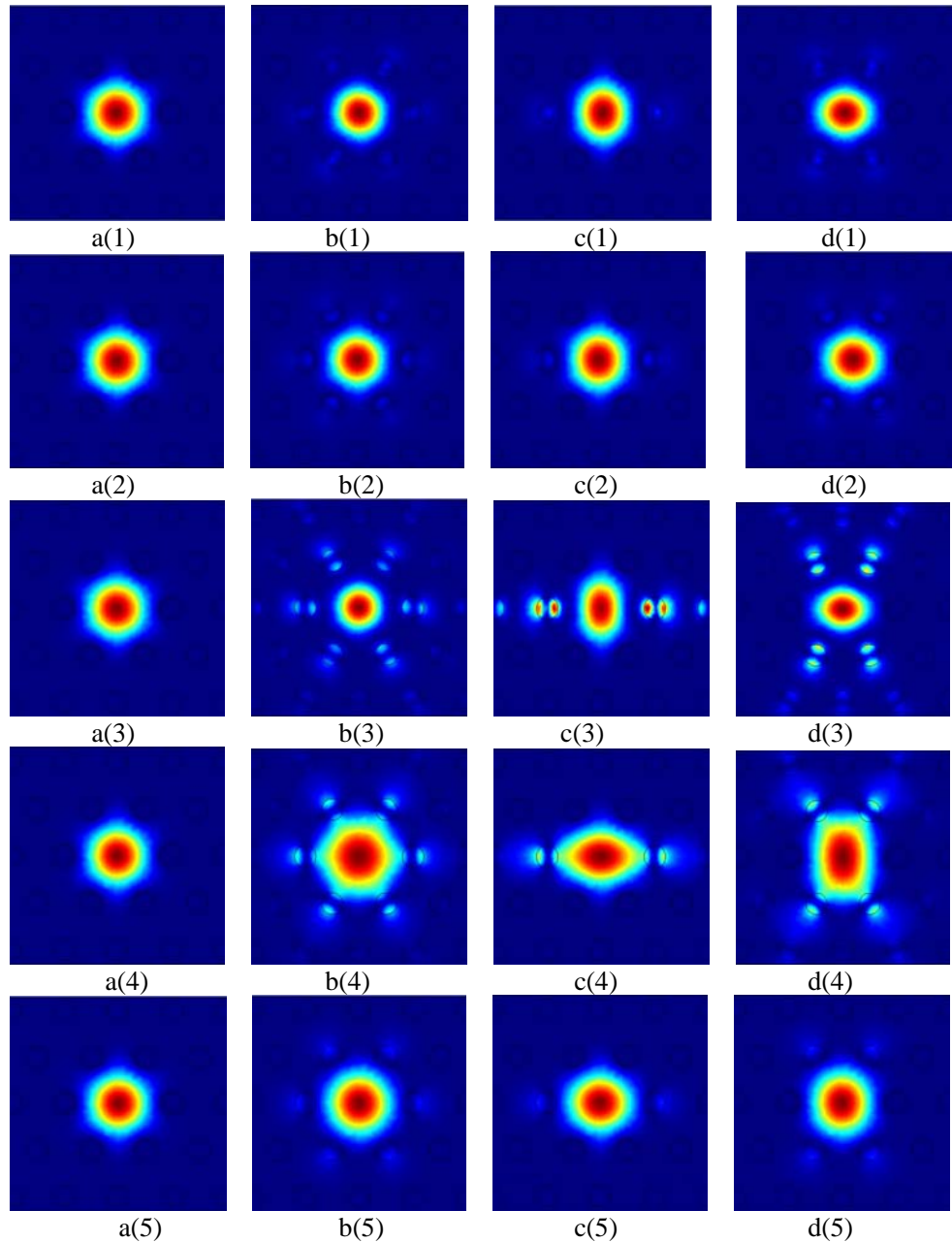


Figure 6.5 Mode intensity distribution of fundamental modes of a (1-5) the index-guiding PCF, b(1-5) the bandgap PCF, c(1-5) the hybrid PCF A1 and d(1-5) the hybrid PCF B1. The wavelength is (1)  $0.65 \mu\text{m}$ , (2)  $1.0 \mu\text{m}$ , (3)  $1.15 \mu\text{m}$ , (4)  $1.30 \mu\text{m}$  and (5)  $1.55 \mu\text{m}$ .

When the wavelengths of the light are close to the middle of the bandgap, the guided modes are well confined in the core, as shown in Fig. 6.5b(1, 2, 5). At the wavelength  $0.65\ \mu\text{m}$  in the third bandgap (Fig. 6.5b(1)), the fundamental mode is well confined in the core, the MFD is  $9.21\ \mu\text{m}$  which is smaller than the MFD of the index-guiding PCF ( $9.81\ \mu\text{m}$ ); at the wavelength  $1.0\ \mu\text{m}$  in the second bandgap (Fig. 6.5b(2)), the MFD is  $10.39\ \mu\text{m}$ , which is slightly larger than the MFD of index-guiding PCF ( $9.92\ \mu\text{m}$ ); at the wavelength  $1.55\ \mu\text{m}$  in the first bandgap (Fig. 6.5b(5)), the MFD is  $12.18\ \mu\text{m}$ , which is significantly larger than the MFD of index-guiding PCF ( $10.10\ \mu\text{m}$ ). When the wavelengths of the light are close to the edges of the bandgap, the effective mode area enlarges rapidly, as shown in Fig. 6.5b (3, 4). This is because of the resonance of the mode in the high-index rod with the core mode [16], which causes the mode to expand and thus increasing the leakage loss.

For the hybrid PCF A1 and B1, the effective mode area is between the effective mode areas of the index-guiding PCF and bandgap PCF when the operation wavelengths are within the middle part of the bandgaps, as shown in Fig. 6.4. The effective mode area curve of hybrid PCF A1 is closer to that of index-guiding PCF and the effective mode area curve of hybrid PCF B1 is closer to that of the bandgap PCF. When the operation wavelengths are close to the middle of the bandgaps, the fundamental modes can be well-confined, as shown in Fig. 6.5c (1, 2, 5) and Fig. 6.5d (1, 2, 5). For example, at the wavelength  $0.65\ \mu\text{m}$ , the normalized mode areas of hybrid PCF A1 and B1 are 1.28 and 1.22 respectively, which is between that of the index-guiding PCF (1.34) and bandgap PCF (1.19). At the wavelength  $1.55\ \mu\text{m}$ , the normalized mode areas of the hybrid PCF A1 and B1 are 1.63 and 1.88 respectively, which is between that of the index-guiding PCF (1.42) and the

bandgap PCF (2.07). When the operation wavelengths are close to the bandgap edges, the effective mode areas of the hybrid PCFs expand quickly, as shown in Fig. 6.5c (3, 4) and Fig. 6.5d (3, 4). The effective mode area of the hybrid PCF B1 is even larger than that of the bandgap PCF at the wavelength of  $1.30\ \mu\text{m}$ , which corresponds to a larger confinement loss than that of the bandgap PCF.

### 6.2.2.3 Confinement loss

Figure 6.6 shows the confinement losses of different PCFs. We can find that the confinement loss of the hybrid PCF A1 and B1 are almost between the loss of the index-guiding PCF and the bandgap PCF except at the bandgap edges. The confinement loss of the index-guiding PCF is very low, it increases from  $1.15 \times 10^{-12}$  dB/m at the wavelength of  $0.55\ \mu\text{m}$  to  $9.54 \times 10^{-10}$  dB/m at the wavelength of  $2.1\ \mu\text{m}$ .

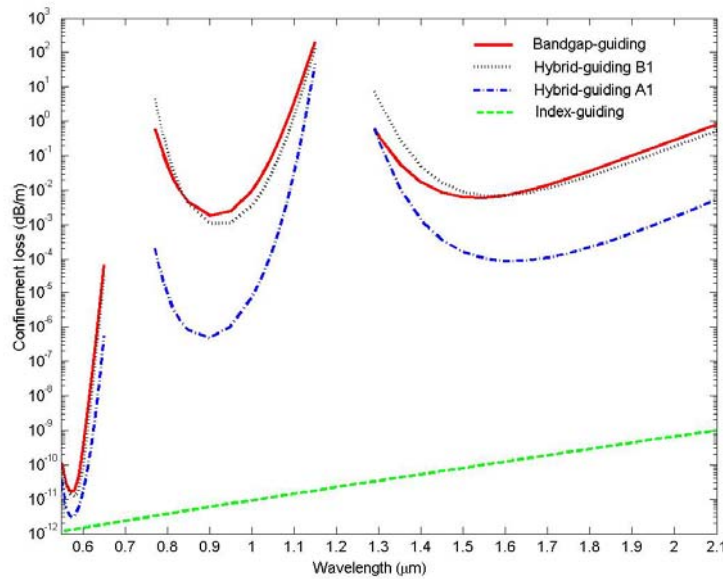


Figure 6.6 Confinement loss of the fundamental mode for different fibers as a function of wavelength.

For the bandgap PCF, the confinement loss is significantly different for all three bandgaps. The confinement loss in the third bandgap is much smaller than the loss in the first and second bandgap. For example, the confinement loss at  $0.58\ \mu\text{m}$  is

$1.75 \times 10^{-11}$  dB/m, however, the confinement losses at 0.9  $\mu\text{m}$  and 1.55  $\mu\text{m}$  are respectively  $1.81 \times 10^{-3}$  dB/m and  $6.01 \times 10^{-3}$  dB/m. For the hybrid PCF A1, the confinement loss is significantly small because the hybrid fiber structure of A1 is much closer to that of the index-guiding PCF. For example, the confinement loss at 0.9  $\mu\text{m}$  and 1.55  $\mu\text{m}$  can be improved to  $4.85 \times 10^{-7}$  dB/m and  $1.01 \times 10^{-4}$  dB/m respectively. The improvement of the confinement loss is attributed to the index-guiding part of the hybrid PCF A1 whose confinement loss is much lower than the bandgap-guiding. It should be noted that it is not for all the cases. For example, when the relative hole size of the index-guiding is significantly small, such as  $d/\Lambda=0.05$ , thus the confinement loss of the index-guiding PCF is larger than the confinement loss of the bandgap PCF, the corresponding hybrid PCF will have lower confinement loss than the index-guiding PCF. So the confinement of the hybrid PCF generally is between the confinement losses of the corresponding index-guiding PCF and bandgap PCF for the operation wavelengths within the middle part of the bandgaps. For the hybrid PCF B1, the confinement loss at the short wavelength edge of the bandgap is larger than the bandgap PCF, it may be explained by bandgap theory. The hybrid-PCF B1 confines light by bandgap effects in the whole cross-section except x direction, the effective index curve is lower than that of bandgap PCF near the short wavelength bandgap edge as shown in Fig. 6.3, which makes the effective index curve closer to the bandgap edge compared with that of the bandgap PCF or even outside the bandgap, thus causing larger confinement loss.

#### **6.2.2.4 Group velocity dispersion**

The GVD property of a fiber similar to hybrid PCF A1 has been demonstrated in Ref. [4]. Here we compare the GVD properties of four different PCFs in the first

bandgap, as shown in Fig. 6.7.

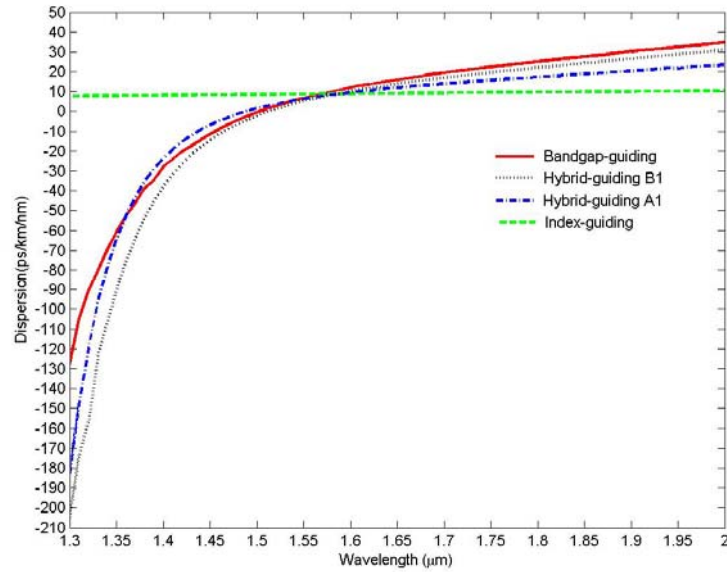


Figure 6.7 GVD of the fundamental mode as a function of the wavelength in the first bandgap

The GVD curve shape of hybrid PCF A1 and B1 is as similar as that of the bandgap PCF. This is due to the similar effective index properties of the hybrid PCFs and the bandgap PCF caused by the bandgap effect, as shown in Fig. 6.3. We can find from Fig. 6.7 that GVD curves of hybrid PCFs, especially hybrid PCF A1, are a little bit flattened compared with the bandgap PCF at the center part of the bandgap. However, the GVD curve of the hybrid PCFs becomes more normal when the operation wavelength is near the bandgap edge. Thus the novel dispersion property of hybrid PCFs can provide new mechanism to design the PCF with modified zero-dispersion wavelength.

### 6.2.2.5 Birefringence

Because the guiding mechanisms of the hybrid PCF A1 and B1 are different in two orthogonal directions, large birefringence for the hybrid PCF is expected. We calculate the birefringence in the first bandgap, the same property is expected for

other bandgaps. To achieve accurate results, we divided one quarter of the fiber cross section into 65280 elements in full-vector FEM. For the index-guiding PCF and the bandgap PCF, the effective index difference of x-polarized and y-polarized fundamental modes which should be degenerate is of the order of  $10^{-7} \sim 10^{-8}$  which is caused by the precision of calculation and could be reduced further by increasing the number of divided elements [9]. Under the same condition, the birefringence of the hybrid PCF A1 and B1 is of the order of  $10^{-5}$  as shown in Fig. 6.8. The birefringence increases with the increase of wavelength, and increases at the short wavelength edge of the bandgap. Thus hybrid PCF has potential to be a high birefringence fiber. For example, when the refractive index and hole diameter of the high-index rod of the hybrid PCF A1 change to 1.65 and  $6 \mu\text{m}$  respectively, the birefringence of the PCF can be high to  $1.04 \times 10^{-3}$  at the wavelength of  $1.55 \mu\text{m}$ .

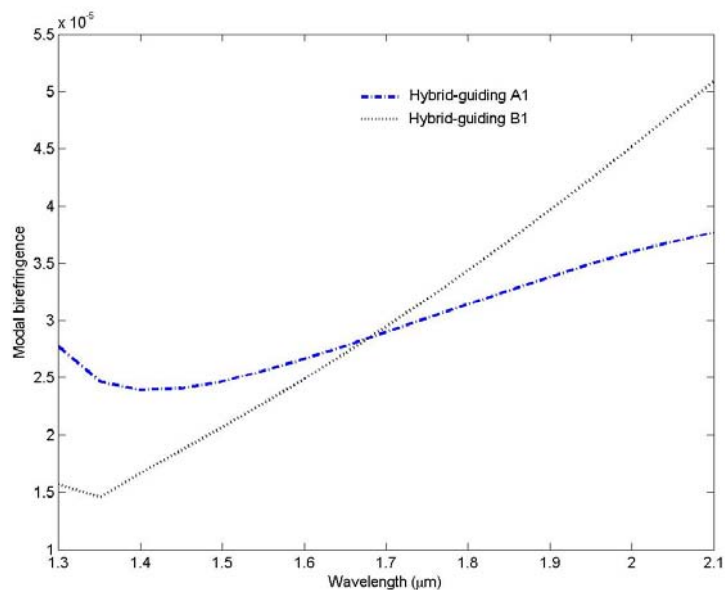


Figure 6.8 Birefringence of the fundamental mode as a function of the wavelength in the first bandgap.

### 6.3 Method of fabrication: micro-hole collapse effect

In Chapter 3, we investigated the micro-hole collapse of different kinds of PCFs and

observed that PCF PM-1550-01 can keep two big holes partially open and all small holes close when applying suitable arc discharge at the end part of the PM-1550-01, as shown in Fig. 6.9.

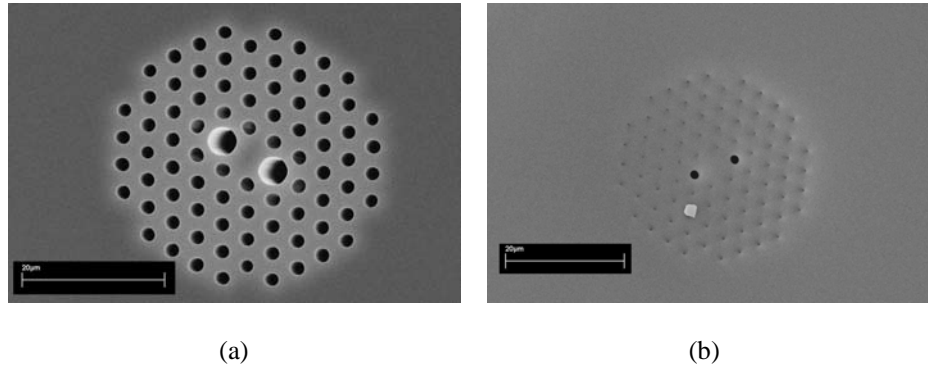


Figure 6.9 (a) SEM photographs of the cross section of the PCF PM-1550-01 without arc discharges. (b) End views of the PM-1550-01 with an arc discharge when fusion current, fusion time, and the offset are 13 mA, 0.3 s, and 50  $\mu\text{m}$  respectively.

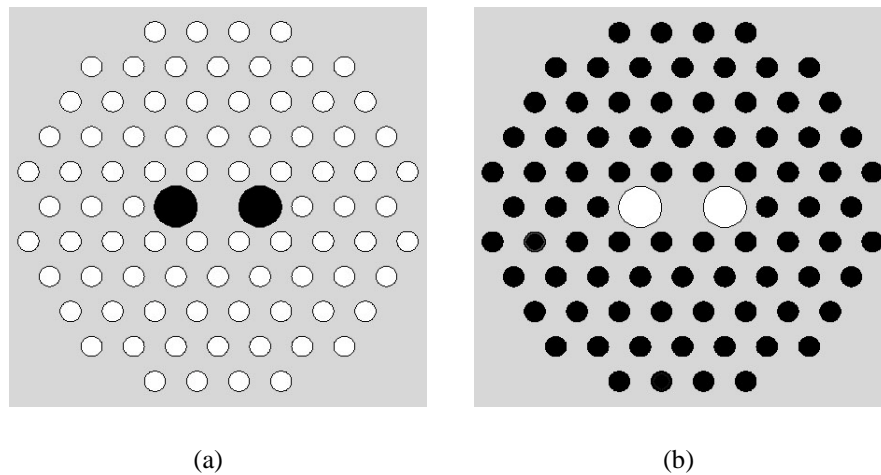


Figure 6.10 Schematics of cross-section of PM-1550-01 with selective filling. (a) Two big holes are filled with UV curable polymer; (b) Small holes are filled with high index liquid, whereas black holes are high-index liquids, empty holes are air holes.

We can fill UV curable polymer into the two big holes of PM-1550-01, as shown in Fig. 6.9(b), by capillary effect; then we cure the UV polymer and cut a short section at the end part of the PCF, thus we can get the PCF with two big holes sealed by cured polymer at the end part, as shown in Fig. 6.10(a). The end of the PCF is then immersed into the high-index liquid for a rather long time, and all smaller holes are

filled with high-index liquid for the whole length except two sealed holes. After cutting the end part of the PCF with cured polymer inclusion, the hybrid PCF can be formed, as shown in Fig. 6.10(b). The side view of selective filling of the PCF can be seen from Fig. 5.1(a). In the x direction, the mode can be confined by index-guiding because of two big air holes; in the y direction, the mode can be confined by bandgap-guiding because of periodic high-index liquid inclusions. As an example, mode intensity distribution of this hybrid PCF at the wavelength of 1550 nm is calculated when the small holes are filled with liquid with refractive index of 1.492. We can find that the hybrid mode can be well confined in the core.

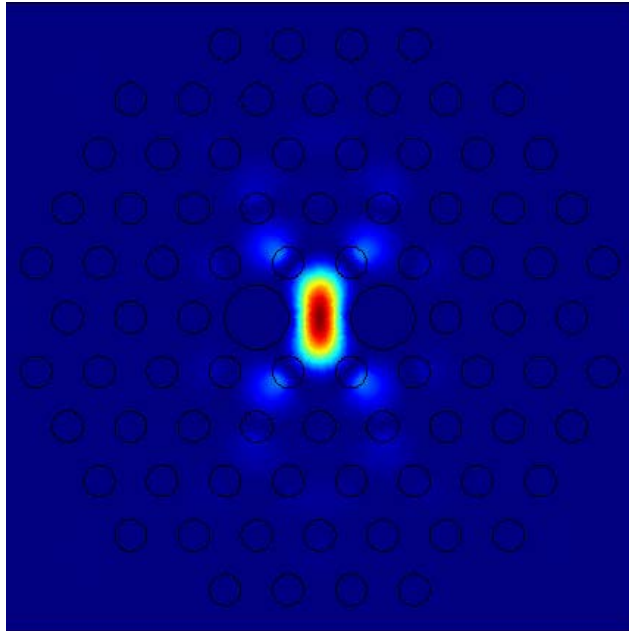


Figure 6.11 Mode intensity distribution of fundamental mode of the hybrid PCF at the wavelength of 1550 nm.

## 6.4 Potential Applications

Because hybrid PCFs have novel guiding mechanism which has the advantages of both index-guiding and bandgap guiding, they have many potential applications. The bending loss of the hybrid PCF A1 and B1 in two orthogonal directions are expected to be very different, which may find application as a directional bending

sensor. The hybrid PCF can be designed as an ultra-low loss filter or switch compared to bandgap PCFs. Hybrid PCFs provide a new mechanism to design high birefringence PCF and to engineer the dispersion. It can also make novel tunable devices when the high-index rod is replaced by high-index liquid, polymer or liquid crystal by using the selective filling technology introduced in Chapter 5. The hybrid PCFs possess a new guiding mechanism which lead us to predict more than three different materials rods can be composed in the fiber and the light can still be well confined in the core, thus providing new ways to design functional fibers such as the fiber composed of semiconductor rods [14, 15], silica and air holes, in which electrons can propagate in the semiconductor rods and photons propagate in the silica core. The combination of hybrid PCF with Bragg gratings and long period gratings may produce grating with new properties, considering that hybrid PCFs may be easier to write gratings using UV light compared with index-guiding PCFs because the index contrast of high-index rod and background silica can be fabricated as low as one percent [16].

## **6.5 Summary**

In conclusion, we have systematically investigated the properties of two kinds of hybrid PCFs. The wavelength dependence of the modal effective index, effective mode area, confinement loss, group velocity dispersion and birefringence has been derived by using a simulation model. The properties and advantages of hybrid PCFs are demonstrated by comparing them with those of the corresponding index-guiding PCF and bandgap-guiding PCF. The method of fabricating hybrid PCFs by micro-hole collapse effect is proposed. Finally, the potential applications of these hybrid PCFs are discussed.

## References for Chapter 6

1. J. C. Knight, T. A. Birks, P. J. Russell, and D. M. Atkin, "All-silica single-mode optical fiber with photonic crystal cladding," *Opt. Lett.*, vol. 21, pp. 1547-1549, (1996).
2. J. C. Knight, J. Broeng, T. A. Birks, and P. J. Russell, "Photonic band gap guidance in optical fibers," *Science*, vol. 282, pp. 1476-1478, (1998).
3. S.G. Johnson, S. Fan, P.R. Villeneuve, J. D. Joannopoulos, and L.A. Kolodziejski, "Guided modes in photonic-crystal slabs," *Phys. Rev. B*, vol. 60, pp. 5751-5780, (1999).
4. A. Cerqueira, F. Luan, C. M. B. Cordeiro, A. K. George, and J. C. Knight, "Hybrid photonic crystal fiber," *Opt. Express*, vol. 14, pp. 926-931, (2006).
5. T. A. Birks, J. C. Knight, and P. J. Russell, "Endlessly single-mode photonic crystal fiber," *Opt. Lett.*, vol. 22, pp. 961-963, (1997).
6. T. A. Birks, P. J. Roberts, P. J. Russell, D. M. Atkin, and T. J. Shepherd, "Full 2-D photonic bandgaps in silica/air structures," *Electron. Lett.*, vol. 31, pp. 1941-1942, (1995).
7. N. Litchinitser, S. Dunn, B. Usner, B. Eggleton, T. White, R. McPhedran, and C. de Sterke, "Resonances in microstructured optical waveguides," *Opt. Express*, vol. 11, pp. 1243-1251, (2003).
8. S. Guo and S. Albin, "Simple plane wave implementation for photonic crystal calculations," *Opt. Express*, vol. 11, pp. 167-175, (2003).
9. M. Koshiba, "Full vector analysis of photonic crystal fibers using the finite element method," *IEICE Electron*, E85-C4, pp. 881-888, (2002).
10. K. Saitoh and M. Koshiba, "Numerical modeling of photonic crystal fibers," *J. Lightwave Technol.*, vol. 23, pp. 3580-3580, (2005).

11. K. Saitoh and M. Koshiba, "Leakage loss and group velocity dispersion in air-core photonic bandgap fibers," *Opt. Express*, vol. 11, pp. 3100-3109, (2003).
12. K. Saitoh and M. Koshiba, "Full-vectorial imaginary-distance beam propagation method based on finite element scheme: Application to photonic crystal fibers," *J. Quantum Electron.*, vol. 38, pp. 927-933, (2002).
13. N. A. Mortensen, "Effective area of photonic crystal fibers," *Opt. Express*, vol. 10, pp. 341-348, (2002).
14. S. D. Hart, G. R. Maskaly, B. Temelkuran, P. H. Pridaux, J. D. Joannopoulos, and Y. Fink, "External reflection from omnidirectional dielectric mirror fibers," *Science*, vol. 296, pp. 510-513, (2002).
15. P. J. A. Sazio, A. A. Correa, C. E. Finlayson, J. R. Hayes, T. J. Scheidemantel, N. F. Baril, B. R. Jackson, D. J. Won, F. Zhang, E. R. Margine, V. Gopalan, V. H. Crespi, and J. V. Badding, "Microstructured Optical Fibers as High-Pressure Microfluidic Reactors," *Science*, vol. 311, pp. 1583-1586, (2006).
16. A. Argyros, T. Birks, S. L. Saval, C. M. Cordeiro, F. Luan, and P. J. Russell, "Photonic bandgap with an index step of one percent," *Opt. Express*, vol. 13, pp. 309-314, (2005).

## Chapter 7

### Conclusion and future work

#### 7.1 Conclusion

In this thesis, we have investigated different splice techniques between PCFs and SMFs, the microhole collapse property and its applications. Four important issues have been addressed: (1) low-loss fusion splicing different kinds of PCFs to SMFs using a conventional fusion splicer; (2) low-loss splicing PCFs to SMFs using photopolymer microtips; (3) fabrication of selective injection PCFs by microhole collapse effect; (4) the properties of hybrid PCFs.

We provided the guidelines for fusion splicing different kinds of PCFs to SMFs, and investigated the micro-hole collapse property of five different kinds of PCFs. The physical mechanism of the splice loss was studied in detail and then different methods were proposed according to the different structure of PCFs to achieve low-loss splicing. For the splicing between PCFs, and between the PCF and the SMF having similar MFDs, low-loss splicing can be achieved by minimizing the collapse of air holes of the PCF. For the small-core PCF with low air-filling fraction, including the PM-PCF, low-loss splicing can be achieved by applying repeated arc discharges over the splicing joint to gradually collapse the air holes of the

small-core PCF. For the small-core PCF with high air-filling fraction, an intermediate fiber should be used to decrease the splice loss. We have demonstrated the low-loss splice of these different PCFs with conventional SMFs. The experimental results prove that fusion splicing is a simple and practical solution to solve the coupling problem between PCFs and SMFs, which will benefit the development of different PCF devices and sensors for practical application.

We demonstrated the use of photopolymer micro-tip to improve the light coupling efficiency from SMFs to small-core PCFs. The method is based on growing photopolymer micro-tips directly on the end face of SMFs. The advantages of this micro-tip fabrication method are its simplicity, controllability, reproducibility and being inexpensive. The shape and the size of the tips can be controlled, by adjusting the laser power, the exposure time and the oxygen diffusion concentration for polymerization, to match its mode field to the small-core PCFs. A photopolymer micro-tip integrated on the end face of a SMF is used to reduce the mode field diameter and increase the numerical aperture of the light beam coming out from the SMF, so that there is a better match to the small mode field diameter and the large numerical aperture of small-core PCFs. A 5 dB improvement in coupling efficiency between a SMF and a commercial small-core, highly nonlinear PCF is demonstrated. This compact and efficient butt-coupling method is particularly suitable for PCF gas sensor applications where holes in the PCF need to be kept open at the joint for easier access to the evanescent field.

We developed a simple method for selective filling the central hole of PCFs. The method is based on a conventional fusion splicer which causes the cladding holes to collapse while leaving the central hollow core to remain open. Theoretical and experimental investigations show that the hole-collapse property of a PCF depends

on fusion current, fusion duration and fusion offset position. The opening and closing of the central hole and the holes in the cladding may be controlled to a certain degree by controlling the fusion current, the fusion duration and the fusion offset position. Experiments show that this method can be used to make hybrid polymer/silica PCFs having the central hole filled by a polymer. This novel structure not only introduces an effective way for micro-fluidic sensing applications, but also opens new perspectives for nonlinear applications by filling various functional materials into the central hole of a hollow-core PCF.

We also investigated the properties of two kinds of hybrid PCFs. The wavelength dependence of the modal effective index, effective mode area, confinement loss, group velocity dispersion and birefringence has been derived by using a simulation model. The properties and advantages of hybrid PCFs are demonstrated by comparing them with those of the corresponding index-guiding PCF and bandgap-guiding PCF. The method of fabricating hybrid PCFs by micro-hole collapse effect was demonstrated and the potential applications of these hybrid PCFs were also discussed.

## **7.2 Future work**

Our splicing techniques for PCFs will give a significant impetus for integrating PCFs into existing fiber optic systems. The micro-hole collapse effect and the incorporation of new materials will provide a new platform for ultra-compact photonic devices. In particular, we have the following suggestions for future study.

To further decrease the coupling loss between small-core PCFs and conventional SMFs, a theoretical investigation of the optimized collapse length of the PCFs using beam propagation method would be useful. The experimental results may be further improved by choosing a wider electrode gap for the fusion splicer to increase the

length of the adiabatic air hole collapse. For direct splicing among different types of PCFs, the two major challenges of microhole collapse and mode mismatch should be considered. The parameters of the fusion splicer such as fusion time, fusion current, offset and overlap should be further investigated to optimize the hole collapse and to increase the mechanical strength of the joint.

Since hollow-core PCFs are mainly produced for photonic bandgap guiding, the air-filling fraction of this kind of hollow-core PCFs are over 90%, thus causing the cladding index to be rather low. For liquid-core based PCF applications, when the central core of the PCF is filled with liquid, the high index contrast will lead to multimode operation, which is not desirable for sensor applications or fabrication of functional fiber devices. In future work, the design of a hollow-core PCF with suitable relative hole size should be attempted to achieve single-mode operation for liquid-core PCF applications. The thickness of the silica interface surrounding the air core will be specially designed to eliminate surface modes.

The bending properties of index-guiding PCF and bandgap PCF are quite different. The macro-bending loss of bandgap PCFs can exist both inside and outside of the bend at the long wavelength edge and the short wavelength edge respectively. For the hybrid PCF A4 in Chapter 6, when the PCF is bent upward, the induced loss mainly occurs at the short-wavelength edge of the transmission band; when the PCF is bent downward, bend-loss will occur at the long-wavelength edge. Thus it can be designed to serve as a directional bend sensor.

# Appendix

## Publications

### Journal articles

1. **Limin Xiao**, Wei Jin, M. S. Demokan, “Photonic crystal fibers confining light by both index-guiding and bandgap-guiding: hybrid PCFs,” *Optics Express*, vol.15, pp. 15637-15647, November 2007.
2. **Limin Xiao**, M. S. Demokan, Wei Jin, Yiping Wang, Chunliu Zhao, “Fusion splicing photonic crystal fibers and conventional single mode fibers: micro-hole collapse effect,” *Journal of Lightwave Technology*, vol. 25, pp. 3563-3574, November 2007.
3. **Limin Xiao**, Wei Jin, M. S. Demokan, “Fusion splicing small-core photonic crystal fibers and single mode fibers by repeated arc discharges,” *Optics Letters*, Vol. 32, pp. 115-117, January 2007. (Reported in the news of Technology World section of Photonics Spectra Magazine Feb2007)
4. **Limin Xiao**, Wei Jin, M. S. Demokan, Hoi L. Ho, Hwa-yaw Tam, Jian Ju, Jianming Yu, “Photopolymer microtips for efficient light coupling between single-mode fibers and photonic crystal fibers,” *Optics Letters*, Vol. 31, pp. 1791-1793, June 2006. (Selected by Virtual Journal of Nanoscale Science & Technology, June 19, 2006)
5. **Limin Xiao**, Wei Jin, M. S. Demokan, Hoi L. Ho, Yeuk L. Hoo, Chunliu Zhao,

- “Fabrication of selective injection microstructured optical fibers with a conventional fusion splicer,” *Optics Express*, Vol. 13, pp. 9014-9022, October 2005.
6. Yun Han, Maung Kyaw Khaing Oo, Yinian Zhu, Henry Du, Svetlana Sukhishvili, **Limin Xiao**, M. S. Demokan, and Wei Jin, “Index-guiding liquid-core photonic crystal fiber for solution measurement using normal and surface-enhanced Raman Scattering,” submitted to *Applied Physics Letters*.
  7. Chunliu Zhao, **Limin Xiao**, Jian Ju, M. S. Demokan, Wei Jin, “strain and temperature characteristics of a long period grating written in a photonic crystal fiber and its application as a temperature-insensitive strain sensor,” (in press) *Journal of Lightwave Technology*.
  8. Chunliu Zhao, M. S. Demokan, Wei Jin, **Limin Xiao**, “A cheap and practical FBG temperature sensor utilizing a long-period grating in a photonic crystal fiber,” *Optics Communications*, Vol. 276, pp. 242-245, August 2007.
  9. Yiping Wang, **Limin Xiao**, D. N. Wang, and Wei Jin, “In-fiber polarizer based on long period fiber grating written on photonic crystal fiber,” *Optics Letters*, Vol. 32 , pp. 1035-1037, May 2007 (Reported in the news of Photonics Research section of Photonics Spectra Magazine Jun 2007)
  10. Yiping Wang, **Limin Xiao**, D. N. Wang, Wei Jin, “Highly sensitive long-period fiber-grating strain sensor with low temperature sensitivity,” *Optics Letters*, Vol. 31, pp. 3414-3416, December 2006. (Reported in the news of Technology World section of Photonics Spectra Magazine Jan 2007)
  11. Yiping Wang, Wei Jin, Jian Ju, Haifeng Xuan, Hoi Lut Ho, **Limin Xiao** and Dongning Wang, “Long period gratings in air-core photonic bandgap fibers,” (accepted with revisions) *Optics Express*.

## Conference proceedings

1. **Limin Xiao**, Wei Jin, and M. S. Demokan, “Photopolymer microtips for efficient light coupling between single-mode fibers and small-core photonic crystal fibers,” *Optics East*, 6379A-02, October 2006.
2. **Limin Xiao**, Wei Jin, and M. S. Demokan, “Low-Loss Splicing Small-Core Photonic Crystal Fibers and Single-Mode Fibers by Repeated Arc Discharges,” *CLEO/QELS*, JTuA89, May 2007.
3. Yun Han, Maung Khaing Oo, Yinian Zhu, Svetlana A. Sukhishvili, **Limin Xiao**, M. S. Demokan, Wei Jin, Henry H. Du, “Index-guiding liquid-core photonic crystal fiber for sensing of solutions using normal and surface-enhanced Raman scattering,” *Optics East*, 6767-17, September 2007.

## Patent

**Limin Xiao**, M. S. Demokan and Wei Jin, “Low loss splicing a small-core photonic crystal fiber and a single mode fiber by repeated arc discharges,” U.S. Patent Application No. 60/834175, filed on July 31, 2006.

## Award

**2006 Chung Hwa Travel Service Scholarship**, The Hong Kong Polytechnic University (Only 4 scholarships are awarded yearly to postgraduate research students in PolyU for academic excellence)